Alma Mater Studiorum · University of Bologna

School of Science
Department of Physics and Astronomy
MASTER DEGREE IN PHYSICS

Fostering Confidence: Evaluating Inter-Site Reproducibility of Bingham-NODDI Model Measures using Phantoms and In-Vivo Acquisitions

Supervisor:
Prof. CLAUDIA TESTA

Co-supervisor:
Dr. JAMES GRIST

Submitted by:
NOEMI SGAMBELLURI

Academic Year 2022/2023

For those who have gathered me when I needed gathering
and given me a launchpad when I needed to dream.

ABSTRACT

Recently, a diffusion model has been introduced to estimate Neurite Orientation Dispersion and Density Imaging (NODDI), a pivotal tool in neuroscience, offering insights into the intricated microstructure of the brain, and in particular, a detailed view of the spatial organization of microscopic neural components known as neurites. The NODDI model reveals the directional alignment of neurites, the degree of their dispersion or organization, and the density of their distribution across distinct brain regions. The Bingham-NODDI model extends the Watson-NODDI formalism to address its limitations in capturing complex neurite structures such as the way they spread or bend, providing more advanced and biologically relevant insights into neurological conditions such as Alzheimer's disease and Multiple Sclerosis. While the model demonstrates significant capabilities, it still is undergoing testing across different MRI scanner systems to ascertain its robustness.

This study aims to evaluate the reliability and consistency of the model by validating it using an MRI test object and *in-vivo* acquisitions, ensuring intra-site stability on each scanner employing coefficient of variation analysis and inter-site comparability of the generated data. Phantom and *in-vivo* acquisitions were performed on 3T high-field scanner systems (GE Signa Premier and Siemens MAGNETOM Prisma) and a 1.5T GE Artist. The inter-site phantom study results show consistency across scanners for the tensor model. Investigations into Mean Diffusivity values highlight a decrease with increasing echo times, requiring future further investigation. Complementing the phantom study, scans of healthy volunteers on GE Premier and Siemens Prisma affirm the Bingham-NODDI model's stability, with slight variations falling within acceptable margins of error for key metrics. In-depth analyses of the Orientation Dispersion Index, Tissue Volume Fraction, and Intra-neurite Volume Fraction underscore the model's reliability.

The Bingham-NODDI model's demonstrated reliability serves as a solid foundation for detecting minor changes in brain microstructure over time, presenting a valuable tool for clinicians in both neuroscience and clinical fields. This study contributes to advancing multi-center studies by transcending individual equipment boundaries, paving the way for collaborative research and clinical applications.

Contents

List of Figures

List of Tables

Introduction

Magnetic Resonance Imaging (MRI) stands as a pivotal technology in the realm of medical diagnostics, offering a non-invasive and highly detailed insight into the internal structures of the human body. This technique exploits the principles of nuclear magnetic resonance (NMR), harnessing the magnetic properties of certain atomic nuclei, notably hydrogen protons, which abound in the human body due to the high water content of tissues [1, 2]. MRI is exceptionally versatile as it is able to produce detailed cross-sectional images of soft tissues, organs, and musculoskeletal structures, rendering it a cornerstone in diagnosis and research. Unlike computed radiography (CT) scans, MRI does employ ionizing radiation, making it a safer option for repeated imaging studies. This technique is also able to provide rich contrast resolution, allowing to distinguish various tissue types based on their distinct water content and molecular environment making it an invaluable tool for elucidating abnormalities in the brain. Diffusion Weighted Imaging (DWI) is an MRI technique that offers unique insights into the microstructural characteristics of tissues. DWI capitalizes on the inherent mobility of water molecules in biological tissues, providing a sensitive means to probe the diffusion of water at the microscopic level. This imaging technique has found widespread applications in both clinical and research settings due to its ability to unveil subtle alterations in the tissue microstructure, being extremely useful to depict diffusion properties of the water molecules in the brain.
The fundamental principle underlying DWI involves the application of strong magnetic gradients during imaging, sensitizing the MRI signal to the random thermal motion of water molecules causing a reduction of the total signal [3]. DWI is used to visualize and analyze white matter tracts as water molecules tend to diffuse along axons in a preferential way hence representing a way of estimating the properties of white matter in the brain.

Currently, the most used diffusion metrics used in DWI analysis are fractional anisotropy (FA) and mean diffusivity (MD), also known as apparent diffusion coefficient (ADC). These metrics offer quantitative information that reflects the degree of diffusion anisotropy in the brain and the average magnitude of diffusion and are obtained from the diffusion tensor model introduced by Basser et al. [4]. Given the restricted movement of water molecules along the axonal fibers that constitute white matter, high FA values suggest a more organized and coherent arrangement of neurites, providing information about the structural integrity and orientation of white matter tracts. Changes in FA can be associated with alterations in tissue microstructure, such as demyelination, axonal damage, or changes in fiber density. Clinically, reduced FA is often observed in conditions like neurodegenerative diseases, traumatic brain injury, or white matter disorders [3, 5, 6]. However, these markers are inherently non-specific. Notably, FA is also a relative measure, presenting in some cases potential pitfalls [7].

Zhang et al. [8] proposed a new model to address the limitations of the tensor model and developed a clinically feasible technique for *in vivo* neurite orientation dispersion and density imaging (NODDI). This technique combines a three-compartment tissue model with a two-shell high-angular-resolution diffusion imaging (HARDI) protocol, which is optimized for clinical feasibility, to map neurite orientation dispersion and density *in vivo* [8]. NODDI divides the signal into three compartments: fast isotropic diffusion (e.g., cerebrospinal fluid (CSF)), anisotropic hindered diffusion (e.g., extracellular water), and highly restricted anisotropic diffusion (e.g., intra-axonal compartments) [8]. From these compartments, parameters such as the neurite density index (NDI) and the orientation dispersion index (ODI) can be calculated. Regions with high ODI values are thought to reflect highly dispersed neurites (a term referring to both dendrites and axons) and com-

plex cytoarchitecture, for example in the gray matter, while lower ODI values are more likely to correspond to more tightly organized structures, such as white matter tracts [8, 9]. Studies have shown complementary results regarding MD and NDI being impacted by age-related differences in a healthy population at risk for Alzheimer's disease, with MD having a stronger association with age, while NDI being more predictive of Executive Function [10]. Therefore, DTI and NODDI metrics may provide complementary and clinically relevant insight into white matter abnormalities hence demonstrating that there is an added clinical value to further investigate the accuracy of the NODDI technique.
Notably, the NODDI model uses the Watson distribution as the orientation distribution function of neurites, only allowing the dispersion around the dominant neurite orientation to be isotropic. This mathematical form is limited as it cannot accurately model complex neurite configurations such as the bending and fanning of axons. In these fibre configurations, the dispersion around the dominant orientation is higher in the plane of fanning and bending, but lower in the plane perpendicular to it, causing anisotropic fibre dispersion that cannot be captured by the Watson distribution.
In this framework, Tariq et al. [11] introduced the Bingham-NODDI model, an extension of the NODDI model that uses the Bingham distribution instead of the Watson distribution. The new model estimated the extent of dispersion about the dominant orientation separately along the primary and secondary dispersion orientations allowing to capture anisotropic dispersion of the neurite configuration.
In summary, the Bingham-NODDI mode offers a more nuanced and detailed characterization of tissue microstructure compared to traditional DTI measures. Its ability to handle complex fiber configurations, provide biologically relevant metrics, and offer increased sensitivity to subtle changes makes it a valuable tool for advancing our understanding of tissue microarchitecture in both research and clinical settings.
However, the Bingham-NODDI model validation is still pending. In this framework, the aim of this study is to evaluate the consistency and stability of the Bingham-NODDI model metrics results across different MRI scanner systems. In particular, metrics of interest are the Orientation Dispersion Index (ODI), the Tissue Volume Fraction, and the Intra-Neurite Volume Fraction. These parameters serve as meaningful indicators of the inherent microstructural characteristics of brain tissue, offering valuable insights into the pathophysiological mechanisms associated with various neurological disorders. To assess the repeatability of results across different MRI scanners, this study uses a DTI test object, also known as 'phantom'.
Phantoms are valuable tools in MRI for several reasons:

- **Standardization**: Phantoms provide a standardized reference that ensures consistent and comparable imaging across different MRI scanners. This is critical for research and clinical applications, as it minimizes variations in image quality and allows for meaningful comparisons.

- **Quality Control**: Phantoms serve as quality control tools, helping assess and maintain the performance of MRI scanners. Regular phantom scans can detect issues, such as signal drift, geometric distortion, or image artifacts, which might affect data quality.

- **Comparative Assessments**: Phantoms provide a basis for comparative assessments of MRI scanners. Researchers can use phantoms to evaluate and rank different scanners based on image quality, resolution, signal-to-noise ratio, and other performance metrics.

- **Cross-Site Studies**: In multicenter studies or studies involving multiple sites, phantoms are invaluable for ensuring data consistency. They help harmonize imaging between sites, making it easier to combine and analyze data from various locations.
- **Calibration**: Phantoms aid in the calibration of MRI scanners to ensure that the measurements are accurate and reliable. This is especially important when performing quantitative analyses or when comparing data across different scanners.
- **Safety Testing**: Phantoms can be used to assess the safety of MRI scanners, particularly concerning issues like radiofrequency (RF) heating. Ensuring the safety of MRI procedures is paramount in clinical practice.

Hence, phantoms are essential in MRI studies and scanner comparisons.
This study employed a DTI basic phantom that mimics restricted anisotropic diffusion in the brain, in particular in white matter.
The phantom is scanned on three different 3T MRI scanners (GE Premier located at the Oxford Centre for Magnetic Resonance - University of Oxford, GE Premier located at the Churchill Hospital - Oxford Hospitals, and the Siemens Prisma with two different acquisitions protocols, i.e. monopolar and bipolar gradient acquisitions) and a 1.5T MRI scanner (GE Artist located at the Churchill Hospital) on multiple days. The phantom data underwent fitting processes using both tensor and NODDI models, accounting for variations in acquisitions across distinct MRI vendors. This involved the adaptation of codes and appropriate correction for distortions in each case. Despite these adjustments, a uniform pipeline of work was maintained to facilitate meaningful comparisons of the results.

After evaluating the repeatability of the fits on the phantom, two healthy volunteers were scanned twice on the GE Premier and Siemens Prisma to verify the consistency of results across different MRI scanners. The volunteers are scanned using the same acquisition protocol as the phantoms. Lastly, a final analysis was conducted on the basic phantom to investigate the correlation between the echo time and the tensor model metrics, focusing on the behavior of the MD values with increasing echo times.

This thesis is structured as follows:

- Chapter 1 provides a detailed overview of diffusion-weighted imaging, including an in-depth explanation of the Diffusion Tensor Model, the DW sequences and the process of acquiring diffusion-weighted images, and the gradient vector orientations algorithm developed by Jones et al. The chapter also covers a detailed description of the calculation of apparent diffusivities and the diffusion tensor model's metrics.
- Chapter 2 offers an in-depth description of the models used for this study hence describing briefly the NODDI model, its linear formulation in the AMICO-NODDI model and the model that needs to be assessed, the Bingham-NODDI model.
- Chapter 3 offers a detailed description of the DTI phantom used in this study and an overview of each scanner's specifications as well as the acquisition parameters used for the phantom and *in-vivo* acquisitions.
- Chapter 4 offers a detailed description of the how the models described in Chapter 2 were implemented in Python and proper adjustements to perform the analysis on each scanner.

- Chapter 5 describes how the acquired data are processed and the metrics of interest are obtained. In particular, the last part of the chapter describes how the ROIs, from which the metrics are extracted, are created.
- Chapter 6 shows phantom results providing a detailed discussion of the outcomes as well as inter-site comparisons.
- Chapter 7 offers an investigation of the link between the echo time and b-values and MD values, showing results and discussion of the outcomes.
- Finally Chapter 8 shows the *in-vivo* results obtained across different MRI scanners, providing the quantitative maps for each model's metric and a detailed discussion of the outcomes as well as inter-site comparisons of the differences.

Chapter 1

Diffusion Weighted Imaging

Diffusion-weighted imaging (DWI) is a powerful magnetic resonance imaging technique that provides valuable insights into the movement of water molecules within tissues. It has become an indispensable tool in medical imaging, particularly in the fields of neurology and oncology. DWI offers a unique perspective on the microstructural characteristics of biological tissues by exploiting the natural diffusion of water molecules. This non-invasive imaging modality is widely used in clinical practice, aiding in the early detection of diseases, guiding treatment decisions, and monitoring treatment responses. Therefore, DWI plays an essential role in healthcare and in research in the field of medical imaging, offering a deeper understanding of tissue microstructure and physiology.
Diffusion is a random transport phenomenon that characterizes the transfer of material (e.g., water molecules) primarily due to random thermal fluctuations. In three dimensions, the Einstein diffusion equation [12]:

$$D = \frac{< \Delta r^2 >}{2n\Delta t} \tag{1.1}$$

states that the diffusion coefficient D (in mm^2/s) is proportional to the mean squares displacement $< \Delta r^2 >$ divided by the number of dimensions n, and the diffusion time, Δt. The diffusion coefficient of pure water at 20°C is roughly $2.0 \times 10^{-3} mm^2/s$ and increases at higher temperatures. In the absence of boundaries, the molecular water displacement is described by a Gaussian probability density:

$$P(\Delta r, \Delta t) = \frac{1}{\sqrt{(2\pi\Delta t)^3}} exp\left(\frac{-\Delta r^2}{4D\Delta t}\right) \tag{1.2}$$

The spread in this distribution increases with the diffusion time, Δt, as illustrated in Figure 1.1: The diffusion of water in biological tissues is strictly related to cellular structures. In addition to being influenced by thermal fluctuations, its behavior is also subject to modulation through interactions with cellular membranes, subcellular components, and organelles. In the case of the brain, the latter is made up of two main tissues: white matter and gray matter. Grey matter is made of neuronal cell bodies, indicating that cell membranes constrain diffusion in this tissue type but remain isotropic. White matter primarily consists of myelinated axons (see Figure 1.2) connecting with neurons in other regions of the brain, leading to a constrained diffusion of water molecules. In particular, water diffusion is relatively unimpeded in the direction parallel to the fibre orientation. Conversely, water diffusion is highly restricted and hindered in directions perpendicular to the fibers. Thus, the diffusion in fibrous tissues is anisotropic [3]. Early diffusion imaging

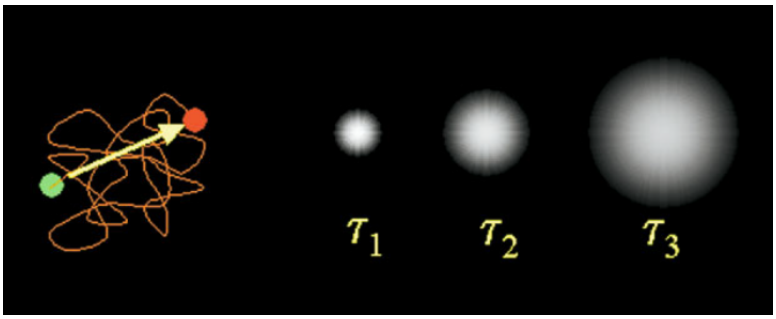

Figure 1.1: Left: Illustration of the diffusion random walk for a single water molecule from the green location to the red location. The displacement is indicated by the yellow arrow. Right: Diffusion describes the probability of displacement with time for a group or ensemble of water molecules. For short diffusion times, the predicted spread is compact but increases with longer diffusion times. Image credit to "Diffusion Tensor Imaging of the Brain" [3]

experiments used measurements of parallel ($D_{\parallel}$) and perpendicular ($D_{\perp}$) diffusion components to characterize the diffusion anisotropy [3]. As a result, white matter displays

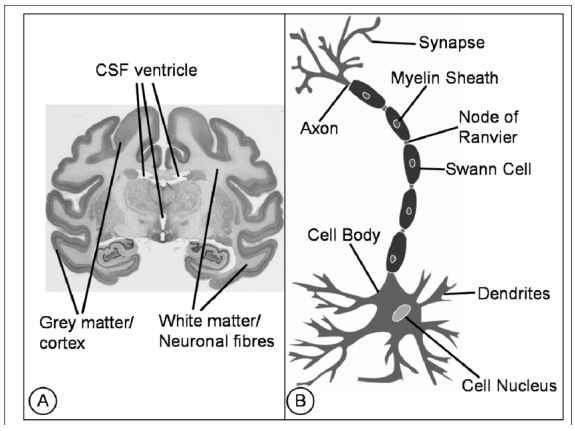

Figure 1.2: A) Coronal cut through the brain showing in dark grey the different cell types and layers of the grey matter and in light grey the white matter, which is composed of neuronal fibre bundles (figure is modified, original figure from: www.brainmaps.org). B) An exemplary neuronal fibre is shown. Image credit to [3]

anisotropy, showing a distinct tendency for diffusion to align with the orientations of fibers, specifically aligning with axons. This feature is extremely valuable to infer structural information about the organization of neural fibers in the brain as well as allowing for the mapping of white matter fiber tracts, assuming that the direction of the fastest diffusion reflects the overall alignment of the fibre tracts [13].

1.1 DTI

Diffusion Tensor Model is an elegant model introduced by Basser et al. [14] according to which diffusion is described by a Multivariate Normal Distribution, as shown in Eq. 1.3:

$$P(\Delta\vec{r}, \Delta t) = \frac{1}{\sqrt{(4\pi\Delta t)^3 \left|\mathbf{D}\right|}} \exp\left(\frac{-\Delta\vec{r}^{\,T}\mathbf{D}^{-1}\Delta\vec{r}}{4\Delta t}\right) \tag{1.3}$$

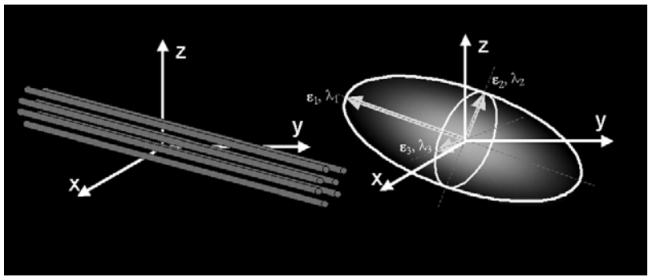

Figure 1.3: Schematic representation of diffusion displacement distributions for the diffusion tensor through ellipsoids. Image credit to [3].

where the diffusion tensor D is a 3×3 covariance matrix defined in Eq. 1.4

$$\mathbf{D} = \begin{pmatrix} D_{xx} & D_{xy} & D_{xz} \\ D_{yx} & D_{yy} & D_{yz} \\ D_{zx} & D_{zy} & D_{zz} \end{pmatrix} \tag{1.4}$$

describing the covariance of diffusion displacement on three dimensions normalized by the diffusion time. The diagonal elements ($D_{ii} > 0$) are the diffusion variances along the axes x, y, and z, while the off-diagonal terms are the covariances and are symmetric about the diagonal ($D_{ij} = D_{ji}$) [15]. Diagonalizing the diffusion tensor matrix produces the eigenvalues $(\lambda_1, \lambda_2, \lambda_3)$ and their corresponding eigenvectors $(\vec{V_1}, \vec{V_2}, \vec{V_3})$ which describe the directions and apparent diffusivities along the axes of principal diffusion.
The diffusion tensor may be visualized as an ellipsoid, with the eigenvectors defining the directions of the principal axes and the ellipsoidal radii defined by the eigenvalues (1.3). Diffusion is considered isotropic when the eigenvalues are nearly equal (e.g. $\lambda_1 \approx \lambda_2 \approx \lambda_3$) whilst it is considered anisotropic when the eigenvalues are significantly different in magnitude (e.g. $\lambda_1 > \lambda_2 > \lambda_3$). The eigenvalue magnitudes are susceptible to changes in local microstructures, hence the diffusion tensor model is a powerful tool for characterizing both normal physiological changes (e.g., aging) and abnormal tissue microstructure (e.g., tissue injury, disease). The diffusion is highly anisotropic on fibrous tissue as white matter while it is isotropic in both gray matter and cerebrospinal fluid (CSF). The greatest diffusion direction ($\vec{V_1}$) is generally assumed to be parallel to the local direction of homogeneous white matter. A diagram displaying the effects of tissue microstructure on diffusion measurements is shown in Figure 1.4. In the case of isotropic diffusion, the

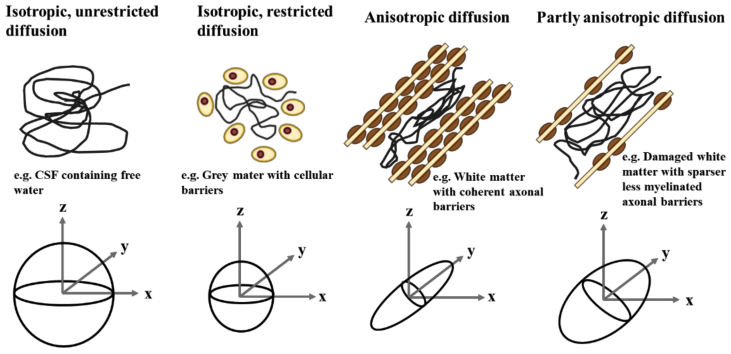

Figure 1.4: Diagram displaying tensors from different microstructure.

diffusion ellipsoid takes the form of a sphere because the Apparent Diffusion Coefficient

is consistent in all directions. This aligns with our expectations for cerebrospinal fluid (CSF), as it primarily consists of approximately 99% water and is predominantly found in the ventricles, allowing molecules to diffuse freely. Larger sphere dimensions correspond to greater eigenvalues, signifying a more significant magnitude of diffusion. Anisotropic diffusion is represented by an elongated ellipsoid, which signifies an increased mean diffusion distance along the longest axis of the ellipsoid. This is the characteristic behavior observed in the diffusion tensor ellipsoid when describing a cohesive axonal bundle, such as in white matter.

1.2 Diffusion-weighted Image acquisition

To generate FA and MD maps, the initial step involves the acquisition of diffusion-weighted images. The most common diffusion-weighting imaging (DWI) approach is the pulsed-gradient spin echo pulse sequence with a single-shot, echo-planar imaging (EPI) readout. The acquisition protocol is shown in Figure 1.5. In the simplest configuration,

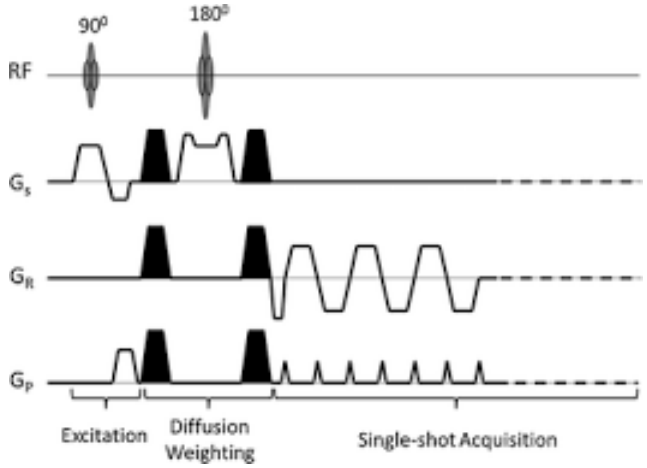

Figure 1.5: DW-SS-EPI pulse sequence where single-shot EPI acquisition is preceded by a slice selective excitation of 90° flip angle and a diffusion-weighting module. Image credit to [16].

this pulse sequence consists of a slice selection gradient during rf excitation, and then subsequent phase and frequency encoding gradients to cover all of k-space in a single shot. As shown in Figure 1.6, the first gradient pulse dephases the magnetization across the sample (or voxel, in imaging); the second pulse rephases the magnetization. For nondiffusing molecules, the phases induced by both gradient pulses will completely cancel, the magnetization will be maximally coherent, and there will be no signal attenuation from diffusion. Conversely, for molecules diffusing in the direction of the applied gradient, the bulk motion will cause the signal phase to change by different amounts for each phase; thus, there will be a net phase difference, which is proportional to the displacement, the area of the diffusion gradient pulses defined by the amplitude, G, the duration, δ, and the spacing between the pulses, Δ. As a result, the introduction of diffusion gradients leads to the accumulation of distinct phases for water molecules. MRI signals are directly related to the cumulative magnetization contributions of all water molecules within a voxel. Consequently, the scattering of phases due to diffusion results in signal attenuation. For simple isotropic Gaussian diffusion the signal attenuation for the diffusion gradient pulses

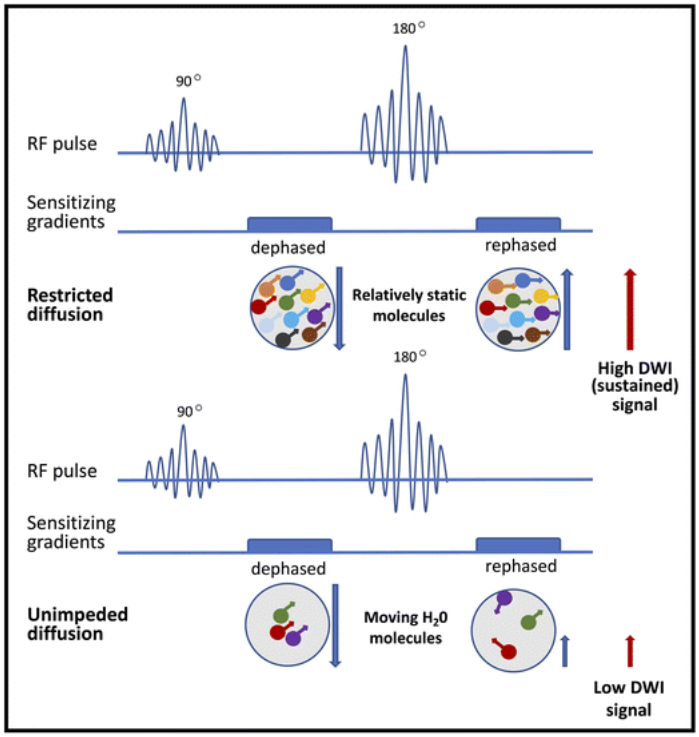

Figure 1.6: Schematic illustration of the principle of diffusion-weighted sequence acquisition, within high cell density tissue with restricted diffusion (top) and low cell density tissue with less restricted areas (bottom). DWI is an adaptation of a routine T2W pulse sequence with the application of two symmetric diffusion-sensitizing gradients (dephasing vs. rephasing) before and after the 180° RF pulse. Within a restricted-diffusion area, water protons do not move long distances. Hence, the rephasing cancels the phase shifts produced by the dephasing gradient, and there is no net loss in T2 signal intensity leading to a hyperintense signal on DWI. In contrast, water molecules move freely in areas with unimpeded diffusion (low cellularity), and by the time rephasing occurs, the protons have moved from their original location. This results in low signal intensity on DWI. DWI, diffusion-weighted imaging; RF, radiofrequency. Image credit to [17]

in Figure 1.5 is described by Eq.(1.5):

$$S = S_0 \cdot e^{-bD} \tag{1.5}$$

where S represents the diffusion-weighted signal, S_0 denotes the signal measurement obtained without applying any diffusion gradient, D corresponds to the apparent diffusion coefficient and b is the diffusion-weighting, referred to as the "b-value", described by the properties of the pulse pair in Eq. (1.6) [18]:

$$b = (\gamma G \delta)^2 \cdot \left(\Delta - \frac{\delta}{3}\right) \tag{1.6}$$

where γ is the gyromagnetic ration.
With the core DW pulse sequence defined as above, the following steps are automatically performed to generate DW images and their associated maps:

- The DW pulse sequence is first run with the diffusion gradients turned off or set to a very low value. This generates a set of $b0$ images and will serve as a baseline for later calculated maps;

- The DW sequence is then run with the diffusion gradients turned on individually or in combination and at various strengths. This produces DW source images sensitized to diffusion in multiple different directions.

- Further advanced processing can be optionally performed, creating calculated image sets for analysis (e.g., fractional anisotropy maps, principal diffusion direction maps, mean diffusivity maps, etc.)

1.3 Calculation of Apparent Diffusivities and Diffusion Tensor element maps

The first step in the calculation of the diffusivities maps, $D_{i,app}$, for each encoding direction. Equation (1.5) has to be adjusted to describe the signal attenuation for anisotropic diffusion with the diffusion tensor:

$$S_i = S_0 e^{-b\hat{g}_i D_{i,app}} = S_0 e^{-b_i D_{i,app}} \tag{1.7}$$

where S_i is the DW signal, the index i corresponds to a unique encoding direction, $\hat{g}_i$ is the unit vector describing the DW encoding direction, and b_i is the amount of diffusion weighting in (1.5). In the case of single diffusion weighting (b-value) and an image with very little or no diffusion weighting (S_0), the apparent diffusivity maps are estimated via [3]

$$D_{i,app} = \frac{ln(S_i) - ln(S_0)}{b_i} \tag{1.8}$$

Subsequently, the six independent elements of the diffusion tensor (D_{xx}, D_{yy}, D_{zz}, $D_{xy} = D_{yx}$, $D_{xz} = D_{zx}$ and $D_{yz} = D_{zy}$) may be estimated from the apparent diffusivities using multiple linear squares methods [19, 20] or nonlinear modeling [21].

Diffusion imaging in Anisotropic systems, with diffusion-enconding gradients applied along one axis results in rotationally variant image contrast. It is possible to obtain rotationally invariant images by computing all elements of the diffusion tensor matrix in equation 1.4 and, displaying scalar rotationally invariant properties of the tensor, such as the trace, denoted here as TR(D). It is possible to determine it by simply measuring the diffusivity in three orthogonal directions and adding these three diffusivities:

$$Tr(D) = D_{xx} + D_{yy} + D_{zz} \tag{1.9}$$

The minimum number of signal amplitude measurements required to estimate the trace in this way in this way is four: one measurement without diffusion-weighting, and one in each of three orthogonal directions. However, the number of measurements needs to be increased when dealing with highly anisotropic tensors. In this case, it can be seen that in the direction of least restriction, signal attenuation will be very high, while in the direction of greatest restriction, there will be much less signal attenuation, as also qualitatively explained above in the case of the different brain tissues. Given our lack of prior knowledge regarding tissue anisotropy or the variation in principal axis orientation across the image, optimizing measurements in individual directions becomes challenging. However, any inherent directional bias arising from measurements in a fixed set of orthogonal directions can be minimized by distributing measurements across the 3-dimensional

gradient vector space [22]. Via this method, the total number of measurements (N_{TOT}) for trace estimation is:

$$N_{TOT} = N_L + 3N_{sets} \tag{1.10}$$

where N_L is the number of measurements made at the low (or zero) b-value and N_{sets} is the number of three orthogonal gradient vectors. If more than one orthogonal set is employed, the minimum value of N_{TOT} is 7. This is also the number of measurements required to estimate all elements of the diffusion tensor matrix [22]. However, if the trace is the only measure of interest, it can be computed with much less computation, as it will be explained in Section 1.5.

1.4 Gradient Vector Orientations

Without prior knowledge about the orientation of the tensor, to optimize the relative orientations of sets of orthogonal gradient vectors, they should be uniformly distributed in the 3-dimensional space. Jones et a. [22] developed an algorithm to find the optimal arrangement of the N gradient vectors involving analogy with electrostatic repulsion.

The algorithm is explained as it follows: considers a model in which a line parallel to each gradient vector passes through the center of a sphere and a unit electrical charge is placed at both of the points where the line intersects the surface of the sphere. Each gradient vector is represented by a pair of points in this way because a diffusion attenuation measurement with the gradient in a positive direction could equally well have been performed with the gradient in the opposite direction since the diffusion tensor is symmetric in the absence of charged moieties.
The repulsive force between a pair of charges is, according to Coulomb's law, inversely proportional to the square of the distance between the charges. The algorithm used to arrange the gradient vectors uniformly in the 3-dimensional space therefore adjusts the orientations of the sets of orthogonal gradient vectors until the sum of the repulsive forces between every possible pair of charges is minimized. This is accomplished using the downhill method of Nelder and Mead [23].
In Figure 1.7, the table suggests some suitable gradient vectors when using 1, 2, and 3 sets of orthogonal gradient vectors.

Number of gradient vectors		x y z		Components of gradient vector orientation					
	1.000	0.000	0.000						
3	0.000	1.000	0.000	–	–	–	–	–	–
	0.000	0.000	1.000						
	1.000	0.000	0.000	−0.666	0.334	−0.667			
6	0.000	1.000	0.000	−0.333	0.667	0.667	–	–	–
	0.000	0.000	1.000	0.667	0.667	−0.333			
	1.000	0.000	0.000	−0.708	−0.503	−0.496	0.517	0.490	0.702
9	0.000	1.000	0.000	−0.706	0.508	0.493	0.475	0.518	−0.711
	0.000	0.000	1.000	0.004	0.699	−0.715	−0.713	0.701	0.035

Figure 1.7: Gradient unit vectors recommended by Jones et al. [22] for Estimating the Trace of the Diffusion Tensor using 1,2, and 3 sets of three orthogonal gradients.

1.5 Diffusion Tensor metrics

Visualizing and conveying tensor information in Diffusion Tensor imaging (DTI) is a significant hurdle due to the data's high dimensionality and intricate relationships within the diffusion tensor domain. This complexity poses a notable challenge in creating intuitive

and easily comprehensible representations. Typical approaches consist of reducing the dimensionality to one scalar (scalar indices) and to three dimensions (tractography). $2D$ visualization of scalar maps is used due to its simplicity and instant visualization. The two main diffusion indices, Mean Diffusivity (MD) and Fractional Anisotropy (FA) are based on the eigenvalues, which represent the magnitude of the diffusion process.
MD, ADC, or trace can be calculated by the mean of the three eigenvalues as shown in Equation (1.11).

$$MD = \frac{Tr(\mathbf{D})}{3} = \frac{\lambda_1 + \lambda_2 + \lambda_3}{3} \tag{1.11}$$

Mean diffusivity (MD) serves as an indicator of the collective magnitude of diffusion within a voxel. It quantifies the average movement of water molecules in all orientations, offering insights into the general diffusion properties, including the degree of restriction or hindrance to diffusion. MD does not convey any details regarding anisotropy or the preferred direction of diffusion. In order to describe the latter, FA is used. Fractional Anisotropy (FA) is a relative measure of diffusion anisotropy within a given voxel or region (see Eq. 1.12), which indicates the amount of diffusion in the principal direction compared to the orthogonal two directions. The values of FA are therefore unitless and inherently scaled between 0 (i.e., isotropic diffusion) and 1 (i.e., diffusion in only one direction).

$$FA = \sqrt{\frac{3\sum_{i=1}^{3}\left(\lambda_i - \langle\lambda\rangle\right)^2}{2\left(\lambda_1^2 + \lambda_2^2 + \lambda 3^2\right)}} \tag{1.12}$$

It was initially introduced by Basser and Pierpaoli [24] and has gained wide recognition in diffusion imaging studies. In practice, FA values consistently exhibit low values within gray matter and high values in most white matter areas. Still, conversely, they tend to be lower in specific white matter lesions [7]. It's crucial to recognize that the interpretation of FA values is intricate due to the presence of cerebral white matter voxels that contain complex fiber geometries and multiple fiber bundles oriented differently (such as crossing fibers, kissing fibers, etc) [7]. Besides that, a broad spectrum of other factors, including image noise (both thermal and physiologic [25, 26]), artifacts (e.g, misregistration of DW images from eddy currents or head motion) and partial volume averaging between tissues in large voxels (e.g., signal mixing of gray matter, WM and CSF [27]).

Furthermore, FA may not be enough to characterize tissue changes. Additionally, it's important to note that FA does not provide a complete description of the entire tensor shape or distribution. This is because different eigenvalue combinations can generate the same values of FA [28]. The tensor shape can, however, be described completely using a combination of spherical, linear, and planar shape measures [28, 29].

Despite these limitations, however, DTI is certainly a sensitive marker of neuropathology. Hundreds of research studies have observed reduced FA in a broad spectrum of diseases, with increases rarely reported. Furthermore, if the neuropathologic basis for a specific disease is understood, then results may be interpreted with greater specificity. For example, demyelination might cause the radial diffusivity ($D_r = \frac{\lambda_2+\lambda_3}{2}$) to increase, with minimal influence on the axial diffusivity ($D_a = \lambda_1$). Increased water in edema will increase the MD. Conversely, in complex diseases such as MS, brain regions may experience an unpredictable combination of demyelination, axon loss, gliosis, and inflammation, which could result in competing influences on the diffusion tensor [3].

Overall, FA and MD play a significant role in advancing our understanding of the brain's structure and function, providing complementary information on tissue microstructure.

1.6 Image distortions

Implementing DTI studies also involves the understanding of specific MRI acquisition artifacts, and how to deal with them. The artifacts in DWI datasets are mainly related to the gradient system hardware, pulse sequence, acquisition strategy used, and subject motion. In particular, even small amounts of the latter can lead to phase and amplitude modulations in the acquired data and significant ghosting artifacts in the reconstructed images. To reduce the influence of motion artifacts, the scan time can be reduced. This makes the use of Single-shot Echo Planar Imaging (EPI) [30, 31] the typical strategy employed to reduce this sensitivity because it is fast, efficient, and insensitive to small motions besides being readily available on most clinical MRI scanners.

Although EPI is the most common acquisition method for DWI, the disadvantages can be significant due to other artifacts related to EPI characteristics such as magnetic field inhomogeneities and eddy currents. Magnetic field inhomogeneities, typically caused by the susceptibility distribution of the subject's head (known as a susceptibility-induced off-resonance field) induce distortions in images if the anatomy of the brain, resulting in nonlinear warping along the phase-encoding direction. These distortions are often more pronounced in regions adjacent to interfaces between bone, air, and brain, such as the skull base, prefrontal regions, and the inferior temporal lobe near the auditory canal. The degree of this distortion is related to the local field variations, the echo spacing or readout bandwidth of the sampling in the phase-encoding direction, the direction of phase-encoding, and the field of view.

Susceptibility-induced distortions are proportional to the magnetic field strength. At 3T, the distortions can be quite severe [3]. EPI uses much longer (rising and falling edges of the gradients are separated in time) gradients; there might be perturbations of the local magnetic field that result in current inductions in the diverse conducting surfaces of the MRI scanner causing image distortions (contraction and/or overall shift and shear) that are usually easy to detect visually. Eddy currents vary with the diffusion gradient applied and, consequently, there will be misregistrations between successive images, which are worse with stronger and longer gradient pulses [32]. To a certain degree, the eddy currents may be reduced by exploiting strategies based on twice-refocused spin echo pulse, bipolar gradients, field maps and may also be retrospectively corrected using image registration methods [13, 33, 34].
Artifacts in DWI acquisitions lead to errors in tensor estimation and, consequently, in diffusion maps (FA and MD). Therefore, it is essential to fine-tune diffusion imaging sequences for greater data precision.

1.6.1 Protocol considerations

Protocols should be tailored to the specific research question, and distinct parameters should be employed to optimize the analysis for that particular purpose. There is no consensus on the optimal acquisition parameters because they vary according to MRI hardware configuration, field strength, vendor, scanning time available, specific anatomic structure, and brain anatomic coverage needed. However, previous technical review [35])provides suggestions for parameters in a typical DTI acquisition.
Diffusion tensor estimation requires high b-values (e.g., 1000 s/mm^2) along at least six non-collinear diffusion encoding directions in addition to one minimally non-weighted $b0$ image (b = 0 s/mm^2). Several sampling schemes have been suggested and it is argued

that the sampling vectors should be uniformly distributed in space so that the SNR is also uniform with respect to the tensor orientation. Most DTI studies use high b-values in the range of $700 - 1000 s/mm^2$, and the actual standard for clinical DWI is 1000 s/mm^2 [35]. The spatial resolution is also important for DTI quality and when using isotropic voxels (in-plane resolution and thickness with equal dimensions), typically, 2-2.5 mm are recommended. Anisotropic voxels also introduce bias in the quantitative assessment of fiber orientation and anisotropy and larger voxels are more likely to have more than one fiber tract orientation [35]. Other characteristic parameters of DTI acquisitions are Field of View (FOV) usually ranging from 240 to 256 mm and acquisition matrix 96 $\times$ 96 - 128 $\times$ 128. Echo Time (TE) and Repetition time (TR) may vary depending on the particular analysis. High-quality DTI data with whole-brain coverage, 2.5-mm isotropic resolution, and 64 diffusion encoding directions may be obtained in $\approx$ 15 minutes on clinical 1.5 T scanners [36]. Similar DTI data quality may be achieved almost one-quarter of the time at 3.0 T but the image distortions are roughly double [37].

Chapter 2

NODDI models

In this chapter, the description of the main models used for this study is presented. In particular, a brief introduction to the NODDI model is presented, followed by a detailed theoretical description of the Bingham-NODDI model and of the AMICO-NODDI model, which is the linear formulation of the NODDI model.

2.1 Bingham-NODDI model

Neurites are the extensions originating from the neuron's cell body, serving as the structural foundation for various brain functions. Neurite morphology, quantified using histological analysis of postmortem tissue, is the most accurate and reliable means for understanding the development [38], aging [39], the function [40] and pathology [41] of the brain. Accessing such information *in vivo* in humans has been of great interest as it can enable a dynamic view of the brain function and development, in health and disease. In this frame, diffusion magnetic resonance imaging (MRI) has become an essential tool, being able to non-invasively probe the microstructure of neurite morphology. In fact, despite being the standard diffusion MRI technique providing sensitivity to neurite morphology, DTI can not quantify neurite-specific measures, such as their density and orientation dispersion. Zhang et al. [8] enabled *in vivo* mapping of these measures with the development of the neurite orientation dispersion and density imaging (NODDI) model. NODDI has been tested in numerous clinical studies, showing the microstructure-specific indices provided to be clinically relevant.
NODDI is underpinned by a two-level multi-compartment model, as shown in Figure 2.1, where all compartments are assumed to be non-exchanging.
The total normalized signal, A, is modeled as the signal contribution from the tissue and non-tissue compartments of the brain, weighted by their respective relaxation-weighted volume fractions

$$A = (1 - \nu_{iso})A_{tissue} + \nu_{iso}A_{iso} \tag{2.1}$$

The non-tissue compartment represents the free diffusing water in the brain (e.g., CSF) and is modeled by free isotropic diffusion, with diffusivity d_{iso}. The volume fraction of this compartment is denoted by ν_{iso} and that of the tissue compartment by $(1 - \nu_{iso})$.
The signal from the tissue compartment, A_{tissue}, consists of the gray and white matter (GM/WM). A_{tissue} is the sum of the signal originating from inside the neurites (intra-neurite) and that from the space outside them (extra-neurite), weighted by their respective volume fractions

$$A_{tissue} = \nu_{in}A_{in} + (1 - \nu_{in})A_{en} \tag{2.2}$$

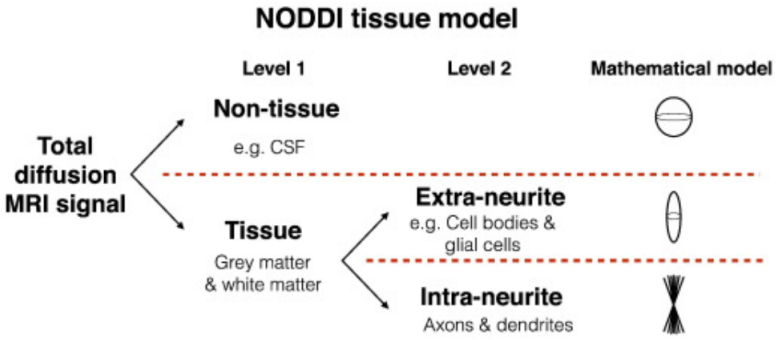

Figure 2.1: Breakdown of the total normalized diffusion MRI signal as modeled by NODDI. The contributions of the tissue and non-tissue components of the brain are modeled separately. The tissue signal is further broken down to account for the signal originating from the highly restricted neurites and the hindered space outside the neurites. The non-tissue compartment is modeled by isotropic Gaussian diffusion. The intra-neurite compartment models the neurites as orientationally dispersed sticks, while the space around the neurites is described as an anisotropic diffusion model. Image credit to *"Bingham–NODDI: Mapping anisotropic orientation dispersion of neurites using diffusion MRI"* [11].

where A_{in} and A_{en} are the normalised signals from the intra-neurite and extra-neurite compartments, respectively. The intra-neurite volume fraction gives an estimate of the neurites and it is indicated with ν_{in} while the extra-neurite volume fraction is $(1-\nu_{in})$, by construction. Specifically, neurites are modeled as sticks because in the typical time scale of diffusion MRI experiments, the membrane of neurites restricts the water diffusion to be along their length [42]. Therefore, the diffusion signal arising from a neurite in a specific orientation $\hat{n}$ is the reduction in signal strength caused by its unobstructed lengthwise diffusion, aligned with the direction of the applied gradient, i.e. $e^{-bd_i(\hat{q}\cdot\hat{n})^2}$. Here, b is the diffusion-weighting factor, $\hat{q}$ the gradient direction, and d_i the intrinsic diffusivity inside the neurites. To account for the orientational dispersion of neurites, we sum this attenuation over all possible orientations, given a certain density of neurites along each orientation, $\hat{n}$. So

$$A_{in} \int_{S^2} f(\hat{n}) e^{-bd_i(\hat{q}\cdot\hat{n})^2}\, dn \tag{2.3}$$

where $f(\hat{n})d\hat{n}$ is the probability of neurites with orientations within $d\hat{n}$. To account for hindrance due to the presence of neurites, the extra-neurite signal A_{en}, is modeled as signal attenuation due to anisotropic Gaussian diffusion [11], i.e.

$$A_{en} = e^{bq^T \hat{D}_{en} \hat{q}} \tag{2.4}$$

where D_{en} is the diffusion tensor representing the diffusion characteristics in the extra-neurite space. The effect of orientationally dispersed neurites on A_{en} is modeled by taking into account the following two observations:

- The dispersion of neurites has an effect on the diffusion in the extra-neurite space, with the diffusion perpendicular to the dominant orientation of neurites being greater if they have high dispersion

- Neurites hinder diffusion in the surrounding space and this hindrance is greater if the neurite density in that space is greater

The first observation implies that the extra- and intra- neurite spaces are coupled by the orientation distribution of neurites $f(\hat{n})$. Therefore

$$D_{en} = \int_{S^2} f(\hat{n}) D(\hat{n})\, dn \tag{2.5}$$

represents the diffusion tensor in the extra-neurite space in the presence of orientationally dispersed neurites, where $D_{\hat{n}}$ is a cylindrically symmetric tensor, with principal diffusion orientation $\hat{n}$, parallel diffusivity $d_{\parallel}$ and perpendicular diffusivity, $d_{\perp}$. $D_{\hat{n}}$ represents the standard configuration of parallel neurites along $\hat{n}$, for which we assume that the intrinsic diffusivity inside neurites is equal to that in the extra-neurite space, i.e. $d_i = d_{\parallel}$. To account for the second observation aforementioned, a tortuosity model [43] is used to estimate $d_{\perp}$, for a given neurite density, according to which $d_{\perp} = d_{\perp}(1 - \nu_{in})$.
In its current form, NODDI cannot accurately model complex neurite configurations such as those arising from fanning and bending axons (giving rise to anisotropic dispersion). In fact, the orientation distribution of neurites is modeled using the Watson distribution, which constrains the dispersion about the dominant orientation, $\hat{\mu_1}$, to be isotropic (figure 2.2a). Tariq et al. proposed the Bingham-NODDI model, able to extend NODDI formalism enabling the characterization of anisotropic orientation dispersion using Bingham distribution to quantify the orientation distribution of neurites. The Bingham dis-

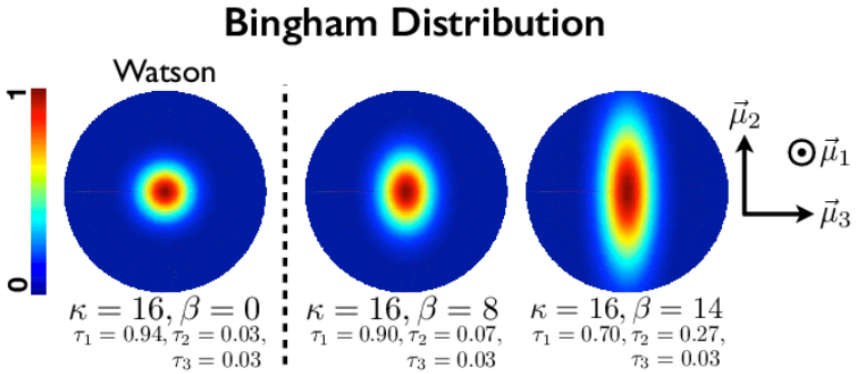

Figure 2.2: Schematic representations of Watson and Bingham distributions of sticks. Watson models isotropic dispersion and is a particular case of Bingham when concentration parameters $\kappa_1 = \kappa_2$. In the Bingham distribution instead $\kappa_1 > \kappa_2$. Image credit to *"Advanced dMRI Signal Modeling for Tissue Microstructure Characterization"*[11].

tribution is a parametric orientation distribution, which is the spherical analogue of a two-dimensional Gaussian distribution. The probability density of orientation along $\hat{n}$ for the Bingham distribution is defined in terms of a 3×3 symmetric matrix, $\mathbf{B}$

$$f(\hat{n}; \mathbf{B}) = \frac{1}{c_B} e^{(\hat{n}^T \mathbf{B} \hat{n})} \tag{2.6}$$

where c_B, the normalisation constant, is determined by

$$c_B =_1 F_1^1\left(\frac{1}{2}; \frac{3}{2}\mathbf{B}\right) \tag{2.7}$$

where ${}_1F_1^1$ is the confluent hypergeometric function of the first kind.
A geometrically interpretable form of (2.6) can be obtained expressing $\mathbf{B}$ in terms of eigendecomposition

$$\mathbf{B} = \begin{pmatrix} \hat{\mu}_1 & \hat{\mu}_2 & \hat{\mu}_3 \end{pmatrix} \cdot \begin{pmatrix} \kappa_1 & 0 & 0 \\ 0 & \kappa_2 & 0 \\ 0 & 0 & \kappa_3 \end{pmatrix} \cdot \begin{pmatrix} \hat{\mu}_1^T \\ \hat{\mu}_2^T \\ \hat{\mu}_3^T \end{pmatrix} \tag{2.8}$$

In this equation, the diagonal terms reflect the concentrations of orientations about the principal axes, $\hat{\mu}_1$, $\hat{\mu}_2$ and $\hat{\mu}_3$, as shown in Figure 2.2, with $\kappa_1 > \kappa_2 > \kappa_3$ [11]. The Bingham distribution is invariant to the addition of an arbitrary constant to its eigenvalues [44]. By choosing $-\kappa_3$ as the arbitrary constant, Equation (2.6) can be rewritten as in Equation (2.9), where $\kappa = \kappa_1 - \kappa_3$ and $\beta = \kappa_2 - \kappa_3$.

$$f(\hat{n}; \mathbf{B}) = \frac{1}{c_B} \exp\left(\kappa \left(\hat{\mu}_1 \cdot \hat{n}\right)^2 + \beta \left(\hat{\mu}_2 \cdot \hat{n}\right)^2\right) \tag{2.9}$$

In the study by Tariq et al., a more straightforward explanation of the orientation distribution is achieved by reformulating Equation (2.6) to resemble a two-dimensional Gaussian distribution. This results in the function expressed in Equation (2.10).

$$f(\hat{n}; \mathbf{B}) = \frac{e^{\kappa}}{c_B} \exp\left(-\frac{\left(\hat{\mu}_2 \cdot \hat{n}\right)^2}{1/\left(\kappa - \beta\right)}\right) \exp\left(-\frac{\left(\hat{\mu}_3 \cdot \hat{n}\right)^2}{1/\kappa}\right) \tag{2.10}$$

In the given equation, $1/\left(\kappa - \beta\right)$ and $1/\kappa$ represent the dispersion about the dominant orientation $\hat{\mu}_1$, specifically along $\hat{\mu}_2$ and $\hat{\mu}_3$ respectively. These dispersion parameters can be seen as analogous to the variance parameters in a Gaussian distribution, and they are inversely proportional to the concentration parameters κ and β. Specifically, since $\kappa \geq \beta$, the dispersion along $\hat{\mu}_3$ is either less than or equal to that along $\hat{\mu}_2$, as visually demonstrated in the density plot presented in Figure 2.2. Consequently, we refer to $\hat{\mu}_2$ as the primary dispersion orientation and $\hat{\mu}_3$ as the secondary dispersion orientation [11].

Tarie et a., defined a way to quantify the dispersion characteristics of neurites through the orientation dispersion index (ODI), specifically quantifying the dispersion extent along $\hat{\mu_1}$ with the parameter

$$ODI_P = \frac{2}{\pi} arctan\left(\frac{1}{\kappa - \beta}\right) \tag{2.11}$$

and that along $\hat{\mu_2}$

$$ODI_S = \frac{2}{\pi} arctan\left(\frac{1}{\kappa}\right) \tag{2.12}$$

As the value of β is increased for the same κ, resulting in an increase in anisotropic dispersion, ODI_P increases while ODI_S remains constant. Thus, while their absolute values indicate the level of dispersion, the relative values of ODI_P and ODI_S are an indicator of dispersion anisotropy.
To estimate the overall orientation dispersion, Tariq et al. [11] observed that the overall spread, or dispersion, of a multivariate normal distribution, can be quantified as the determinant of its covariance matrix, thus defining the index in Equation (2.13),

$$|\Sigma_{Bing}| = \sqrt{\left(\frac{1}{\kappa - \beta}\right)\left(\frac{1}{\kappa}\right)} \tag{2.13}$$

which can be mapped to a finite range giving a measure of total dispersion:

$$ODI = \frac{2}{\pi} \arctan\left(|\Sigma_{Bing}|\right) \tag{2.14}$$

ODI_{tot} measures the overall dispersion of neurite orientations within a voxel. A lower ODI_{tot} value indicates that neurite orientations are relatively aligned or coherent within the voxel, suggesting a more organized and uniform structure. In contrast, a higher ODI-tot value implies greater variability and dispersion in neurite orientations, indicating a more complex and disorganized structure. In white matter regions, lower ODI_{tot} values typically correspond to well-structured and densely packed axonal bundles, such as in the corpus callosum, where axons are highly aligned. Conversely, in areas with complex fiber geometries, like crossing or kissing fibers, you might observe higher ODI_{tot} values. In this frame, ODI_{tot} can be clinically relevant for assessing white matter integrity in various neurological conditions. Reduced ODI_{tot} values might indicate white matter damage or axonal loss, while increased ODI_{tot} values could suggest abnormalities in fiber organization, which may be related to neurodegenerative diseases or traumatic brain injuries.
In summary, ODI_{tot} values in the Bingham-NODDI model provide insights into the degree of neurite orientation dispersion within a voxel. These values have implications for white matter integrity, clinical diagnosis, and neuroscientific research, helping to characterize brain microstructure and connectivity.

2.2 AMICO-NODDI model

NODDI has been proven to be a powerful tool to estimate microstructural indices agreeing very well with known anatomical patterns observed within histology [8]. However, the non-linear routines usually employed to fit these models, as well as other diffusion modalities, are computationally very intensive and may cause practical problems for their application in clinical studies. Daducci et al., proposed the AMICO, standing for Accelerated Microstructure Imaging via Convex Optimization model, to reformulate microstructure imaging techniques as equivalent but in the convenient form of linear systems that can be solved efficiently using very fast algorithms [45].
In classical spherical deconvolution methods, the dMRI signal E(q) in each voxel is modeled as the convolution of a *fiber orientation distribution* (FOD) function with a response function $K(\cdot, \hat{u})$ corresponding to the signal attenuation of a single fiber with orientation $\hat{u}$ as shown in (2.15):

$$E(q) = E_0 \int_{S^2} K(q, \hat{u}) f(\hat{u})\, d\hat{u} \tag{2.15}$$

where E_0 is the signal without diffusion weighting and the integration is performed over the unit sphere S^2. The FOD can be expressed as a linear combination of N_k basis functions, also called atoms. When the response functions are known (or can be estimated) a priori, the measurement process can be expressed as a system of linear equations, as follows:

$$\mathbf{y} = \Phi\mathbf{x} + \eta \tag{2.16}$$

The variable, $\mathbf{y}$, represents the measured signal. The second variable, Φ, is the linear operator that explicitly models the convolution operation, also called dictionary, that consists of pre-generated signals that can be combined in a linear manner to estimate the measurement $\mathbf{x}$. The third variable, η, accounts for any noise that may be present during the acquisition process.

Daducci et al. proposed to decouple the reconstruction of the intra-voxel fiber geometry, i.e. number and orientation of fiber populations, from the assessment of their microstructure properties, i.e., diameter and density as this allows for breaking down the complexity of the original methods. In order to do so, the orientation of the major fiber is estimated by exploiting DTI, as they are well known for providing very accurate and robust reconstructions. Once the main orientation is known, it is possible to extend the linear operator Φ in (2.16) to account for the distinct water pools that arise from axons orientated in the main directions.
Specifically, in the NODDI model (as aforementioned), the anisotropy of the extra-cellular compartment is dictated by the density and orientation dispersion of the intra-cellular compartment; as a result A_{en} depends on both ν_{in} and κ, which are parameters to be estimated. This dependence makes it more complicated to formulate as a linear system. To linearize NODDI model, Daducci et al. [45] partitioned the dictionary into the following two blocks:

$$\Phi_N = \left[\Phi_N^t | \Phi_N^i\right] \tag{2.17}$$

In Equation (2.17) Φ_N^i models the isotropic contribution to the signal, while Φ_N^t accounts explicitly for the coupled intra- and extra-cellular compartments in the tissue. These sub-directories are constructed as follows:

- Each column in Φ_N^t represents the signal attenuation that results from a micro-environment with a unique density and orientation dispersion of the axons. In the context of the AMICO-NODDI model, the dictionary terms Φ_N are referred to as "atoms". As in Zhang et al. [8], the Watson distribution [44] is used to model the dispersion of white matter, and the longitudinal diffusivity is set to $d_{\|} = 1.7 \cdot 10^{-3}\, mm^2/s$.

- Isotropic contributions are modeled setting intrinsic diffusivity to the standard *in vivo* value of $d_{iso} = 3.0 \cdot 10^{-3}\, mm^2/s$.

Once we establish the linear dictionary, NODDI can be expressed as a convex optimization challenge:

$$\arg\min_{x \geq 0} \frac{1}{2} \left\| \tilde{\Phi}_N \mathbf{x} - \mathbf{y} \right\|_2^2 + \lambda \left(\frac{1}{2} \|\mathbf{x}\|_2^2 \right) + \gamma \left(\|\mathbf{x}\|_1 \right) \tag{2.18}$$

Equation (2.18) shows that the classical Tikhonov regularization is used in conjunction with the $\mathcal{L}_1$ norm to enhance problem stability.

Daducci et al. [45] developed an optimization strategy that follows three steps. First, the volume fraction of the isotropic compartment ν_{iso} is estimated by solving Equation (2.18) without regularization (i.e., $\lambda = \gamma = 0$). After that, the isotropic contribution to the dMRI signal is removed by subtracting $\tilde{\Phi}_N^i \nu_{iso}$ from $\mathbf{y}$ and solving Equation (2.18) with regularization terms. This step identifies the smallest subset of atoms needed to represent the signal, but the fitted coefficients $\mathbf{x}$ are not directly usable as they tend to

be biased due to the underestimation by the $\mathcal{L}_1$ norm. The final step involves debiasing the previously found solutions by solving Equation (2.18) again, without regularization, over the set of solutions previously identified.

Once this procedure has been carried out, the NODDI model parameters can be extracted using the following:

$$\nu_{ic} = \frac{\sum_{j=1}^{N_t} f_j \mathbf{x}_j^t}{\sum_{j=1}^{N_t} \mathbf{x}_j^t} \tag{2.19}$$

$$\kappa_{ic} = \frac{\sum_{j=1}^{N_t} \kappa_j \mathbf{x}_j^t}{\sum_{j=1}^{N_t} \mathbf{x}_j^t} \tag{2.20}$$

$$\nu_{iso} = \sum_{j=1}^{N_t} \mathbf{x}_j^t \tag{2.21}$$

The notation f_j and k_j is used to refer to the intra-cellular volume fraction and concentration parameter of the j-th atom in Φ_N^t, for $j \in \{1, \ldots, Nt\}$.
An example showing AMICO model metrics results and comparisons is shown in figure 2.3, as provided by Daducci et al., [45].

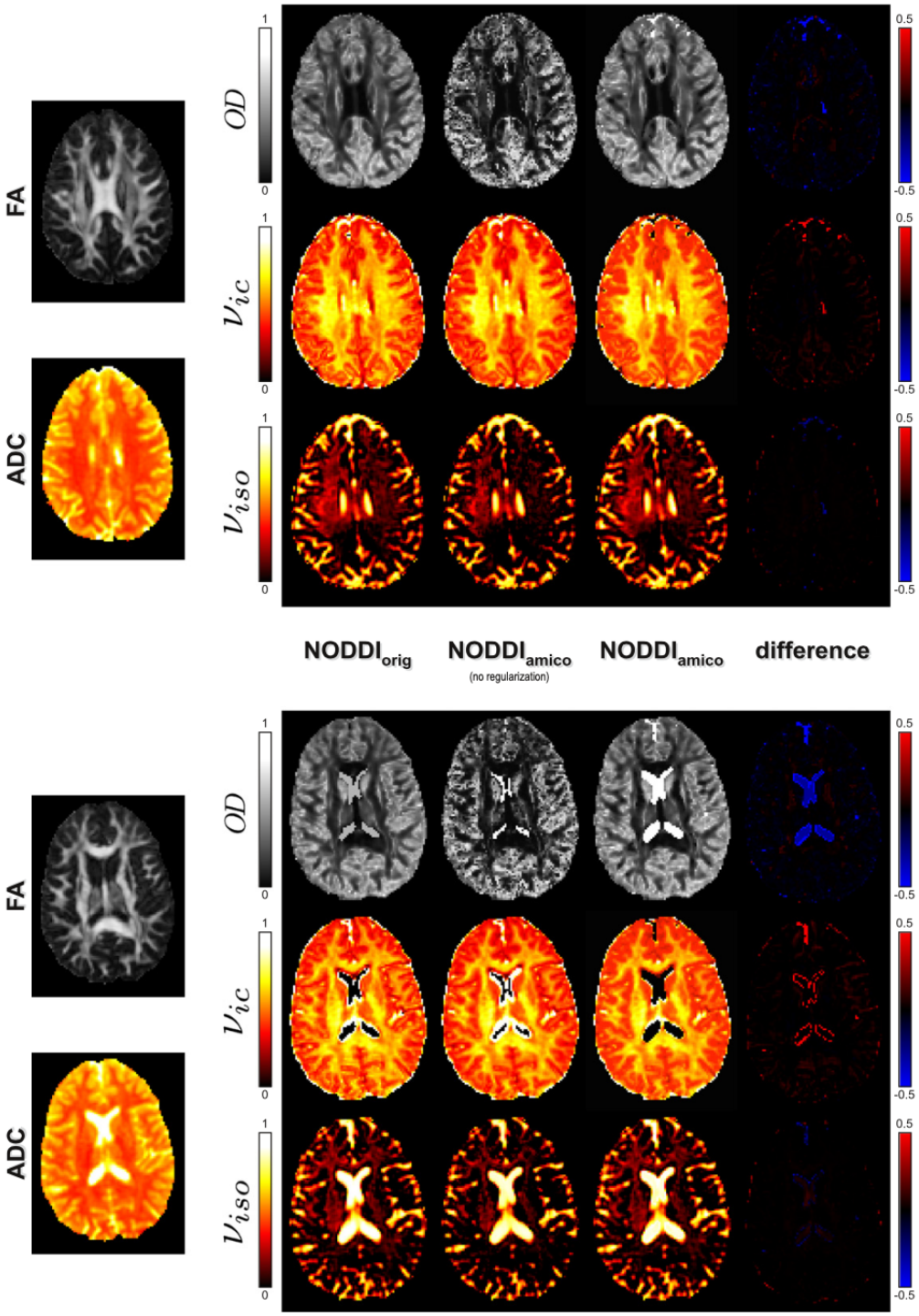

Figure 2.3: NODDI evaluation on the in-vivo human dataset. The microstructure parameters OD, $\nu_i n$ and ν_{iso} estimated with $NODDI_{orig}$ and $NODDI_{amico}$, both with and without regularization, are reported in two representative slices of the brain. The last column shows the difference between the corresponding $NODDI_{orig}$ and $NODDI_{amico}$ maps. FA and ADC maps extracted from standard DTI analysis are reported as references.

Materials and Methods

Chapter 3

DTI Phantom, subjects, MRI scanner systems and sequences

In this chapter, we delve into a comprehensive examination of the materials used in this study. Initially, we provide a detailed overview of the DTI phantom used in our research. Furthermore, we discuss the acquisition of brain diffusion-weighted MRI (dMRI) images for this study. Additionally, we present a comparative analysis of the technical specifications of various MRI scanners utilized in our research, with a focus on highlighting the key distinctions among them.

3.1 Phantom

Phantoms are essential in MRI studies and scanner comparisons to ensure data reliability and provide a foundation for making informed decisions about MRI scanner selection and optimization. For this study, in order to assess the consistency and reproducibility of diffusion results over time, a DTI Phantom called "basic phantom" has been used. This object has been scanned multiple times in different MRI Scanner systems (GE Signa Premier, GE Signa Artist, Siemens PRISMA). Specifically, the basic phantom has undergone two rescans (one after another) on each scanner on multiple days to investigate repeatability and/or noticeable differences of DTI model, Bingham-NODDI model and AMICO-NODDI model metrics results.

The "basic phantom" was manufactured by the German Cancer Research Center, Heidelberg (DKFZ) [46].
It is composed of a fibre ring with uniform anisotropy at each position, which is embedded in a homogeneous medium. Specifically, the phantom is made by winding polyamide fibres around an acrylic plastic spindle. The fibres are made of a synthetic, extremely fine polyester fiberfill of diameter 15 μm. The polyfill is made of filament yarn, specifically known as Filamentgarn TYPE 611. This type of yarn consists of continuous, long strands of polyester fibres, with a linear mass density of 50 decitex (dtex), indicating that 10000 meters of this yarn weigh 50 grams. Trevira GmbH, a company based in Bobingen, Germany, produces this polyfill. The fluid portion of the phantom is a mixture of distilled water and an aqueous sodium chloride solution (83 g NaCl per kilogram of water). This fluid constitution enables an orientation-independent and reliable use of DTI phantoms for evaluation purposes [46].
In Figure 3.2, it can be observed that the outer fibre strand has a diameter of $60mm$ and a thickness of $10mm$. Water is present between the fibres to simulate restricted anisotropic

(a) (b)

Figure 3.1: (a) Picture of the basic phantom that shows the part in which the fibre bundle is contained and the liquid in which it is immersed. (b) Top vision of the DTI basic phantom with a single fibre ring mimicking restricted anisotropic diffusion.

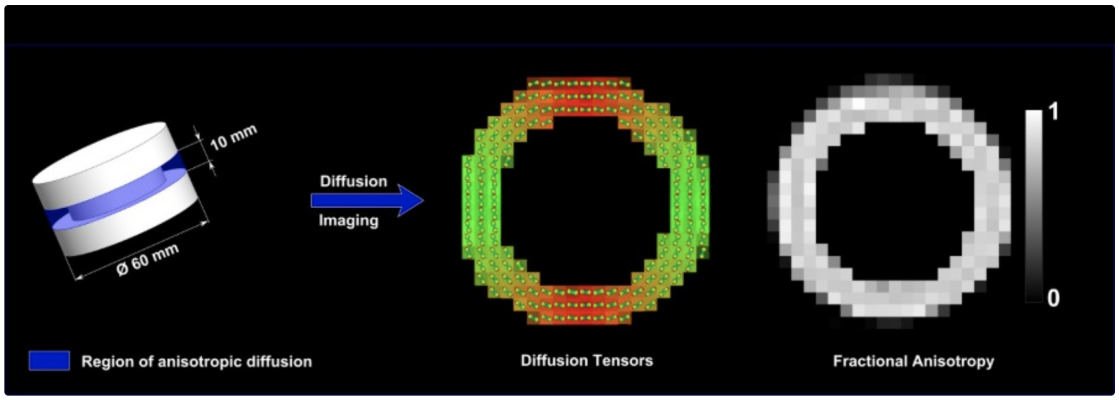

Figure 3.2: Detailed view of the plastic spindle, with the region of anisotropic diffusion highlighted in blue inside the basic phantom. On the right DTI metrics maps that can be obtained through phantom scans.

diffusion in the brain's white matter. The polyamide fibres winded around the plastic spindle are contained inside a cylindrical phantom container, shown in Figure 3.1a, of diameter $150mm$ and height $150mm$. According to the manufacturer's information, [46], the phantom was crafted using an automatic winding machine. This machine ensured a constant rotation speed and controlled horizontal movement that resulted in an even distribution of the thread over the spindle's width. Additionally, a counter kept track of the total amount of thread used. The achieved fractional anisotropy is 0.78 ± 0.02 [46]. The phantoms are scanned at the Oxford Centre for Clinical Magnetic Resonance Research (OCMR) and at the Churchill Hospital - University of Oxford - using the locally available 21-channel head and neck coil (General Electric Healthcare, Waukesha, WI, USA). The phantoms are positioned within the head coil with the cylinder's axis aligned parallel to the $B0$ field of the clinical scanner. Furthermore, the segment of the phantom housing the fibers must be centered at the scanner's isocenter.

3.2 MRI Scanner Systems

Phantom and brain scans were acquired with three different MRI scanner systems: two GE Signa systems, specifically GE Premier and GE Artist (General Electric Healthcare, Waukesha, WI, USA), and a Siemens PRISMA (Siemens Healthineers, Erlangen, Germany). For each MRI scanner, we obtained two sets of DWI image data. First, we acquired a dataset using a single-shell protocol, which exploits a single diffusion weighting value. Subsequently, we utilized a multi-shell protocol, involving multiple diffusion weighting values (to provide a comprehensive view of the diffusion process), to acquire another dataset.

3.2.1 GE Premier

Figure 3.3: Example of GE Premier 3 T scanner.

GE SIGNA^{TM} Premier (figure 3.3) is an ultra high-performance, 70 cm 3.0 T system. This system features a compact, lightweight, superconducting magnet designed to provide excellent homogeneity ensuring uniform signal and fat-suppression over a 50 cm FOV. GE Premier has a 3.0 T operating magnetic field strength with active magnet shielding and a cryogenic system for magnet cooling. It exploits a SuperG gradient coil which uses a hollow conductor, a water-cooled design for all axes, and a force-balanced layout to maximize overall gradient performance and minimize vibroacoustic effects on the patient. The SuperG Gradient Amplifier outputs 2.4MW of power to maximize outcomes in highly demanding cases. GE Premier gradient has Peak Amplitude = $80mT/m$ and Peak slew-rate = $200T/m/s$. At 3.0 T, precise control over the RF environment in a 70 cm patient bore has been challenging until now. The GE Premier RF transmit architecture consists of two liquid-cooled $15kW$ solid-state RF power amplifiers. By optimizing the phase and amplitude of each RF amplifier output channel that is applied to GE's 70 cm whole-body RF transmit coil, the RF uniformity and signal homogeneity are improved regardless of the patient's shape, size, and/or body habitus. In the Echo Planar Imaging sequence, a maximum of 320 diffusion gradient directions are available.

3.2.2 Siemens PRISMA

Siemens MAGNETOM^{TM} Prisma is a 3 T MRI scanner system. As the GE Premier, it has a magnet characterized by Peak amplitude = $80mT/m$ and slew rate = $200T/m/s$, simultaneously, on all axes. It is designed to work on a FOV of $50\times50\times50cm$ and to deliver quality and speed efficiently in MRI exploiting the combination of "Tim 4G" integrated coil technology and "Dot". The first is a RF system with 48 or 64 independent channels for faster imaging and it guarantees extended coverage, meaning no need to reposition for multiple exams, and more exams per day; the second is a system studied to adjust each exam to the patient's situation or clinical question at hand in order to reduce inter-subject variability and to provide accurate intra-subject rescans for increased statistical power.

Figure 3.4: Example of Siemens PRISMA 3 T scanner.

3.2.3 GE Artist

The SIGNA^{TM} Artist 1.5 T MRI scanner, as depicted in Figure 3.5, boasts a comprehensive array of features. It provides complete 360-degree coil coverage, advanced RF technology, and a direct digital interface equipped with an expanded number of channels. This system is highlighted by its magnet with a peak amplitude of $44mT/m$ and a slew rate of $200T/m/s$. It includes an innovative AIR^{TM} coil, which significantly reduces patient on-table time by 37% and streamlines patient setup by 59%. Additionally, the GE Signa Artist MRI system incorporates independent analog-to-digital converters for digitizing inputs from each of its 128 receive channels. This feature eliminates unnecessary noise amplification and enhances signal-to-noise ratio (SNR) by up to 25%. Moreover, the GE Artist magnet is engineered to reduce helium consumption by as much as 70% over its lifecycle, all while maintaining consistent and dependable performance.

3.3 Acquisition Protocol

In the following section, acquisition protocols are presented for each scanner. For this research, a DTI basic phantom and two healthy volunteers were scanned using two dif-

Figure 3.5: Example of GE Signa Artist 1.5 T MRI scanner.

fusion acquisition protocols: single-shell and multi-shell protocols. In diffusion weighting imaging (DWI) in MRI, single-shell acquisition involves acquiring data with diffusion gradients applied along a single direction or in a single shell of directions.
Single-shell acquisitions are simpler to implement and quicker to acquire compared to multi-shell acquisitions. They're often used in clinical settings where rapid imaging is crucial, such as in routine brain scans. Single-shell acquisitions can provide valuable information about diffusion. Multi-shell acquisitions involve acquiring data with diffusion gradients applied along multiple shells of directions. This allows for a more comprehensive assessment of tissue microstructure because different shells are sensitive to different ranges of diffusion characteristics.

The basic phantom also underwent multiple acquisitions using different echo times and b-values, to capture the correlation between TE and b-values with the tensor model metrics values, i.e. MD and FA.

3.3.1 Phantom and *In-vivo* studies

GE PREMIER - OCMR

The DTI protocol for the phantom study on the GE Premier consists of a single-shot, spin echo-based, and diffusion-weighted echo planar imaging sequence. The sequence includes a single refocusing pulse (180° pulse) with a repetition time (TR) equal to 6000 ms to allow for the acquisition of multiple slices during a single TR. For the single shell acquisition, the echo time (TE) has been set equal to 64.7 ms. Specifically, data acquisition was performed along 32 directions with a b-value = 1000 mm/s^2. In addition, one b = 0 image has been acquired, for critical assessment of signal intensity in the absence of diffusion weighting and the correction artifacts due to the B_0 inhomogeneities, eddy currents, and

subject motion. Regarding the multi-shell acquisition, the echo time was set equal to 76.9 ms. Data acquisition was performed on 90 distinct diffusion directions with two corresponding b-values: 30 directions with a b-value = 1000 mm/s^2 and 60 directions with a b-value = 2600 mm/s^2. In addition, 9 b = 0 images are randomly dispersed in between the diffusion-weighted images, for the same reasons as aforementioned. All images have a 2.5 mm^3 voxel resolution and the sequence used has been developed to reconstruct images to a voxel matrix of 96 × 96. Finally, the sequence is adapted to output the reversed polarity phase encode acquisition, a b = 0 volume acquired with the opposite phase encoding gradient direction compared to the diffusion-weighted volumes. This acquisition is exploited in the susceptibility-induced off-resonance field distortion correction step.
Imaging protocol for healthy volunteers includes a T1-weighted and diffusion-weighted scan. The subject left the scanner table at the end of each scanning session and then repositioned to be scanned for the second time, with the same acquisition protocol as the first scanning session. T1 weighted 3D volumes of the brain were acquired with a Magnetization Prepared RApid Gradient Echo sequence (MP-RAGE) with the following parameters for acquisitions of both healthy volunteers: TE/TR= 2.912/2584.12 ms, Inversion Time (IT) = 1058 ms, 0.79 number of averages, one Echo Train Length, pixel bandwidth equal to 244.141, and 1 mm^3 isotropic voxel resolution.
The diffusion-weighted sequence includes a single refocusing pulse with a repetition time (TR) of 6000 ms and an echo time (TE) of 71 ms. Diffusion data is acquired along 90 different directions with distinct b-values: 30 directions with a b-value = 1000 mm/s^2 and 60 directions with a b-value = 2600 mm/s^2. In addition, 9 b = 0 images are randomly dispersed in between the diffusion-weighted images. Just as for the phantoms, the voxel matrix size is 96 × 96 and each image has an isotropic voxel resolution of 2.5 mm^3. Furthermore, to enhance image quality, spectral fat saturation with non-spectral selective excitation was included in the sequence. This technique selectively suppresses fat signals, thus avoiding N/2 chemical shift ghosting artifacts which can cause the fat signal to appear displaced from its actual location, creating a duplication of structures and reducing image quality. Finally, for the brain acquisitions, the sequence was adapted to output the integrated reverse polarity phase encode acquisition.

SIEMENS PRISMA

Each set of scans on the Siemens Prisma MRI system included a Monopolar single-shell and a multi-shell acquisition, as well as a bipolar single-shell and multi-shell acquisition. As mentioned in Section 1.6, one approach to minimizing distortion from eddy currents is to modify the gradient pulse sequence by inserting additional gradients of opposite polarity is that individual eddy current effects are counterbalanced [47]. Specifically, the introduction of a second refocusing pulse to the conventional monopolar Stejskal and Tanner sequence permits the splitting of the original pair of diffusion gradients into two pairs of shorter pulses with opposite polarity, referred to as *bipolar*, as shown in Figure 3.6.
On the GE Premier MRI system, the bipolar sequence hasn't been employed as it would require large edits to the sequence to output the distortion uncorrected and the reversed polarity images. Additionally, it results in less efficient diffusion weighting.
For the single shell acquisition, the echo time (TE) has been set equal to 58 ms. Specifically, data acquisition was performed along 30 directions with a b-value = 1000 mm/s^2. In addition, one b = 0 image has been acquired, for critical assessment of signal intensity in the absence of diffusion weighting and the correction artifacts due to the B_0 inho-

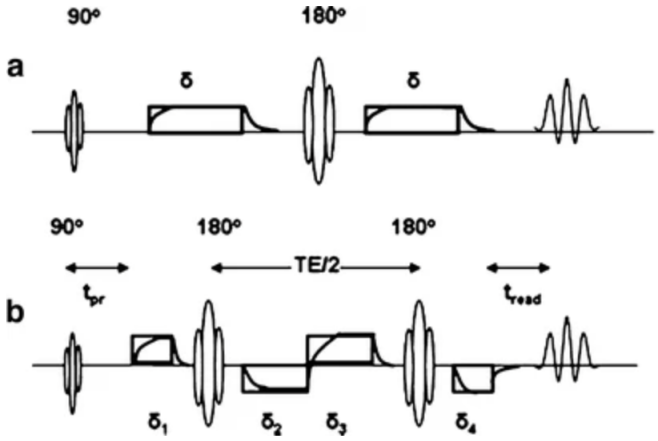

Figure 3.6: Schematic pulse sequence for the **a** single-refocused (monopolar) and **b** twice-refocused (bipolar) spin-echo diffusion-weighted experiments. *Boxes* represent motion-probing gradient pulses of equal magnitude but different durations δ; The curves superimposed on the boxes signify build-up/down of the gradient magnetic field, which is responsible for the generation of eddy currents. The echo time (TE) in the bipolar sequence has to include the preparation time before the application of the gradient pulses (t_{pr}) and the readout time before the formation of the echo (t_{read}). Image credit to [47].

mogeneities, eddy currents, and subject motion. Regarding the multi-shell acquisition, TE/TR = 69/6000 ms (monopolar) and TE/TR = 81/6400 ms have been set. Data acquisition was performed on 90 distinct diffusion directions with two corresponding b-values: 30 directions with a b-value = 1000 mm/s^2 and 60 directions with a b-value = 2600 mm/s^2. In addition, 9 b = 0 images are randomly dispersed in between the diffusion-weighted images, for the same reasons as aforementioned. All images have a 2.5 mm^3 voxel resolution and the sequence used has been developed to reconstruct images to a voxel matrix of 96 × 96, this allows to avoid image data interpolation. Finally, the sequence is adapted to output the reversed polarity phase encode acquisition, b = 0 volumes were acquired with the opposite phase encoding gradient direction compared to the diffusion-weighted volumes and the first volume has been selected with a script for the processing of the data as it will be better explained in the next chapter regarding data analysis. This acquisition is exploited in the susceptibility-induced off-resonance field distortion correction step. Regarding *in-vivo* acquisitions, the MP-RAGE parameters set during the acquisitions performed on both healthy volunteers were: TE/TR/IT = 4.73/2200/1110 ms, one average, pixel bandwidth equal to 130, and 1 mm^3 isotropic voxel resolution.
The diffusion acquisition protocol for *in-vivo* brain analysis is congruent with the one used on the GE Premier as described in Subsection 3.3.1 as data were acquired along 90 different directions. For the *in-vivo* acquisition, the single-refocused (monopolar) spin-echo sequence was used.

GE ARTIST

Acquisition were performed on a GE Artist scanner, located at the Churchill Hospital - University of Oxford - to better compare results from two 3.0 T MRI scanner systems with a 1.5 high-field MRI scanner system. The DTI protocol for the phantom study on the

GE Artist consists of a single-shot, spin echo-based, and diffusion-weighted echo planar imaging sequence. The sequence includes a single refocusing pulse (180° pulse) with a repetition time (TR) equal to 6000 ms to allow for the acquisition of multiple slices during a single TR. For the single shell acquisition, the echo time (TE) has been set equal to 83.5 ms. Specifically, data acquisition was performed along 32 directions with a b-value = 1000 mm/s^2. In addition, one b = 0 image has been acquired, for critical assessment of signal intensity in the absence of diffusion weighting and the correction artifacts due to the B_0 inhomogeneities, eddy currents, and subject motion. Regarding the multi-shell acquisition, the echo time was set equal to 105 ms. Data acquisition was performed on 90 distinct diffusion directions: 30 directions with a b-value = 1000 mm/s^2 and 60 directions with a b-value = 2600 mm/s^2. In addition, 9 b = 0 images are randomly dispersed in between the diffusion-weighted images, for the same reasons as aforementioned. All images have a 2.5 mm^3 voxel resolution and the sequence used has been developed to reconstruct images to a voxel matrix of 96 × 96, this allows to avoid image data interpolation. Finally, the sequence is adapted to output the reversed polarity phase encode acquisition, a b = 0 volume acquired with the opposite phase encoding gradient direction compared to the diffusion-weighted 32 volumes. This acquisition is exploited in the susceptibility-induced off-resonance field distortion correction step. Our *in-vivo* analysis exclusively utilized data acquired from the GE Premier and Siemens Prisma MRI systems, without acquiring data from the GE Artist system.

3.3.2 Multiple TE and b-values Phantom Study

Part of this study involved multiple echo time (TE) phantom acquisitions. In particular, the DTI basic phantom underwent eight consecutive scans with different echo times, spaced by 10 ms each, starting from a TE = 56.3 ms to a TE = 126 ms. For this study, other imaging parameters set are: isotropic voxel resolution of $2.5mm^3$ and echo train length equal to one. For each acquisition, one average was acquired and a single-shell acquisition protocol was used, with a diffusion weighting equal to 1000 s/mm^2.

The investigation proceeds with a set of acquisitions using a multi-slice (32 volumes) single-shell and a multi-shell (298 volumes) protocol exploiting multiple b-values. In particular, the b-values used for this study are: 100 s/mm^2, 200 s/mm^2, 400 s/mm^2, 600 s/mm^2, 800 s/mm^2, 1000 s/mm^2, 1500 s/mm^2, 2000 s/mm^2 and 2600 s/mm^2. For each b-value, 32 volumes were acquired. The acquired was then fitted to the tensor and Bingham-NODDI model.

3.4 FSL

All data used in this study have been processed exploiting the features of **FSL** [48]. FSL is a comprehensive library of analysis tools for FMRI, MRI, and diffusion brain imaging data developed in Oxford, UK. Because of its reliability, adaptability, and broad range of capabilities, FSL is widely employed in the neuroscience and medical imaging fields. Regarding image distortions, FSL includes the TOPUP and EDDY tools. The TOPUP method is used to correct the susceptibility-induced off-resonance field. As described in 1.6, is one of the most common artifacts affecting diffusion-weighted spin-echo EPI images. To a first approximation, the susceptibility-induced field will be constant for all acquired images, implying that the set of images will be internally consistent.

It is a problem because it will result in a geometric mismatch between the structural images (which are typically unaffected by distortions) and the diffusion image. TOPUP estimates the susceptibility-induced off-resonance field using two images acquired with different polarities of the phase-encoding gradient. In this way, the same field produces distortions in opposite directions in the two acquisitions, as shown in figure 3.7.

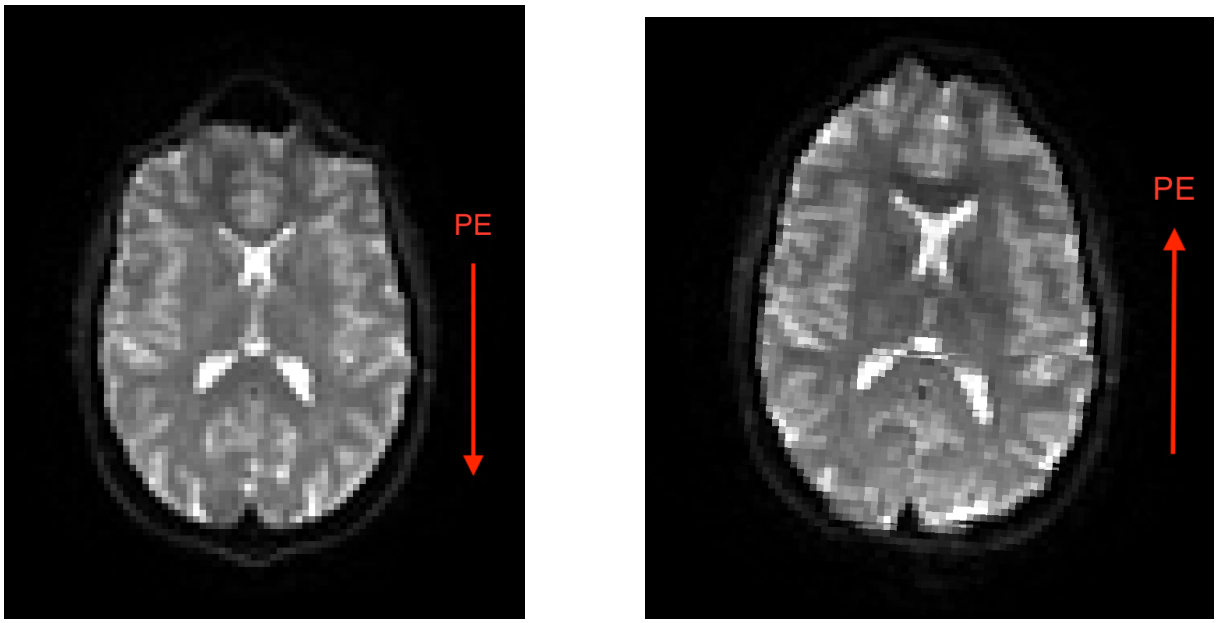

(a) Phase Encoding gradient AP

(b) Phase Encoding gradient PA

Figure 3.7: Example of DWI images exhibiting notable distortions due to B_0 inhomogeneities. The image on the left displays compression of the frontal area, attributed to the application of a phase encoding gradient directed from the Anterior to the Posterior part of the brain. Conversely, the image on the right demonstrates elongation of the frontal area due to the application of a phase encoding gradient directed from the Posterior to the Anterior part of the brain.

TOPUP finds the field that, when applied to the two volumes, maximizes the similarity of the unwarped images. The similarity is gauged by the sum-of-squared differences between the unwarped images. This measure allows to use of Gauss-Newton for jointly finding the field and any movement that may have occurred between the two acquisitions [49]. To correct for eddy currents, the EDDY tool implemented in FSL can be used.

EDDY estimates the eddy current-induced distortions and movements on the image, starting from the TOPUP fieldmap [50]. It also, optionally, performs outlier detection to identify slices where signal has been lost as a consequence of subject movement during the diffusion encoding. These slices are replaced by non-parametric predictions by the Gaussian Process that is at the heart of EDDY.
Figure 3.8 shows a comparison between the original diffusion-weighted image (i.e., GE Premier (OCMR) brain acquisition) and the final EDDY-corrected image. On the brain study, an automated quality control assessment (QC) has been performed exploiting the EDDY QC tool, implemented in FSL. This process is of great importance to detect data acquisition and pre-processing issues. The automated EDDY QC framework allows to assess dMRI data both at the single subject and group levels after the TOPUP and EDDY correction stages have been performed. Using this framework it is possible to

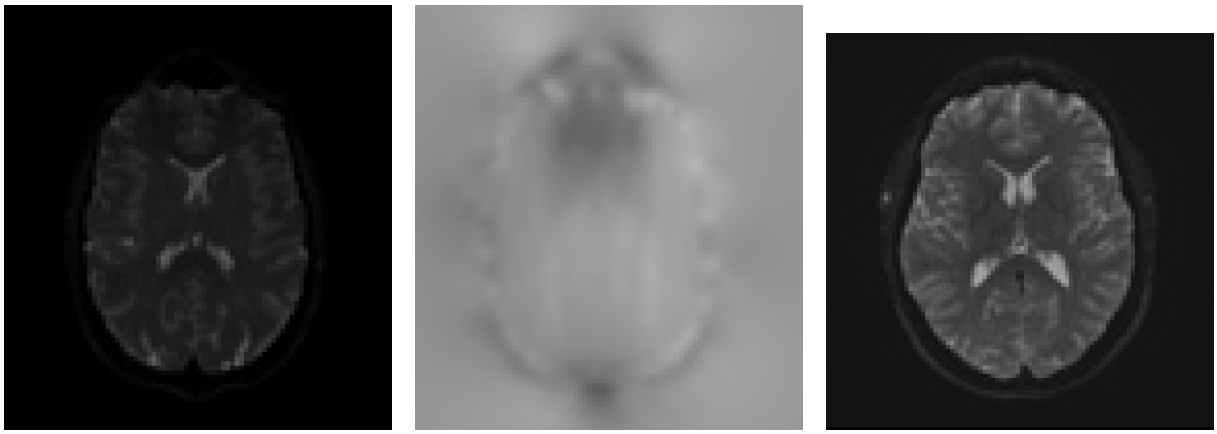

(a) (b) (c)

Figure 3.8: (a) Image of the original diffusion-weighted image of the brain (GE Premier), in which it appears to be warped, notably along the phase encoding gradient direction. (b) The TOPUP fieldmap. (c) The corrected DW-image.

distinguish between good and bad quality datasets and, importantly, identify subsets of the data that may need careful visual inspection [51]. This tool produces a single-subject quality control report.

Chapter 4

Models implementation

This chapter describes the practical implementation of the software tools used to process and analyze MRI data acquired in this study.

First, the implementation of the tensor model to the DW-MRI data is explained. In particular, to fit the tensor model, the function `dtifit` of the FMRIB Software Library (FSL) [48] has been used, a well-known software suite in the neuroimaging community. The implementation of this function has been done by integrating FSL into Python exploiting the flexibility features of the *fslpy* library.

Therefore, the implementation of the Bingham-NODDI model [11] is described. This has been done by using the Dmipy library, an open-source Python program built to model and analyze diffusion magnetic resonance data through multi-compartment modeling methodologies.

The final section describes the implementation of the AMICO-NODDi model [45] using resources from the AMICO repository, publicly available on Github (`https://github.com/daducci/AMICO`).

The codes used for this study have been developed previously in collaboration with the University of Oxford (focused on analysis of data acquired on a single MRI scanner) and properly adapted for this study, aiming at expanding our investigation to encompass reliability of the Bingham-NODDI model on multiple MRI scanners.

4.1 Tensor model

The tensor model was applied through the utilization of the FMRIB Software Library (FSL), a versatile and extensively adopted software suite tailored for the analysis of both functional and structural neuroimaging data, with a particular emphasis on MRI techniques [52, 53, 48]. As aforementioned in 3.4, FSL is largely used in the neuroscience and medical imaging fields as it provides a variety of tools and utilities for processing neuroimaging data, among which DW-MRI data.
To fit diffusion tensor on eddy-corrected diffusion-weighted MRI data, the `dtifit` command is used. This command estimates the diffusion tensor parameters, as described in 1.1, that are the three eigenvalues λ_1, λ_2 and λ_3 of the diffusion tensor matrix, corresponding to the magnitude of water diffusion in the tissue microstructure's principal directions and the three principal directions $\vec{\mu_1}$, $\vec{\mu_2}$ and $\vec{\mu_3}$. Once this has been done, Mean Diffusivity (MD) and Fractional Anisotropy (FA) are computed, according to equations (1.11) and (1.12), with the ultimate goal of obtaining information about the tissue

integrity through diffusion properties.

`dtifit` would be typically run on data that has been pre-processed and eddy current corrected. As input, the command needs:

- Diffusion weighted data (data): Diffusion data is usually stored in 4D NIFTI (.nii) file, where each volume is acquired with a different b-value and/or gradient orientation. This will include diffusion-weighted volumes and volume(s) with no diffusion weighting.
- A brain/phantom mask: A single binarised volume in diffusion space containing ones inside the brain and zeroes outside the brain.
- output basename: User specifies a basename that will be used to name outputs of the `dtifit`.
- Gradient directions (bvecs): An ASCII text file containing a list of gradient directions applied during diffusion-weighted volumes.
- b values (bvals): An ASCII text file containing a list of b values applied during each volume acquisition.

The outputs of `dtifit` are:

- $< basename >\_V1$ - 1st eigenvector
- $< basename >\_V2$ - 2nd eigenvector
- $< basename >\_V3$ - 3rd eigenvector
- $< basename >\_L1$ - 1st eigenvalue
- $< basename >\_L2$ - 2nd eigenvalue
- $< basename >\_L3$ - 3rd eigenvalue
- $< basename >\_MD$ - mean diffusivity
- $< basename >\_FA$ - fractional anisotropy
- $< basename >\_MO$ - mode of the anisotropy
- $< basename >\_S0$ - raw T2 signal with no diffusion weighting

FSL has been implemented in Python, exploiting the `fslpy` package. The `fslpy` project is an FSL programming library written in Python. This package contains all the Python functions which can be used to invoke FSL commands. FSL may thus be easily accessed and integrated into the rest of the programming needed to analyze the collected data using Python commands. The `fslpy` complete documentation can be found at `https://open.win.ox.ac.uk/pages/fsl/fslpy/index.html#`.

4.2 Bingham-NODDI model

The first implementation of Neurite Orientation Dispersion and Density Imaging, also known as Watson-NODDI, was accomplished through a package of functions called the 'NODDI toolbox' in MATLAB, created by The Mathworks company in Natick, USA. The toolbox can be accessed at `http://mig.cs.ucl.ac.uk/index.php?n=Download.NODDI`. This toolbox allows users to select from a variety of biophysical models. The original code was written in Matlab, for this work it has been adapted to Python. In this project, collaborative Python scripts were developed through a partnership between the University of Bologna and the University of Oxford. These scripts were designed to process and analyze Diffusion Weighted-Magnetic Resonance Imaging (DW-MRI) data obtained at the Oxford Centre for Clinical Magnetic Resonance Research (OCMR) using various MRI scanner systems.
Initially tailored for the 3T GE Premier scanner at OCMR, the scripts underwent modifications to accommodate different MRI scanner systems, including Siemens Prisma and GE Artist. This adaptation involved adjusting configuration files and meticulously fine-tuning each step of the scripts. Detailed information on these adjustments is provided in the subsequent sections.
The input diffusion-weighted images must be in the *.nii* format, and the b-values and gradient directions must be provided in separate *.bval* and *.bvec* files. Additionally, a binary brain mask in *.nii* format is required, and the user must specify the name of the model to be fitted.

The Dmipy (Diffusion Microstructure Imaging in Python) software package facilitates the reproducible estimation of diffusion MRI-based microstructure features. It does this by taking a completely modular approach to Microstructure Imaging. Dmipy's main features include:

- Any combination of tissue models (e.g. Gaussian, Cylinder, Sphere) and axon bundle representation (e.g. orientation-dispersed/diameter-distributed) can be combined into a multi-compartment model.
- Any appropriate model can be orientation-dispersed and/or axon diameter-distributed.
- Any predefined or custom parameter constraints or relations can be imposed.
- Fit the spherical mean of any multi-compartment model to the spherical mean of the data.

So Dmipy is a powerful tool with which any microstructure model can be assembled, as shown in figure 4.1.
Dmipy is used for the implementation of the Bingham-NODDI model [11] using the following mathematical structure (4.1):

$$S = \underbrace{f_{\text{CSF}} \overbrace{S_{\text{iso}}(\cdot|D_{\text{CSF}})}^{\text{Ball}}}_{\text{CSF}} + \overbrace{B(\kappa_1, \kappa_2, \boldsymbol{\mu}_i)}^{\text{Bingham}} *_{\mathbb{S}^2} \left[\underbrace{f_{\text{en}} \overbrace{S_{\text{en}}(\cdot|\lambda_\perp^{\text{tort}}, \lambda_\parallel^{\text{tort}})}^{\text{Zeppelin}}}_{\text{Hindered Extra-Axonal}} + \underbrace{f_{\text{in}} \overbrace{S_{\text{in}}(\cdot|\lambda_\parallel)}^{\text{Stick}}}_{\text{Intra-Axonal}} \right] \tag{4.1}$$

The total diffusion signal is implemented exploiting multiple models: CSF compartment is represented using the Ball model, an isotropic Gaussian compartment whose signal attenuation only depends on isotropic diffusivity λ_{iso} [48]. The extra-neurite compartment is

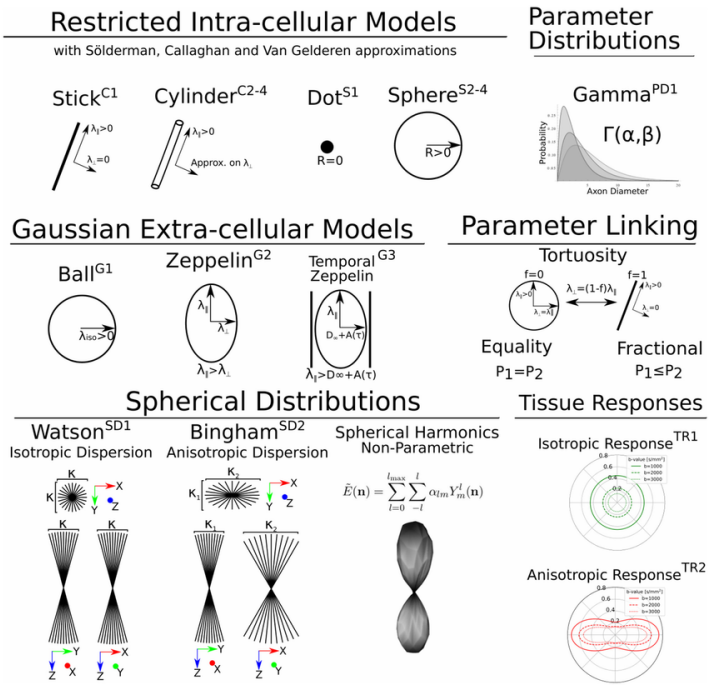

Figure 4.1: A schematic representation of most biophysical models that are used in PGSE-based Microstructure Imaging. Using different combinations of these "components," any microstructure model can be assembled using Dmipy. Image credit [54]

.

described as the Zeppelin component, an axially symmetric Gaussian distribution aligned along orientation $\hat{\mu}$, with parallel and perpendicular diffusivity $\lambda_{\parallel} \geq \lambda_{\perp}$, often used to describe the diffusion signal originating from the oriented, extra-axonal space [48]. Finally, the intra-neurite compartment is modelled as a Stick, a cylinder with a diameter of zero. It has Gaussian diffusivity $\lambda_{\parallel}$ along the cylinder's axis and $\lambda_{\perp} = 0$ perpendicular to the axis [48]. As already mentioned, the Bingham-NODDI model uses the Bingham distribution to capture the orientation distribution of the tissue compartment, defined as an anisotropic Gaussian distribution on the sphere with orientation μ and primary and secondary concentration concentrations κ_1 and κ_2. The schematic representation of the implementation of the Bingham-NODDI model as just described is shown in Figure 4.2.

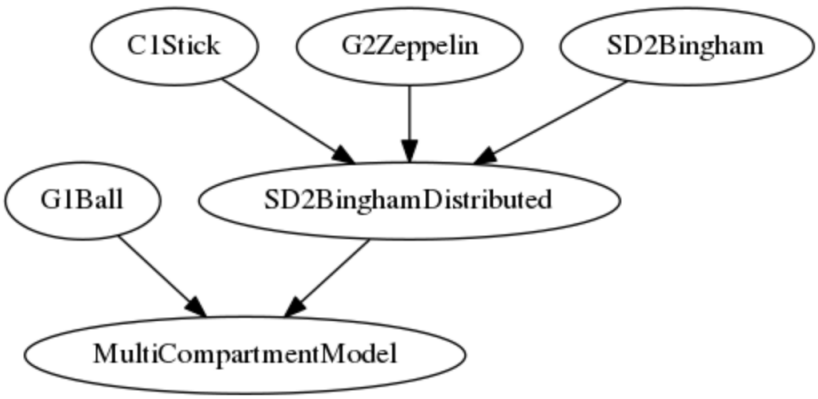

Figure 4.2: Schematic representation of the Bingham-NODDI model Dmipy implementation.

To describe the neurite concentration, the optimisation parameters ODI and β-fraction are used. The ODI is defined in Equation (2.14), while the β-fraction is defined as follows:

$$\kappa_2 = \beta \cdot \kappa_1 \tag{4.2}$$

As described in Equation (4.2), β-fraction is used to characterise the degree of dispersion in the secondary direction within the Bingham distribution.
To fit Bingham-NODDI model, th following inputs are required:

- Preprocessed Difussion-weighted data: NIFTI format files DW data
- Gradient directions (bvecs): An ASCII text file containing a list of gradient directions applied during diffusion-weighted volumes.
- b values (bvals): An ASCII text file containing a list of b values applied during each volume acquisition usually supplied in s/mm^2, but in this case they have to be converted to s/m^2.
- A brain/phantom mask: A single binarised volume in diffusion space containing ones inside the brain and zeroes outside the brain.

As outputs, the Bingham-NODDI model fit produces a variety of quantitative maps: the tissue volume fraction map, indicating the portion of tissue proportion within each voxel; the intra-neurite volume fraction map, indicating the portion of voxel occupied by neurites. The beta fraction map and the Orientation Dispersion Index (ODI) map, representing the degree of dispersion or coherence of neurite orientations within each voxel. It also provides the mean squared error (MSE) and the R^2 maps are provided to assess the goodness of the fit.

4.3 AMICO-NODDI model

Fitting the Bingham-NODDI model takes on average 13 hours. The process may be reduced when fitting results using a binary mask from a specific region, like it has been done in this study and explained in the next section. The AMICO-NODDI model is a linearized version of the NODDI model and is publicly available (`https://github.com/daducci/AMICO`). This model, in order to be fit, needs a precise folder structure, as shown in figure 4.3.

```
├─ data
    ├─ Study_01                --> all subjects acquired with protocol "Study_01"
        ├─ Subject_01
        ├─ Subject_02
        ├─ ...
    ├─ Study_02                --> all subjects acquired with protocol "Study_02"
        ├─ Subject_01
        ├─ Subject_02
        ├─ ...
    ├─ ...
```

Figure 4.3: AMICO assumed folder structure when fitting the model.

Subjects' data acquisitions should be organized within the dataset's root directory, with each subject's data allocated to a dedicated subfolder identified by their corresponding

diffusion protocol. This scheme is necessary in order to improve computation efficiency. For each diffusion weight (i.e., b-value), AMICO generates a large number of probable dictionary terms known as 'kernels' with high angular resolution, which are shared among participants scanned with equal diffusion weighting, regardless of the number of DW images acquired within the dataset. After generating the kernel, the set of synthetic signals is resampled to align with the real gradient directions and can subsequently be utilized for model fitting within the dictionary. This process ensures that patients participating in the same study, who underwent scanning using the same diffusion protocol, will share identical pre-computed kernels stored in memory. In this way, the fitting process is more efficient since producing the kernels is the most computationally significant part.

Fitting AMICO-NODDI requires the following inputs:

- Preprocessed DW data in the *.hdr / .img* format
- Gradient directions (bvecs): An ASCII text file containing a list of gradient directions applied during diffusion-weighted volumes.
- b values (bvals): An ASCII text file containing a list of b values applied during each volume acquisition
- A *.hdr / .img* format of the brain/phantom mask: A single binarised volume in diffusion space containing ones inside the brain and zeroes outside the brain.

Fitting AMCIO-NODDI takes on average 5-10 minutes, dramatically reducing the time required by the Bingham-NODDI model fit, and providing a useful tool to neuroscientists and researchers.

Chapter 5

Processing of data

This chapter provides a comprehensive exploration of the data pipeline, commencing with the analysis of phantom data and proceeding to the examination of in-vivo brain data. For this work, Python scripts were written by Mattia Ricchi to process and analyze DW-MRI collected at the Oxford Centre for Clinical Magnetic Resonance Research (OCMR) with the 3T GE Premier and adapted in this study to work with multiple MRI scanners. All the in-house Python scripts used in this work for processing and analyzing the acquired data can be found on the GitHub page Oxford Molecular Imaging.

In the first part of this chapter, the focus is on the steps required to process the DTI 'basic phantom' data collected on multiple scanners. The second part focuses on the processing pipeline of the *in-vivo* brain data.

5.1 Phantom Study

For this work, a DTI 'basic phantom' has been used, as described in Section 3. The phantom underwent multiple MRI scans across various days, with two scans performed on each occasion, to evaluate the consistency of both the Tensor model and the Bingham-NODDI model outcomes across time and different MRI scanners. Prior to the fitting process, data required preprocessing, and this task was efficiently accomplished in a single Python script, thanks to the capabilities of the `fslpy` library.
Each acquisition comprised two subacquisitions: a singleshell acquisition and a multishell acquisition, as detailed in the acquisition protocol Section 3.3. These subacquisitions underwent separate processing. Specifically, the tensor model was fitted for both single shell and multishell acquisitions, while the Bingham-NODDI and AMICO-NODDI models were exclusively fitted to the multishell acquisitions. The subsequent pipeline was consistently applied to datasets obtained from various MRI scanners, and any specific adjustments will be comprehensively detailed.

The first step is the correction of the artefacts produced by the local inhomogeneities of the B_0 field. This is done by the TOPUP tool, as explained in section 1.6, available in the `fslpy` library and called in the Pyhton script with the **topup** command. For the correction to be performed, it needs to load the first volume of the DTI data and of the reverse phase-encoded DTI data in a 4D array. Specifically, in certain instances, the phantom data obtained on the Siemens Prisma differ from those acquired on the GE Premier, as they are obtained in sets comprising more than one volume. As a result, a Python script has been developed for this study to specifically extract the initial volume

of the reverse phase-encoded data. TOPUP also required the use of a configuration file, a text file containing some or all of the parameters that can be specified for topup. This file had to be changed to process data acquired on Siemens Prisma, due to an odd matrix of data, differently from data acquired on the GE Premier.
Then, a binary mask is created. This step is crucial for accurately positioning the phantom within the image, particularly focusing on the anisotropic diffusion ring. It involves processing the temporal mean of the topup-corrected NIFTI data, utilizing the capabilities `fslmaths`. The binary mask is designed using a Python function that, given the 3D picture provided by TOPUP as input, iteratively calculates the mean noise value from a subset of the input data, incrementally increasing the kernel size until a valid mean noise value is found. This noise level is used to normalise the original input array, thereby scaling it in relation to noise. The normalised data is then thresholded using the given signal-to-noise ratio (SNR) threshold. Areas in the normalised data below the threshold are assigned to 0 in the mask, indicating areas with a low signal-to-noise ratio, whilst regions above the threshold are put to 1, indicating areas with sufficient signal intensity compared to noise. Using the same reasoning, SNR maps were created for each acquisition.

The following step regards correcting distortions caused by eddy currents. This is done exploiting the EDDY tool in FSL, as described in section 1.6 and using the Pyhton command **eddy**. EDDY is the most time consuming step of the pipeline, taking from 2 to 4 hours to run. In order for EDDY to run, an *acquisition parameters* (specifying information about the acquisition of the DTI data images) and an *index* (text file specifying the relationship between the DTI data images and the information in *acquisition parameters* and in *topup* data) files were necessary. In particular, the *index* was adjusted to accommodate the single shell acquisitions conducted on the Siemens Prisma, as the DTI data acquired consisted of 31 total volumes, in contrast to the 33 volumes provided by the GE Premier. Results of the preprocessing steps are shown in Figure 5.1.

Once the preprocessing steps have been done, the tensor model can be fitted to the diffusion-weighted data to obtain the corresponding measures, i.e. the Fractional Anisotropy (FA) and Mean Diffusivity (MD). This step requires an additional binary mask, a ring mask, that allows us to select only the fibre ring region we're interested in fitting the tensor model's metrics.
At this point, the fitting procedure can be carried out. The tensor model is fitted to the eddy corrected data using the `dtifit` function in Pyhton and Fractional Anisotropy and Mean Diffusivity quantitative maps are obtained. In order to extract from the fibre ring the FA and MD mean and standard deviations values, the features of `fslstats`, provided by `fslpy`, are used. To analyze the phantom data acquired with multiple echo time values, the mean and standard deviations values were also computed on the eigenvalues λ_1, λ_2, λ_3 quantitative maps provided by the `dtifit` function. The outcomes are saved in a .txt file, available for the user to consult.
The 3D representation of the ring mask used for the DTI fits and its placement inside the phantom are shown in Figure 5.2b.
For the multishell acquisitions, in addition to the tensor model, the Bingham-NODDI model and the AMICO-NODDI model are fitted. The Bingham-NODDI model is fitted as described in section 4.2 using the Dmipy Python module. As a first step, a .txt file containing the information of the gradient directions applied during the acquisitions is needed. At this point the mathematical implementation follows: first, the basic Ball, Stick and Zeppelin components are called. Then, the *BinghamDistributed* instead of the

(a) (b) (c)

Figure 5.1: (a) Image of the original diffusion-weighted image of the basic phantom, in which it appears to be warped, notably along the phase encoding gradient direction. (b) The binary mask constructed using the SNR threshold is displayed. (c) The corrected DW-image.

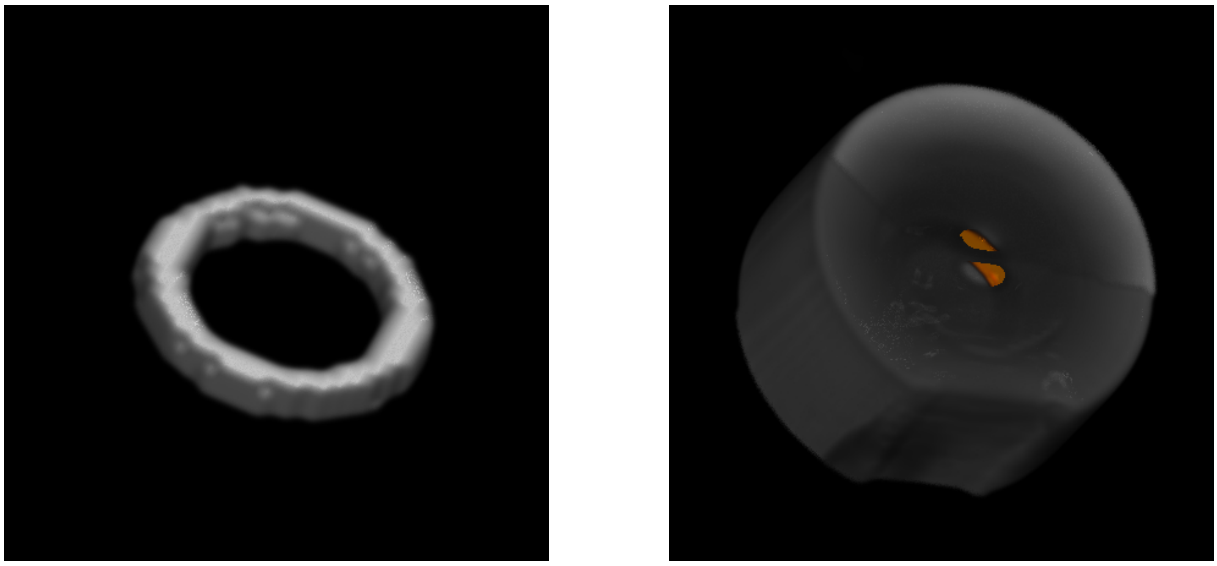

(a) (b)

Figure 5.2: The binary mask has been created for the regions in the phantoms with fibre bundles. The figure shows (a) a ring mask for the basic phantom and (b) 3D representation of the basic phantom, the ring mask, placed inside, is coloured in orange.

WatsonDistributed model is called. The Bingham-NODDI's parametesr assumptions are then set: the tortuosity constraint, equal $\lambda_{\parallel}$ between the Stick and Zeppelin, and fixing the diffusivity to 1.7e-9 m^2/s. The Bingham-dispersed Stick and Ball are then combined in a multi-compartment model, and the isotropic diffusivity of the ball is set to free water diffusivity.

The AMICO-NODDI model is implemented using the publicly accessible GitHub repositorry, as described in section 4.3. The quantitative maps of interest for both models are the tissue volume fraction, intra-neurite volume fraction, and ODI defined in Equation (2.14), to characterise neurite dispersion. These results are extracted using the same ROIs and procedure as the MD and FA values.

For each intrasite acquisition, the Coefficient of Variation (CV) has been computed. This is done to assess consistency and repeatability of the DTI fits. The Coefficient of Variation is a statiscal measure used to describe a datset's relative variability or dispersion in relation to its mean. It is defined as follows:

$$CV = \frac{\text{Standard deviation}}{\text{Mean}} \cdot 100 \tag{5.1}$$

where the standard deviationused is the *Population Standard Deviation*. A lower value of the CV indicates less variability among the obtained metrics results. Viceversa, higher values indicate more variability (hence less repeatability) of results on the same MRI scanner.

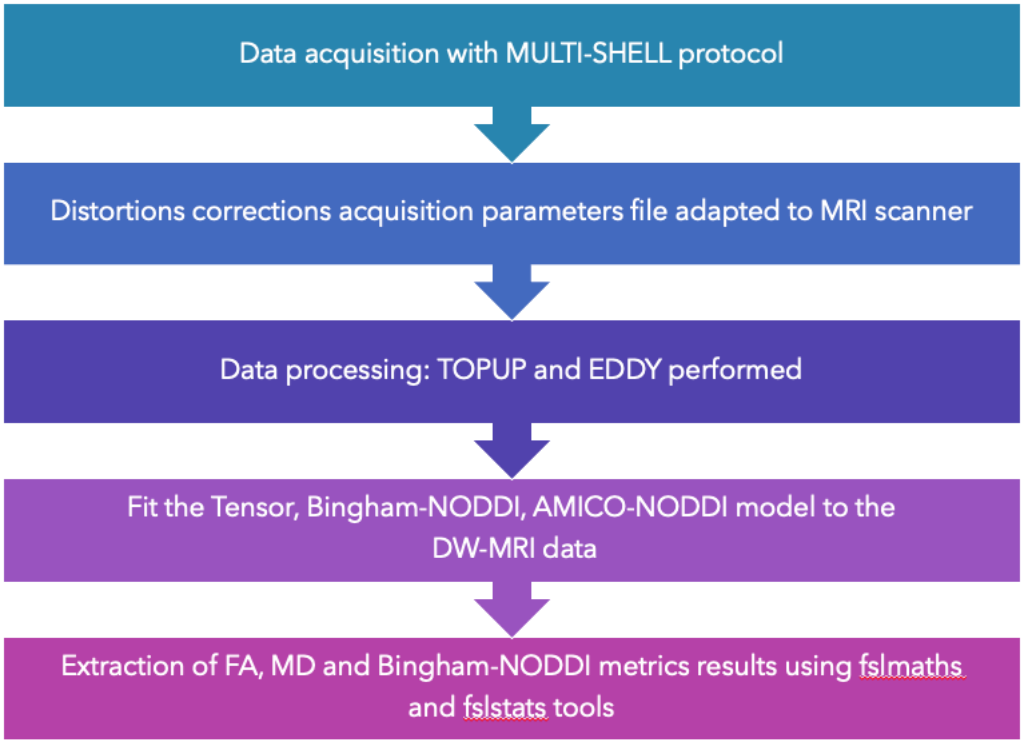

Figure 5.3: Multi-shell acquisition work pipeline.

5.2 In-vivo Brain study

Regarding the *In-vivo* study, four healthy volunteer are scanned on the two 3T MRI scanners: the GE Premier and the Siemens Prisma. The first scan was performed twice on both scanners to assess intra-site consistency before comparing inter-site results. The scanning process involves a structural T1-weighted scan (MP-RAGE) and a diffusion-weighted scan.

The preprocessing steps' pipeline is similar to the one performed for the phantom study. The first step is to correct the B_0 field inhomogeneities and eddy currents-induced distortions, exploiting the features of TOPUP and EDDY implemented in `fslpy`. It is necessary to highlight that brain data acquired on the Siemens Prisma MRI scanner need different configuration and *acquisition parameters* files, since images have been acquired

from Left to Right (differently from GE Premier where the phase encoding direction goes from Anterior to Posterior). The `acqparams` file is, in fact, used to inform EDDY what direction the distortions are likely to go in. Each row consists of a vector (three values) that specifies what the phase-encode (PE) axis is and also what direction along that axis implies higher frequency. So, in the acquisition parameters file written for the data acquired with the Siemens Prisma:

$$1\ 0\ 0\ 0.024 \tag{5.2}$$

$$-1\ 0\ 0\ 0.024 \tag{5.3}$$

have the vectors [1 0 0] and [−1 0 0] both implying that the PE is along the x-direction and which further imply that for the first row [1 0 0] a higher frequency is associated with a position higher up along the x-direction (i.e. positive blips) and the second [1 0 0] implies that a lower frequency is associated with a position higher up (i.e. negative blips). *In-vivo* data requires a binary brain mask for eddy correction, to define the the brain tissue and distinguish it from non-brain structures (e.g., skull, scalp, etc.). The brain mask is created exploiting the features of BET (Brain Extraction Tool) function, implemented in `fslpy`. After images distortions have been corrected, the tensor model and the NODDI models can be fitted to obtain the quantitative maps of each metrics.

In order for results to be extracted, the acquired maps must be registered to a standard space: the MNI152. The MNI152 space is a well known coordinate system in the neuroscience field and it is based on the Montreal Neurological Institute (MNI) reference brain, a template produced by the average of 152 healthy brain scans. It used as a reference when dealing with brain scans performed across different partecipants and studies.
This process of transforming different acquired images into one coordinate system is referred to as *image registration* and it involves the application of translation, rotations, scaling, and shearing trasnformations to make images match. To perform the registration of the acquired images to the MNI152, the first step that must be performed involves the alignement of the non-diffusion weighted B0 image (b-value = 0) with the T1-weighted scan. This is done exploiting the features of FLIRT (FMRIB's Linear Image Registration Tool) tool, implemented in FSL [55]. FLIRT is a fully automated robust and accurate tool for linear (affine) intra- and inter- modal brain image registration. It employs a cost function to assess the similarity of the source and reference images after the transformation. For this study, the cost function that showed the best similarity between the B0 scan and the T1-weighted is the *mutual information* with 6 degrees of freedom (DOF) since images are from the same subject and hence should be registered using 6 DOF (rigid body transformation).

The T1-weighted image must then be registered to the MNI152 space with a nonlinear registration. To perform this operation, first a linear registration of the T1-weighted image to the MNI152 space is done using FLIRT with 12 degrees of freedom, to get the orientation and size of the image close enough for the nonlinear registration, as shown in Figure 5.4a.
Then, using the linear registration matrix generated by executing FLIRT, a nonlinear registration of the original (non-brain-extracted) T1 image to the MNI152 space can be performed (Figure 5.4b). This is done exploiting the features of the FNIRT (FMRIB's Nonlinear Image Registration Tool) [48] FSL tool, a nonlinear image registration tool used when the relation between two pictures (same modality of acquisition) involves compplicated deformations that cannot be correctly represented by linear transformations. The

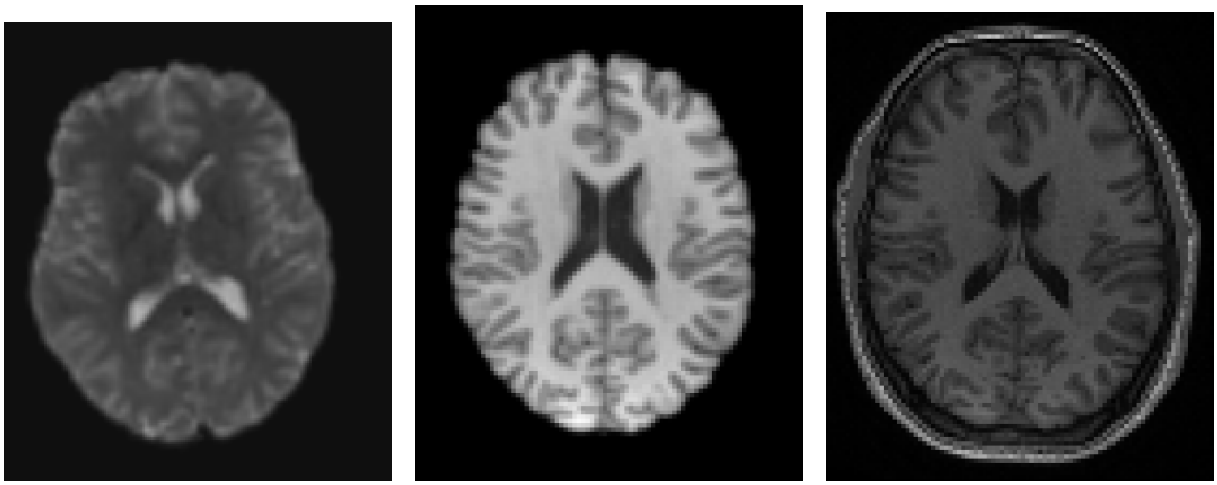

(a) (b) (c)

Figure 5.4: (a) The non-diffusion weighted (T2-weighted) image aligned with the T1-weighted image (rigid body transformation) (b) The T1-weighted image aligned to the MNI152 space (c) The T1-weighted (non-brain extracted) image aligned to the MNI152 space.

FNIRT tool also provides a coefficient file containing the nonlinear spatial transformation used in each voxel to align the T1 to the MNI space, with the intensity value in each voxel representing the amount that this voxel has been shifted by the transformation. In addition to the T1, this *warp* file can be used to register other volumes to the MNI space (Figure 5.4c). By using the FSL's command `applywarp`, the quantitative maps of interest can be aligned to the MNI152 space by applying the transformations contained in the warp file generated by FNIRT.

5.2.1 Regions of Interest (ROIs)

To extract values from the quantitative maps, different Regions of Interest (ROIs) have been created by extracting selected regions from the brain atlases available in FSL. In particular, the ROIs used for this study are shown in Figure 5.5 and they were created in the MNI space.
To extract values of Fractional Anisotropy (FA) and Mean Diffusivity (MD) one ROI for each tissue type was created: Genu and Splenium of Corpus Callosum for White Matter, Thalamus for Gray Matter, and Ventricles for CSF.

Regarding results to be extracted from the NODDI models fit, new ROIs were designed. This is due to the CSF signal being suppressed in the NODDI model's tissue volume fraction. So, in addition to the previous ROIs used to extract results for White and Gray Matter, these new ROIs were created: Caudate and Putamen for Gray Matter, and the anterior and posterior limbs of the Internal Capsule for White Matter, as shown in Figure 5.5. Overall, the Bingham-NODDI model metrics results were extracted from the anterior and posterior limbs of IC and from Genu and Splenium for White Matter and from Thalamus, Caudate and Putamen for Gray Matter.

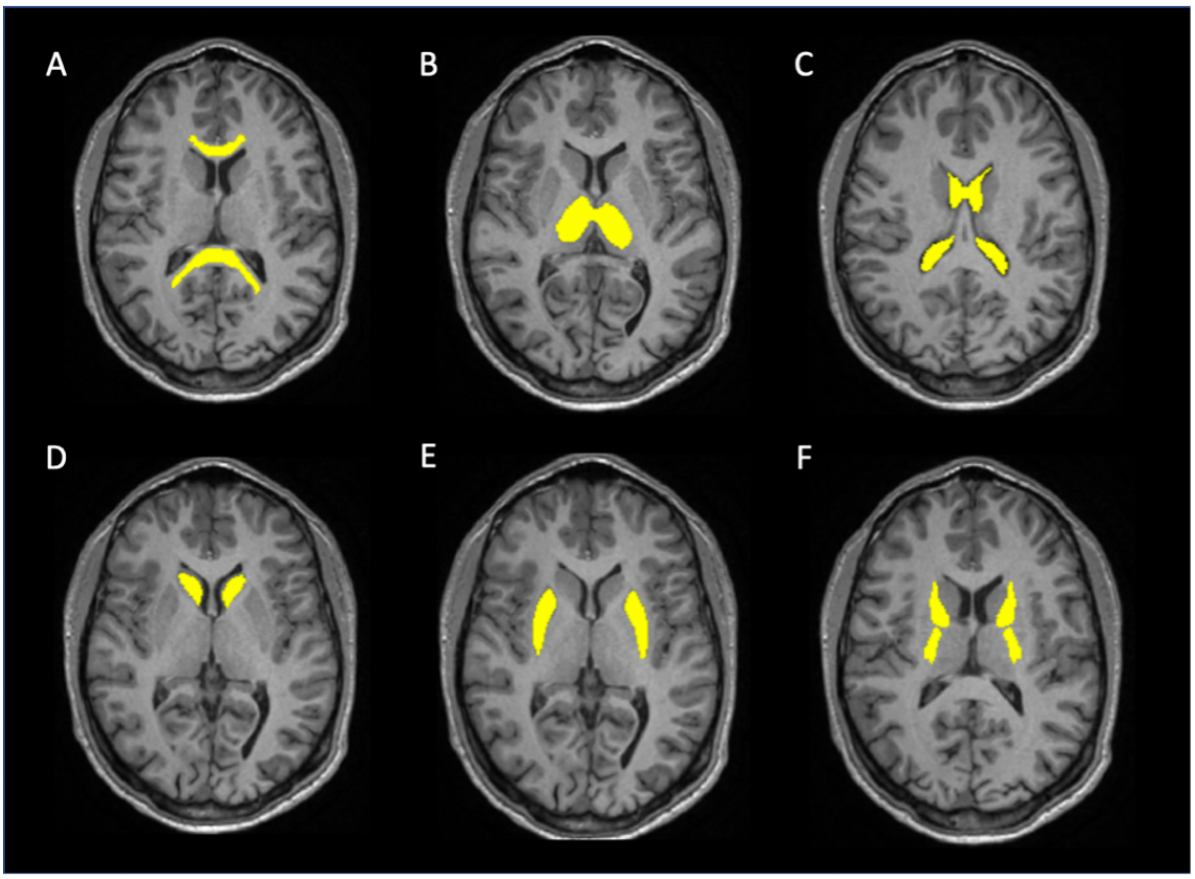

Figure 5.5: ROIs in the brain used to extract the tensor model and the NODDI model metrics results. (A) Genu and Splenium of Corpus Callosum, (B) Thalamus, (D) Ventricles, (E) Caudate, (E) Putamen, (F) Anterior and Posterior limbs of Internal Capsule.

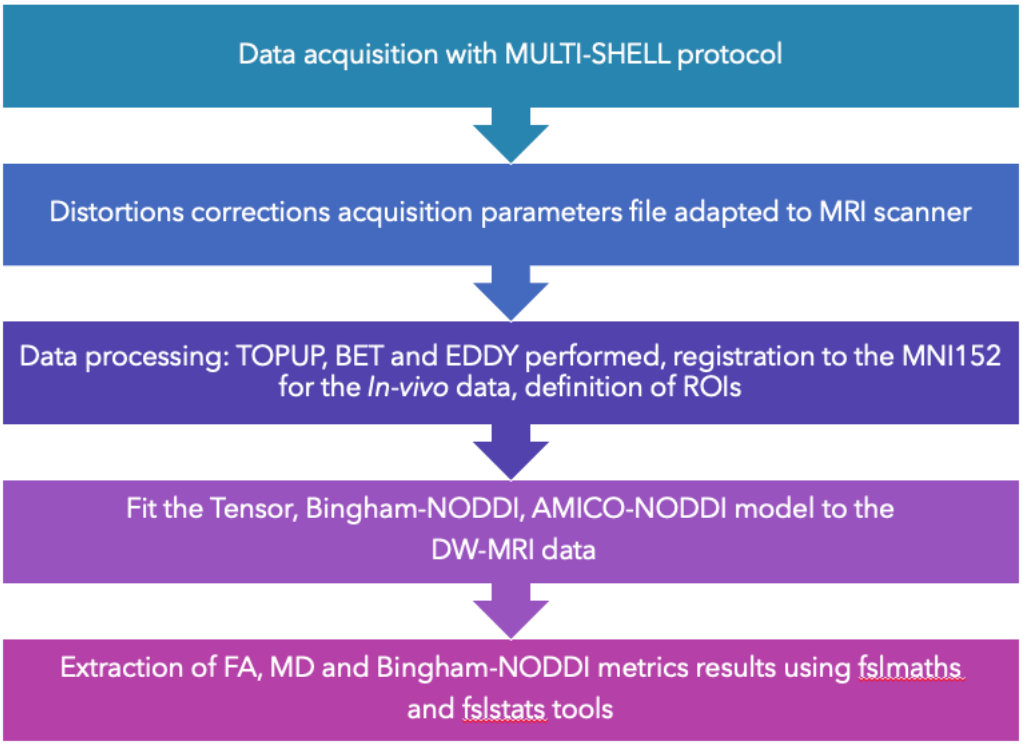

Figure 5.6: *In-vivo* brain data analysis pipeline

Results and Discussion

Chapter 6

PHANTOM STUDY

In this chapter, the results of the phantom data analysis are presented. Diffusion-weighted phantom data was collected as described in section 3.3.
All acquired data was fitted to the DTI tensor model, the Bingham-NODDI and AMICO-NODDI models after the preprocessing steps described in section 5.

The chapter is divided into three sections: the first delves into the results collected from single-shell acquisitions on multiple MRI scanner systems, the second focuses on the results of the analysis of the multi-shell acquisitions on multiple MRI scanner systems, and the third presents results obtained from multiple acquisitions performed with different echo times. In particular, for the first and second section, results are presented singularly for each scan, to assess intra-site repeatability. Furthermore, inter-site comparisons of results are shown, to assess the reliability and consistency of the model on multiple MRI scanner systems.

In all sections, a detailed explanation of the achieved results is presented.

6.1 Single-Shell acquisitions

This analysis seeks to showcase the outcomes of fitting the tensor model to data obtained from single-shell acquisitions across various MRI scanners. The primary goal is to assess and compare the results across different imaging sites. Additionally, we aim to evaluate the effectiveness of single-shell acquisitions in accurately capturing the water diffusion properties of a DTI basic phantom for each scanner, considering the anticipated Fractional Anisotropy (FA) values provided by the manufacturer.

6.1.1 Intra-site results

Two sets of phantom scans were acquired on the Siemens Prisma, and the GE Premier - located at the OCMR - and on the GE Premier and the GE Artist (1.5T) - located at the Churchill Hospital. The phantom used for the acquisition is described in Chapter 3 and illustrated in Figure 3.1a. The acquisitions were performed at the Oxford Centre for Clinical Magnetic Resonance Research (OCMR) - University of Oxford and at the Churchill Hospital - Oxford Hospitals.

As a first step, the original DW images were corrected from distortions, following the procedure described in section 5. The binary masks needed to process the data have different Signal-to-Noise-Rastio according to the specific acquisition. In particular, for

the phantom scans acquired on the Siemens Prisma and on the GE Premier (OCMR) the SNR has been set equal to 150. For the phantom scans acquired on the GE Premier located at Churchill Hospital the SNR has been set equal to 50 whilst it has been set equal to 30 for the phantom scans acquired on the GE Artist.

Figure 6.1 show the postprocessing of images acquired on the Siemens Prisma for the first scan and the second scan.

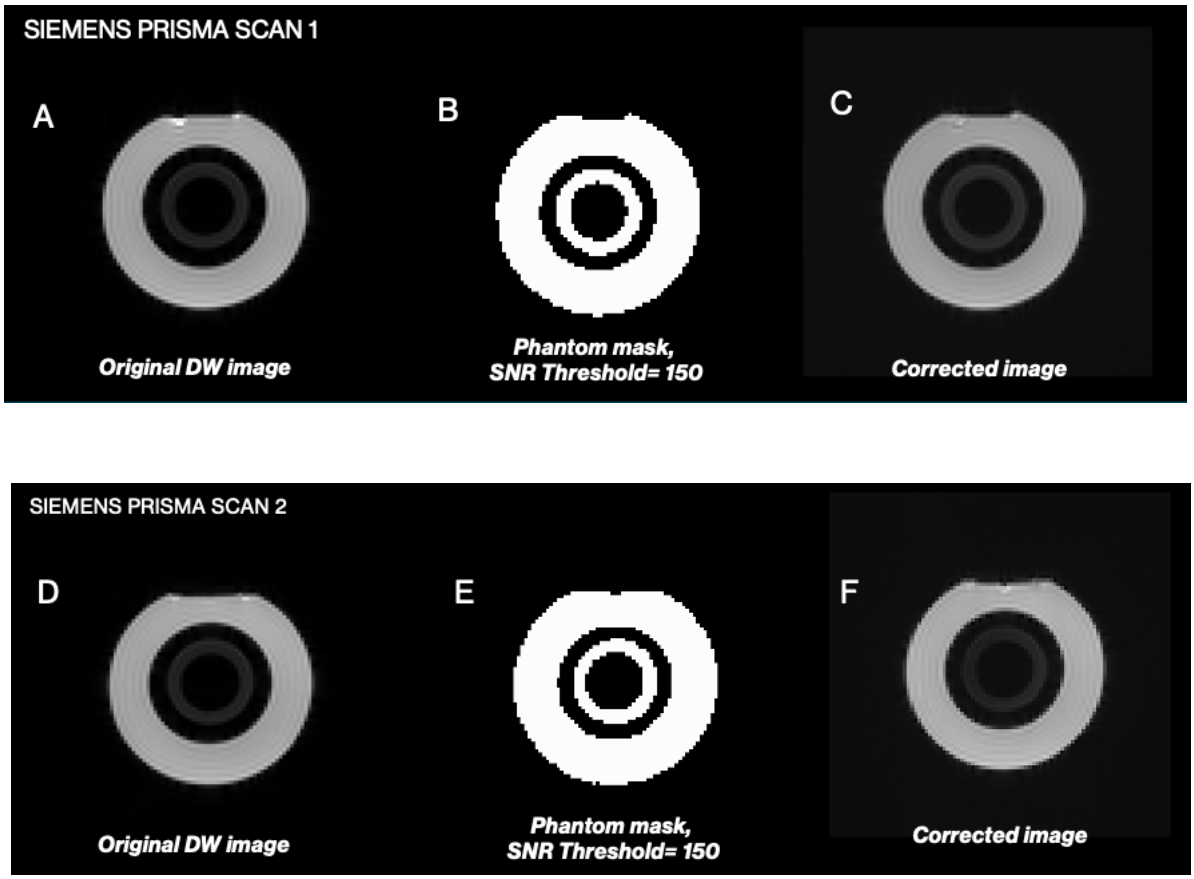

Figure 6.1: Phantom single-shell scan 1 and scan 2 on 3T Siemens Prisma: (A) and (D) Image of the original diffusion-weighted image of the basic phantom, in which it appears to be warped, notably along the phase-encoding gradient direction, (B) and (E) the binary mask constructed using an SNR = 150, as displayed, (C) and (F) The corrected DW-image.

The images visually demonstrate the effectiveness of TOPUP and EDDY in the correction process. The original diffusion-weighted image undergoes distortion along the phase encoding gradient direction, and the corrected output exhibits enhanced visual appeal. The eddy current correction process took approximately 4-5 minutes to complete. This suggests that these images acquired with a single-shell protocol on Siemens Prisma are relatively less impacted by distortions caused by eddy currents compared to other systems. The acquired data was fitted with the Tensor model, extracting the mean and standard deviation values of the Fractional Anisotropy (FA) and Mean Diffusivity (MD) from the fibre ring using a binary mask, as shown in Figure 5.2a. Finally, the Coefficient of Variation (CV) was computed to assess intra-site consistency on each scanner. Metrics results for FA and MD of phantom scans acquired on Siemens Prisma are shown in table 6.1.

Table 6.1: FA and MD results for the basic phantom to look for the consistency of Siemens Prisma single-shell phantom acquisitions.

Tensor model		
	FA	MD ($\cdot 10^{-3}\,\mathrm{mm}^2/\mathrm{s}$)
Scan 1	0.713 ± 0.083	0.957 ± 0.098
Scan 2	0.716 ± 0.078	0.940 ± 0.110
CV	0.22 %	0.90 %

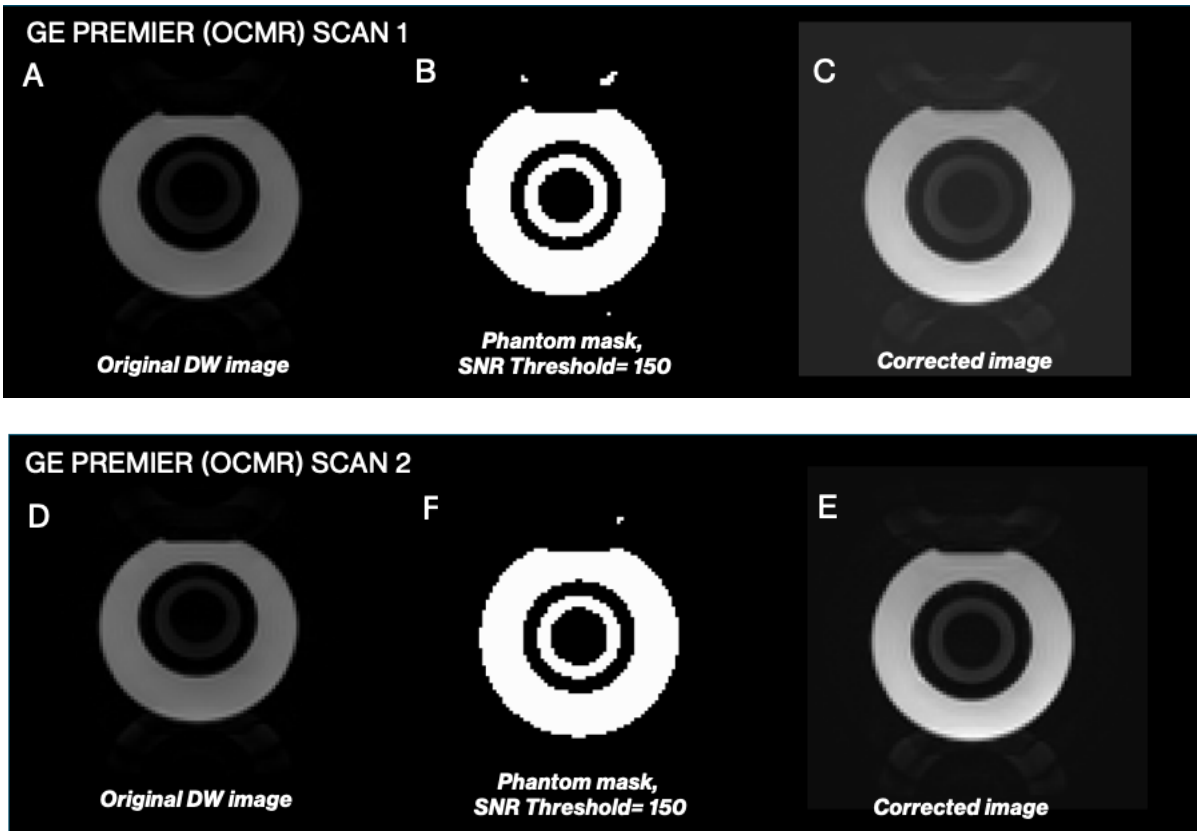

Figure 6.2: Phantom single-shell scan 1 and scan 2 on 3T GE Premier (OCMR): (A) and (D) Image of the original diffusion-weighted image of the basic phantom, in which it appears to be warped, notably along the phase-encoding gradient direction, (B) and (F) the binary mask constructed using an SNR = 150, as displayed, (C) and (E) The corrected DW-image.

The intra-site coefficient of variation low values show how tensor model metrics results obtained fitting data acquired on the Siemens Prisma with a single shell protocol are consistent over time.

Regarding phantom scans acquired on the GE Premier located at the OCMR, results of the correction process are shown in Figure 6.2.
The step of eddy currents-induced distortions correction, differently from the processing of phantom data acquired on the Siemens Prisma, took an average of $\approx$ 2 hours. The tensor model metrics results are presented in table 6.2.
As for the data acquired on the Siemens Prisma, coefficient of variation (CV) values well below 5% indicate there is no notable variation in diffusion tensor metrics intra-site consistency. Regarding phantom data acquired with the GE Premier located at the

Table 6.2: FA and MD results for the basic phantom to look for the consistency of GE Premier (OCMR) single-shell phantom acquisitions.

Tensor model		
	FA	MD ($\cdot 10^{-3}\,\mathrm{mm}^2/\mathrm{s}$)
Scan 1	0.722 ± 0.151	0.901 ± 0.240
Scan 2	0.716 ± 0.079	0.903 ± 0.094
CV	$0.42\,\%$	$0.11\,\%$

Churchill Hospital in Oxford, the original DW images and the post-processing corrected images are shown in Figure 6.3.

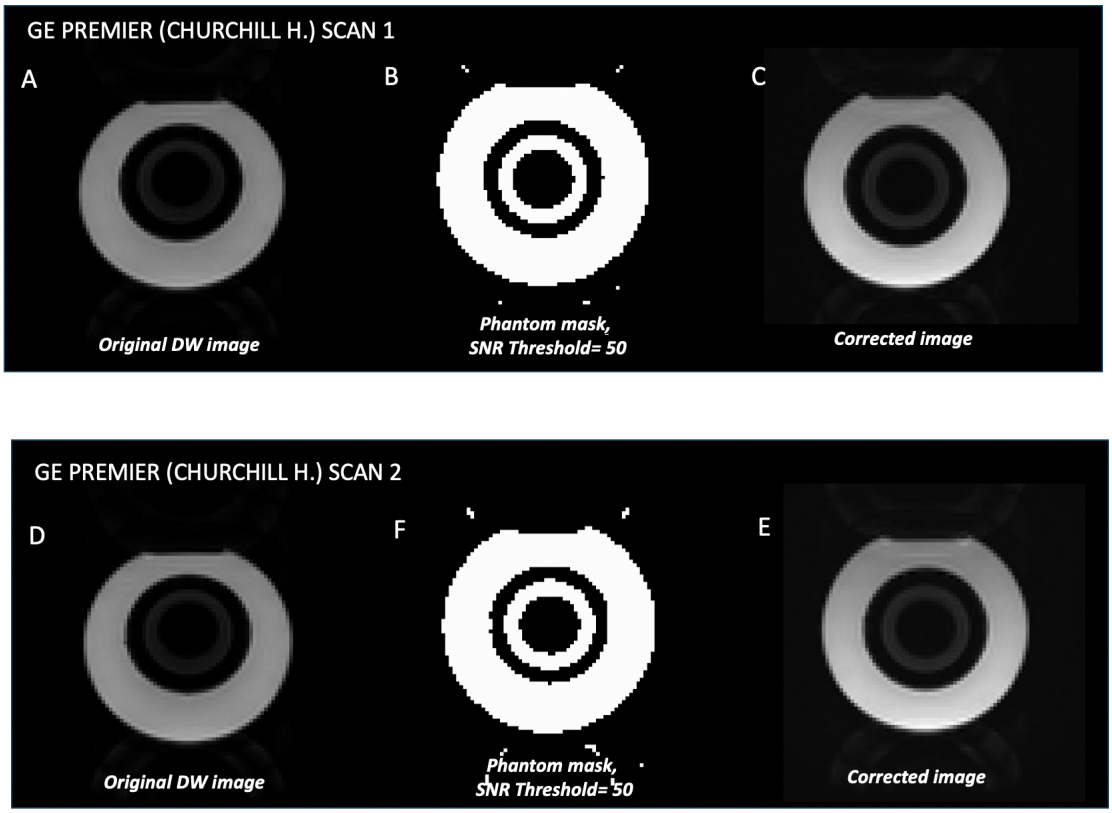

Figure 6.3: Phantom single-shell scan 1 and scan 2 on 3T GE Premier (Churchill Hospital): (A) and (D) Image of the original diffusion-weighted image of the basic phantom, in which it appears to be warped, notably along the phase-encoding gradient direction, (B) and (F) the binary mask constructed using an SNR = 50, as displayed, (C) and (E) The corrected DW-image.

The tensor model metrics results are presented in table 6.3.
Despite the SNR set to create the binary mask is lower compared to single-shell acquisitions on other scanners hence indicating images more affected by noise, the results show intra-site consistency hence ensuring repeatability over time.
Similar considerations can be made for the phantom data acquired on the 1.5T GE Artist, located at the Churchill Hospital, Oxford. In this case, the SNR has been set to 50 in order to get a binary mask able to properly cover the whole fibre ring region. The original DW images, the binary mask, and the post-processed corrected image are shown in Figure 6.4.

Table 6.3: FA and MD results for the basic phantom to look for the consistency of GE Premier (Churchill Hospital) single-shell phantom acquisitions.

Tensor model		
	FA	MD ($\cdot 10^{-3}\,\mathrm{mm}^2/\mathrm{s}$)
Scan 1	0.731 ± 0.085	0.921 ± 0.092
Scan 2	0.738 ± 0.073	0.917 ± 0.080
CV	0.48 %	0.22 %

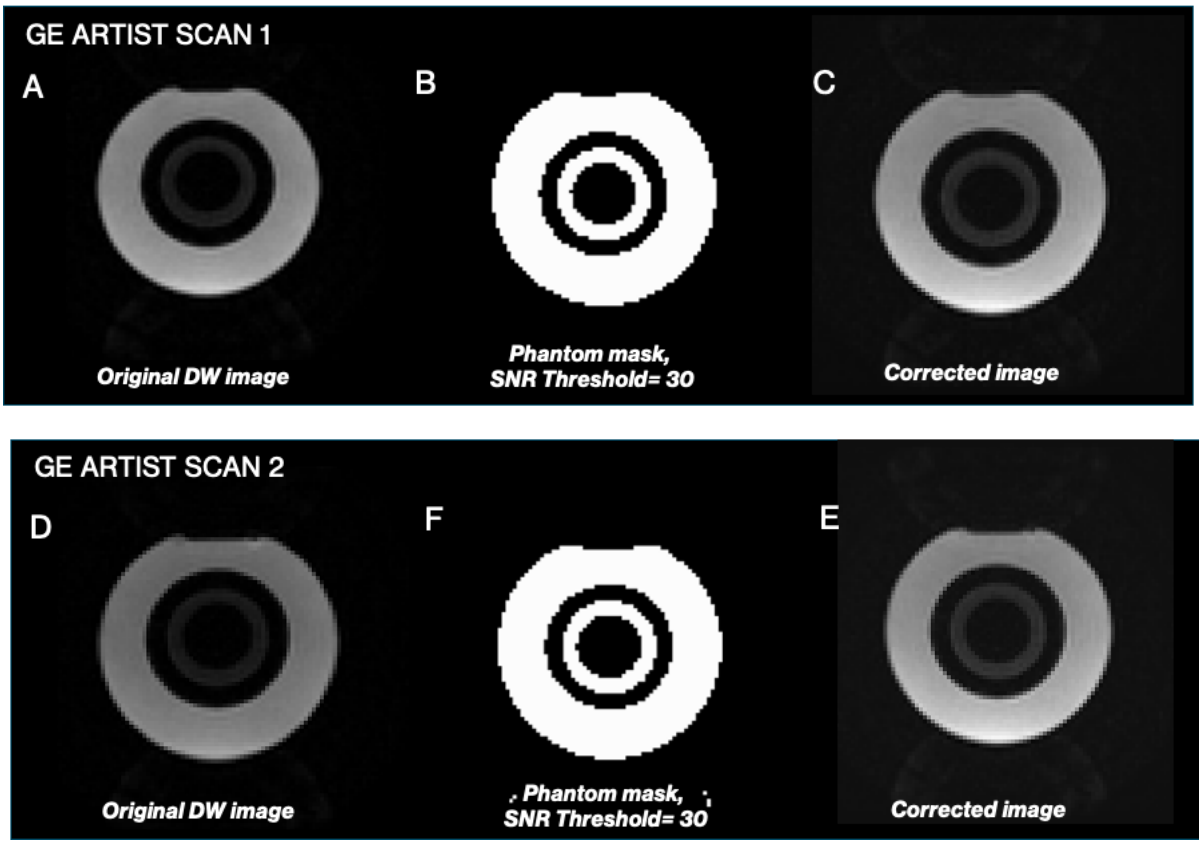

Figure 6.4: Phantom single-shell scan 1 and scan 2 on 1.5T GE Artist (Churchill Hospital): (A) and (D) Image of the original diffusion-weighted image of the basic phantom, in which it appears to be warped, notably along the phase-encoding gradient direction, (B) and (F) the binary mask constructed using an SNR = 50, as displayed, (C) and (E) The corrected DW-image.

The tensor metrics results are shown in Table 6.4. The diminished coefficients of variation (CV) suggest a high degree of result stability, even when utilizing the 1.5T magnetic resonance imaging (MRI) scanner.
For the purpose of facilitating comparisons, a single scan has been selected for each scanner, given the observed consistency in results within the intra-site study. Results are shown in Table 6.5.
Comparisons of fractional anisotropy (FA) and mean diffusivity (MD) outcomes reveal a notable similarity in values obtained through the use of 3T MRI scanners, falling within acceptable margins of error. Nevertheless, it is noteworthy that FA values remain below the manufacturer-specified reference of 0.78 ± 0.02. This discrepancy suggests that the singular use of a single-shell protocol is insufficient to adequately capture the diffu-

Table 6.4: FA and MD results for the basic phantom to look for the consistency of GE Artist (Churchill Hospital) single-shell phantom acquisitions.

Tensor model		
	FA	MD ($\cdot 10^{-3}\,\mathrm{mm}^2/\mathrm{s}$)
Scan 1	0.757 ± 0.099	0.808 ± 0.065
Scan 2	0.759 ± 0.098	0.814 ± 0.109
CV	0.13 %	0.37 %

Table 6.5: Tensor model metrics results comparison for single-shell acquisitions on multiple MRI scanners. FA and MD results of the first scan of each set acquired on: Siemens Prisma, GE Premier (OCMR), GE Premier (Churchill Hospital), GE Artist.

Tensor model				
SS acquisitions	Prisma	Premier(OCMR)	Premier(Church)	Artist
FA	0.713 ± 0.083	0.716 ± 0.079	0.731 ± 0.085	0.757 ± 0.099
MD ($\cdot 10^{-3}\,\mathrm{mm}^2/\mathrm{s}$)	0.957 ± 0.098	0.903 ± 0.094	0.921 ± 0.092	0.808 ± 0.065

sion properties of the fundamental diffusion tensor imaging (DTI) phantom. Moreover, outcomes derived from the GE Artist exhibit elevated fractional anisotropy (FA) values and reduced mean diffusivity (MD) values in contrast to those acquired using alternative MRI scanners. This discrepancy could be attributed to the chosen echo time (TE) for acquisition, particularly noteworthy as the GE Artist employed a prolonged TE of 83.5 ms, compared to the GE Premier (TE = 64.7 ms) and to the Siemens Prisma (TE = 58 ms). A more comprehensive examination of this phenomenon is undertaken in Section 7.1, where acquisitions involve varied echo times to ascertain the extent to which decreasing MD values correlate with increasing TE values.

The basic phantom's FA quantitative maps obtained by fitting the tensor model to the single-shell phantom data acquisitions are shown in Figure 6.5.
The phantom's MD quantitative maps obtained by fitting the tensor model to the single-shell phantom data acquisitions are shown in Figure 6.6.
The GE Premier (OCMR) FA map shows a greater range of values for each voxel of the image. Overall, the maps reveal a consistent pattern wherein both mean diffusivity (MD) and fractional anisotropy (FA) values remain almost constant across the entirety of the fiber ring. This observation signifies a uniform distribution of diffusion properties throughout the specified region.

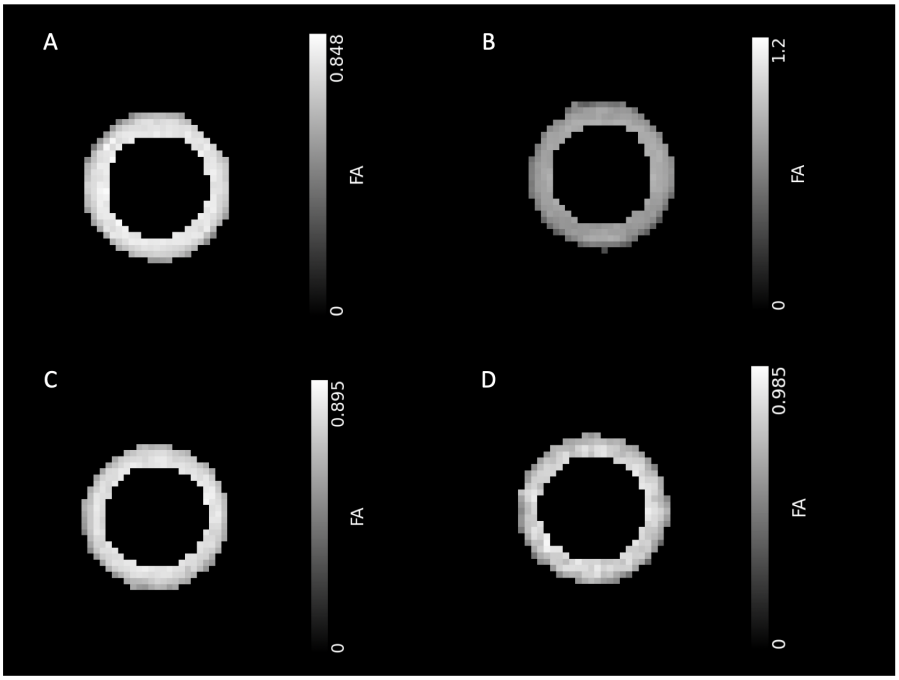

Figure 6.5: FA quantitative maps for single-shell acquisitions of the basic phantom for (A) Siemens Prisma (B) GE Premier (OCMR) (C) GE Premier (Churchill Hospital (D) GE Artist. he images show a uniform distribution of the tensor model parameters along the whole fibre ring.

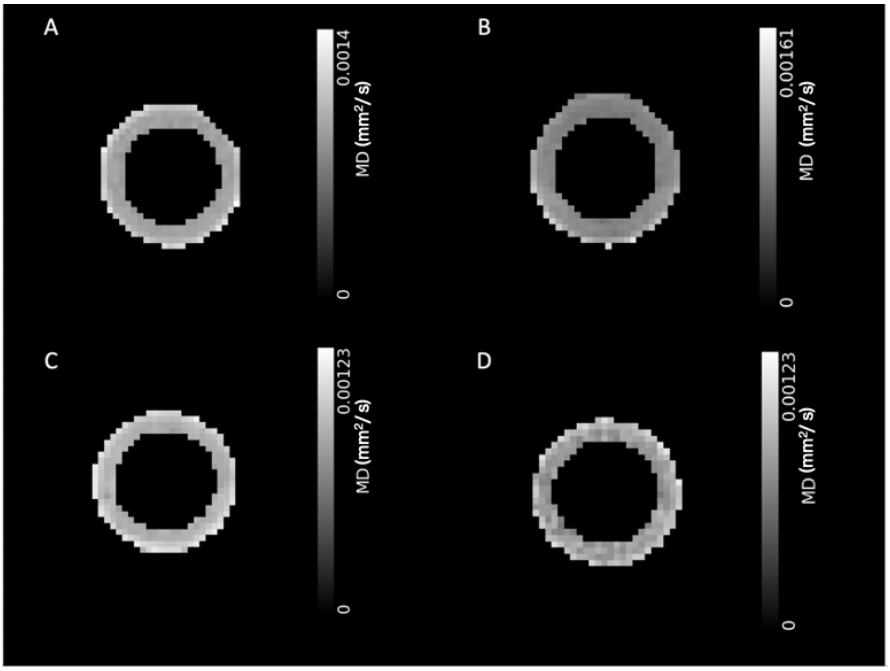

Figure 6.6: MD quantitative maps for single-shell acquisitions of the basic phantom for (A) Siemens Prisma (B) GE Premier (OCMR) (C) GE Premier (Churchill Hospital), (D) GE Artist. The images show a uniform distribution of the tensor model parameters along the whole fibre ring.

6.2 Multi-Shell acquisitions

Though useful, single-shell acquisitions have major limitations, as thoughtfully described in the previous section. Furthermore, multi-shell acquisitions are necessary when dealing with more complex diffusion characteristics. Multi-shell acquisitions involve acquiring data with diffusion gradients applied along multiple shells of directions. This allows for a more comprehensive assessment of tissue microstructure because different shells are sensitive to different ranges of diffusion characteristics. Multi-shell acquisitions are extremely useful, compared to single-shell acquisitions, since they enable the application of more advanced diffusion models, such as multi-compartment models, which can distinguish between different tissue compartments (e.g., intra- and extra-cellular spaces), more accurately, such as the NODDI models. Multi-shell acquisitions are particularly useful for characterizing white matter fiber orientation and crossing fibers, providing a more detailed understanding of complex tissue structures, hence the use of this type of multi-shell acquisitions datasets to fit the Bingham-NODDI model.

As done for the single-shell phantom acquisitions, original DW multi-shell phantom images, and post processed corrected images are shown for each MRI scanner. In particular, as mentioned in section 3.3, multi-shell phantom acquisitions of Siemens Prisma were made using both a spin-echo twice-refocused (Bipolar) and single-refocused applied gradient (Monopolar). Images are shown in Figure 6.7 and Figure 6.8. In both cases, to create the binary mask, an SNR = 150 was set.

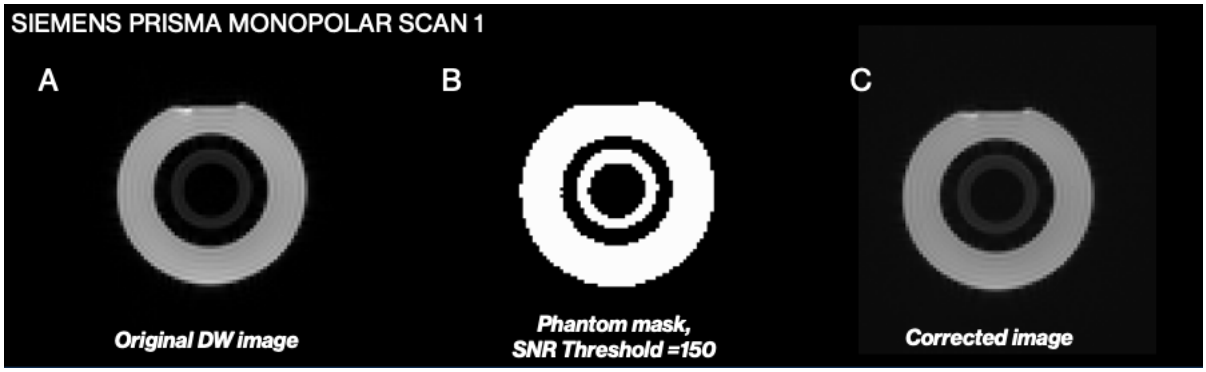

Regarding multi-shell phantom acquisitions on the GE Premier located at the OCMR and those acquired at the Churchill Hospital, images are shown in Figure 6.9 and in Figure 6.10.
Besides minor differences, images show similar features. Regarding multi-shell phantom acquisitions made on the GE Artist 1.5T, original DW-images are more noisy, as it can be seen by the necessity of setting the SNR equal to 10. Images are shown in Figure 6.11. Once the tensor model was fitted to the multi-shell phantom data, the FA and MD values are obtained. For each MRI scanner employed for this study, the tensor model metrics results are shown in Table 6.6. Results show that the Coefficient of Variation (CV) has values below 5%, indicating that multi-shell intra-site phantom acquisitions are consistent over time. Also, multi-shell acquisitions performed on the Siemens Prisma with a single-refocused gradient show a lower CV compared to that corresponding to the acquisitions performed with a twice-refocused gradient.

Regarding the tensor model metrics results obtained fitting to the GE ARtist multi-shell phantom data, FA and MD values are shown in Table 6.7. Results show intra-site stability, as values are similar between scans within the margin of errors. Consistency of the tensor

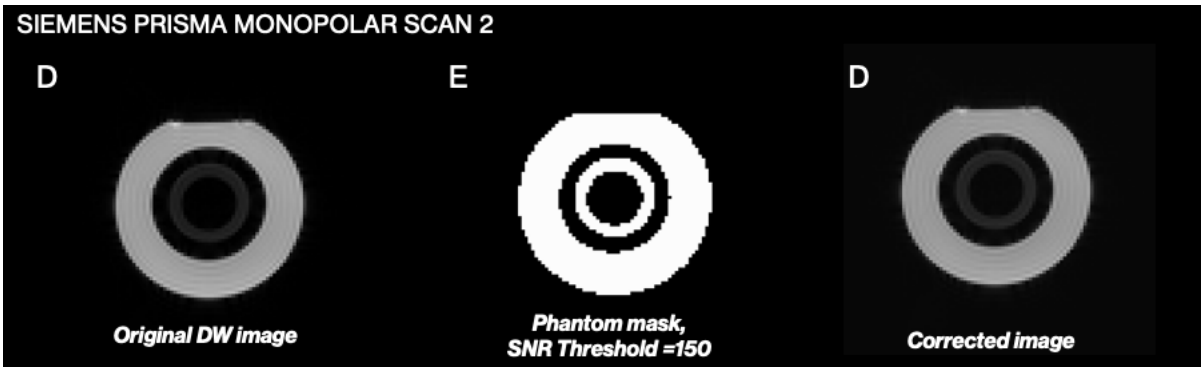

Figure 6.7: Phantom multi-shell Monopolar scan 1 and scan 2 on 3T Siemens Prisma: (A) and (D) Image of the original diffusion-weighted image of the basic phantom, in which it appears to be warped, notably along the phase-encoding gradient direction, (B) and (F) the binary mask constructed using an SNR = 150, as displayed, (C) and (E) The corrected DW-image.

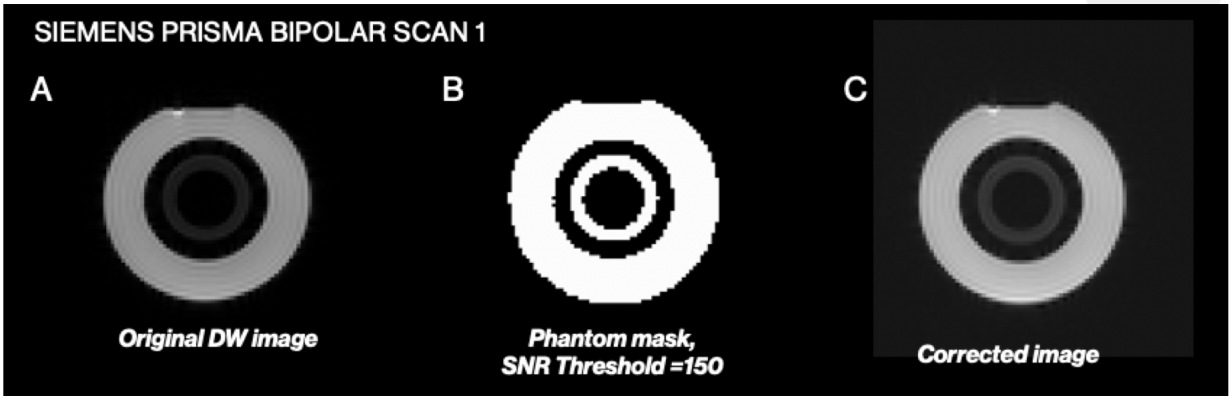

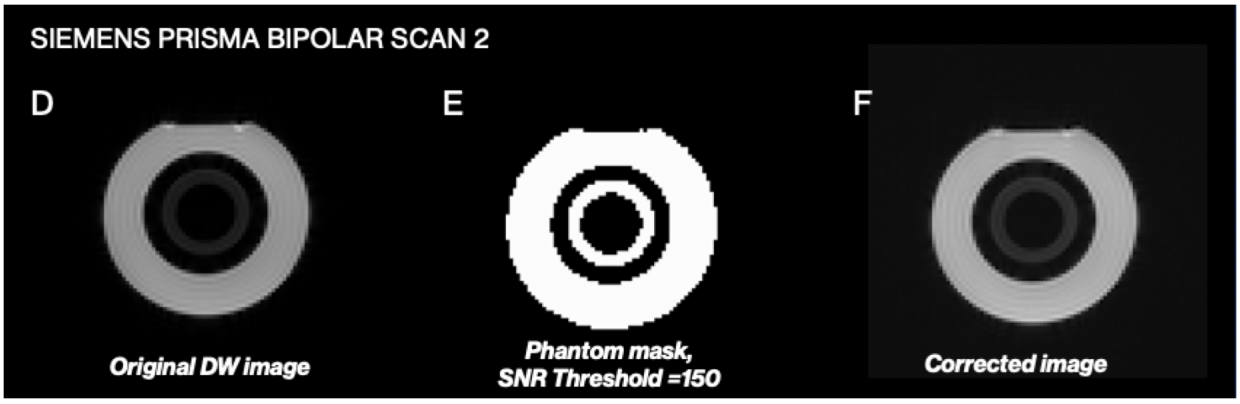

Figure 6.8: Phantom multi-shell Bipolar scan 1 and scan 2 on 3T Siemens Prisma: (A) and (D) Image of the original diffusion-weighted image of the basic phantom, in which it appears to be warped, notably along the phase-encoding gradient direction, (B) and (F) the binary mask constructed using an SNR = 150, as displayed, (C) and (E) The corrected DW-image.

model metrics results is also confirmed by the low values of the Coefficient of Variation (CV), especially the CV related to the Fractional Anisotropy measures.

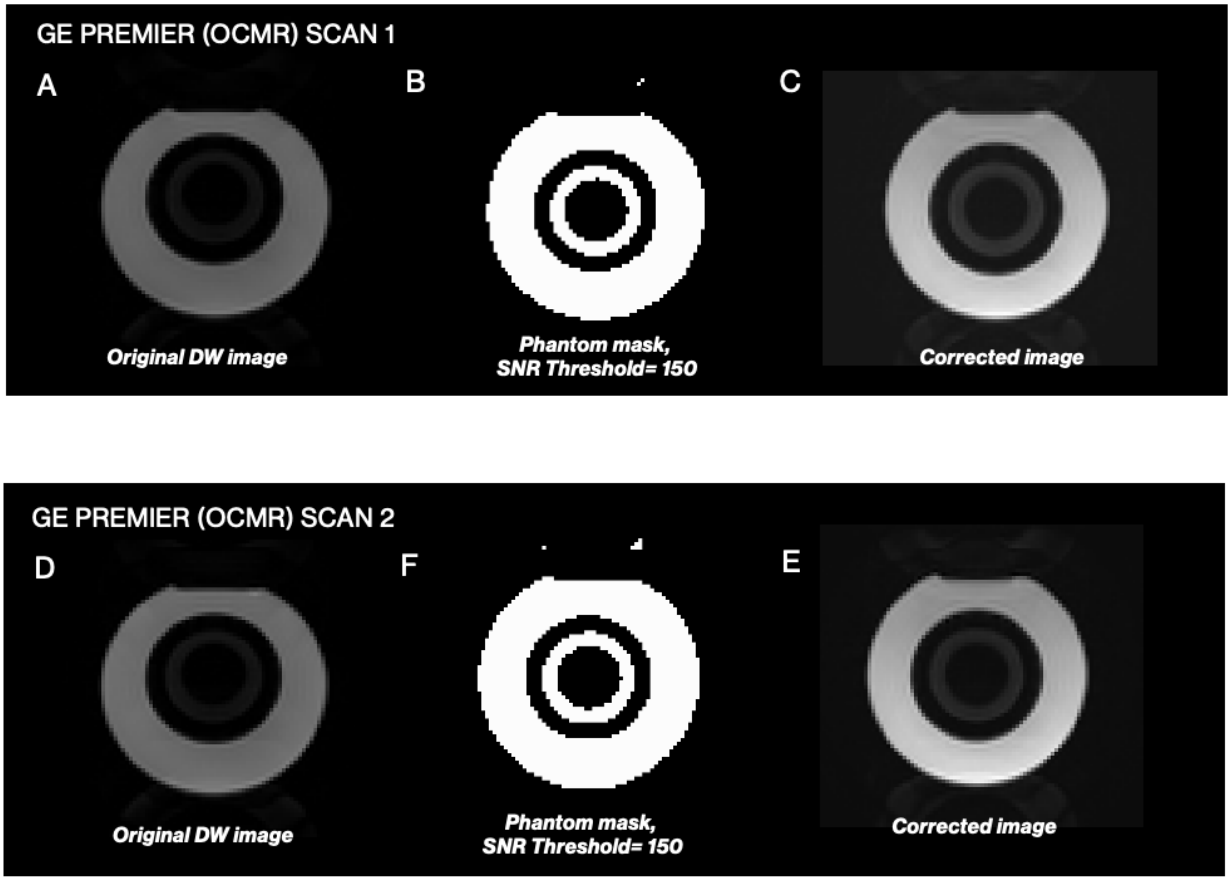

Figure 6.9: Phantom multi-shell scan 1 and scan 2 on 3T GE Premier (OCMR): (A) and (D) Image of the original diffusion-weighted image of the basic phantom, in which it appears to be warped, notably along the phase-encoding gradient direction, (B) and (F) the binary mask constructed using an SNR = 150, as displayed, (C) and (E) The corrected DW-image.

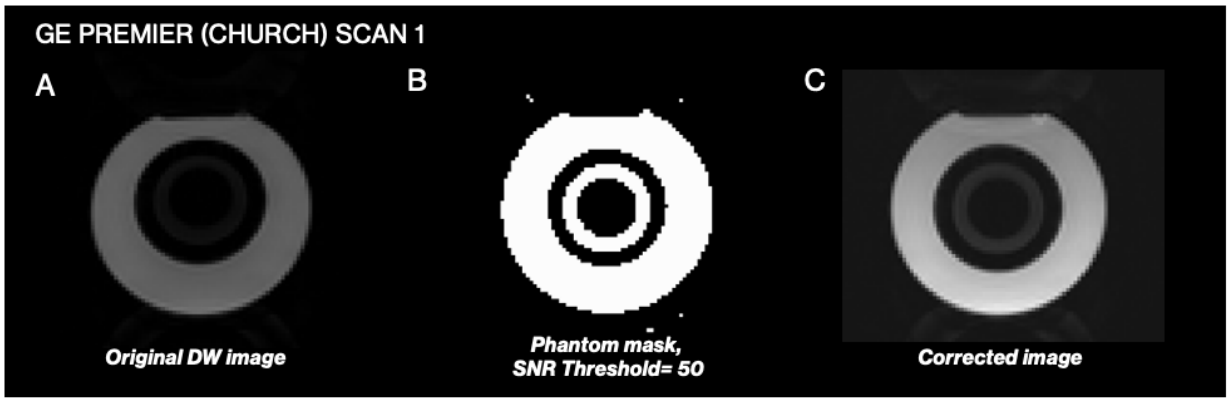

In Table 6.8, the FA and MD values computed fitting the tensor model to multi-shell acquisitions on multiple MRI scanners are shown. In particular, having assessed intra-site consistency (Table 6.6), in order to make comparisons, results of the fit performed to the first scan data of each scanner acquisition were chosen. Comparing the metrics results, it is possible to notice how values are similar within the margin of errors, ensuring inter-site consistency hence the reliability of the tensor model. It's interesting to notice

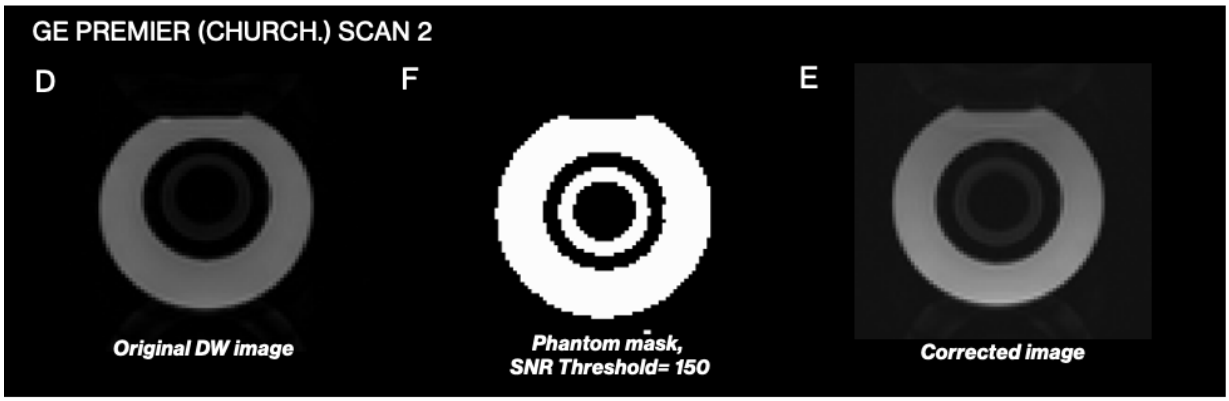

Figure 6.10: Phantom multi-shell scan 1 and scan 2 on 3T GE Premier (Churchill Hospital): (A) and (D) Image of the original diffusion-weighted image of the basic phantom, in which it appears to be warped, notably along the phase-encoding gradient direction, (B) and (F) the binary mask constructed using an SNR = 50, as displayed, (C) and (E) The corrected DW-image.

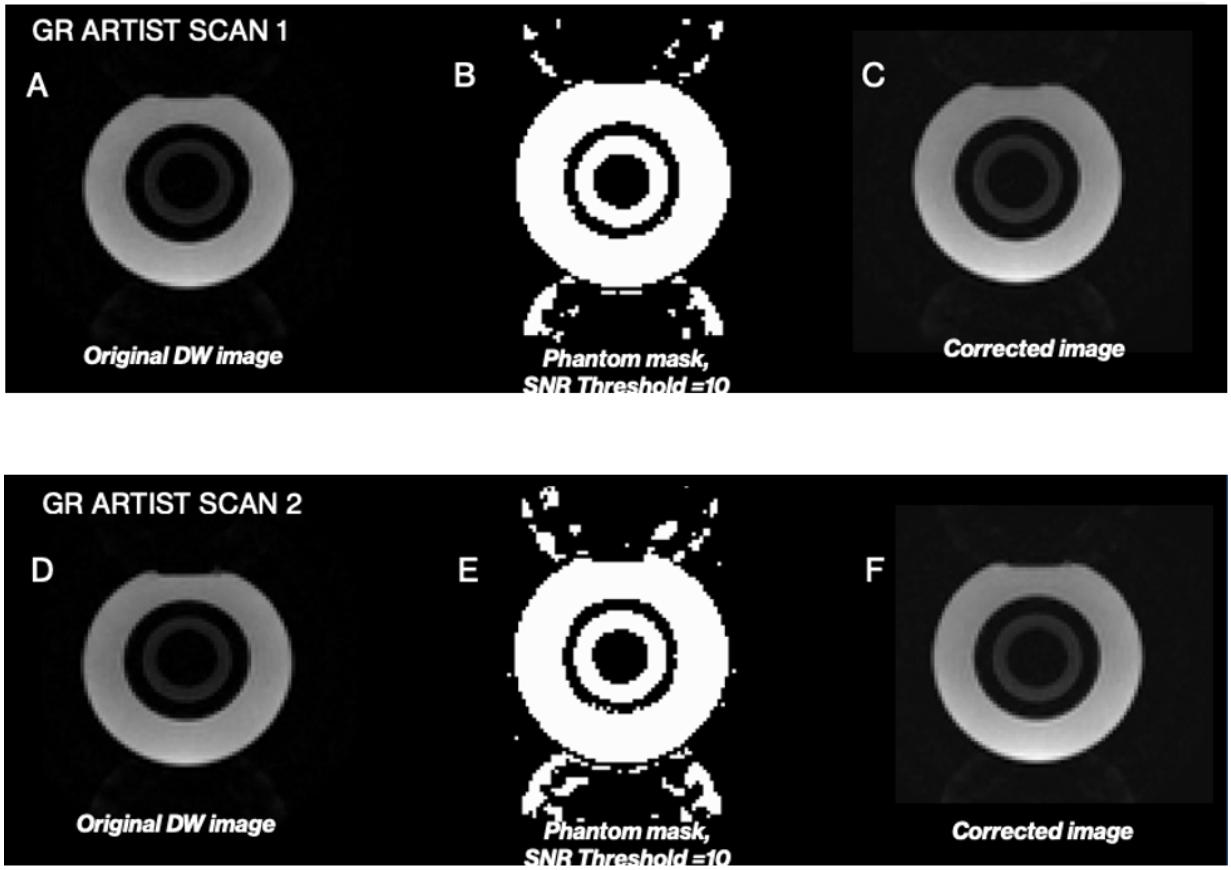

Figure 6.11: Phantom multi-shell scan 1 and scan 2 on 1.5T GE Artist: (A) and (D) Image of the original diffusion-weighted image of the basic phantom, in which it appears to be warped, notably along the phase-encoding gradient direction, (B) and (F) the binary mask constructed using an SNR = 50, as displayed, (C) and (E) The corrected DW-image.

how the Fractional Anisotropy (FA) values obtained fitting to the GE Artist 1.5T scanner multi-shell phantom data are still similar to the value provided by the manufacturer (0.78 $\pm$ 0.02) while the Mean Diffusivity (MD) are lower compared to the results obtained on

Table 6.6: FA and MD results for the basic phantom to look for the consistency of multi-shell protocol acquisitions on the multiple MRI 3T scanners: Siemens Prisma Monopolar and Bipolar, GE Premier (OCMR), GE Premier (Churchill Hospital).

Tensor Model					
		Siemens Prisma MONOPOLAR	Siemens Prisma BIPOLAR	GE Premier (OCMR)	GE Premier (Churchill H.)
FA	SCAN 1	0.7964 ± 0.0561	0.779 ± 0.075	0.7914 ± 0.0584	0.803 ± 0.057
	SCAN 2	0.7954 ± 0.0584	0.785 ± 0.063	0.7912 ± 0.0576	0.801 ± 0.061
	CV (%)	0.06%	0.39%	0.013%	0.09 %
MD ($\cdot 10^{-3}\,\mathbf{mm^2/s}$)	SCAN 1	0.846 ± 0.067	0.861 ± 0.073	0.823 ± 0.065	0.831 ± 0.063
	SCAN 2	0.844 ± 0.070	0.862 ± 0.073	0.824 ± 0.063	0.834 ± 0.069
	CV (%)	0.12 %	0.12 %	0.06%	0.18 %

Table 6.7: FA and MD results for the basic phantom to look for the consistency of Siemens Prisma multi-shell phantom acquisitions on the 1.5T GE Artist.

Tensor model		
	FA	MD ($\cdot 10^{-3}\,\mathrm{mm^2/s}$)
Scan 1	0.794 ± 0.072	0.661 ± 0.059
Scan 2	0.793 ± 0.078	0.677 ± 0.065
CV	0.08 %	1.2 %

the other scanners, as also seen for the single shell acquisition. One reason may be due to the increased echo time necessary to be set for these acquisitions (TE = 105 ms) compared to echo times set to acquire multi-shell phantom data on the other MRI scanners.

Table 6.8: Multi-shell acquisitions metrics results. The first scan of each acquisition has been chosen to compare FA and MD results of phantom data acquired on the Siemens Prisma Monopolar and Bipolar, GE Premier (OCMR), GE Premieri (Churchill Hospital) and GE Artist.

Tensor Model					
	Siemens Prisma MONOPOLAR	Siemens Prisma BIPOLAR	GE Premier (OCMR)	GE Premier (Churchill H.)	GE Artist
	TE = 69 ms	TE = 81 ms	TE = 76.9 ms	TE = 72.1 ms	TE = 105 ms
FA	0.796 ± 0.056	0.779 ± 0.0785	0.791 ± 0.058	0.803 ± 0.057	0.794 ± 0.072
MD ($\cdot 10^{-3}\,\mathbf{mm^2/s}$)	0.846 ± 0.067	0.861 ± 0.073	0.823 ± 0.065	0.831 ± 0.063	0.661 ± 0.059

The quantitative maps of FA and MD of each scanner are compared in Figure 6.13 and in Figure 6.12.
The FA and MD maps show how values remain constant throughout the entire fibre ring, indicating a uniform distribution of the diffusion properties. All ring masks were created using the tools provided by FSLeyes. To assess the impact of manual mask variations on data acquired from the GE Artist, multiple masks were generated. The objective was to investigate whether lower mean diffusivity (MD) values were associated with fluctuations in manual mask creation. Subsequently, all masks underwent application in the `dtifit` process, yielding consistent outcomes. Notably, an observed correlation emerged: augmenting the dimensions of the outer 3D layer of the ring mask resulted in a reduction of fractional anisotropy (FA) values and an increase in MD. However, it is imperative to acknowledge that expanding the ring mask's dimensions would concurrently elevate noise

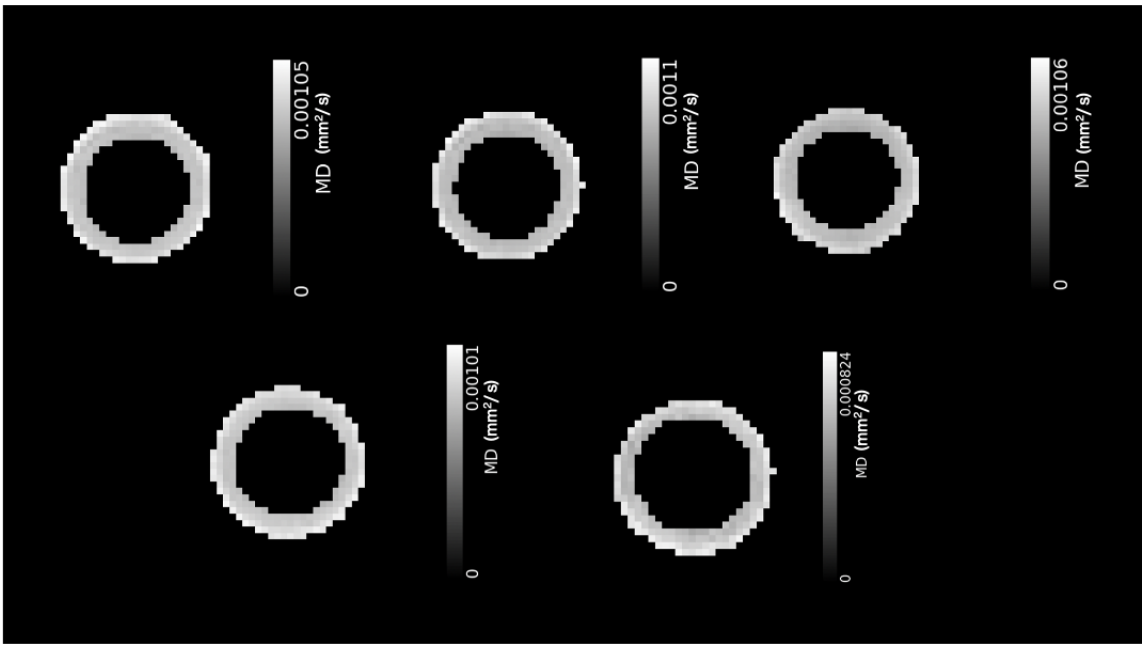

Figure 6.12: Mean Diffusivity quantitive maps for the multi-shell acquisitions performed on, in order, first row: Siemens Prisma Monopolar and Bipolar, GE Premier (OCMR); second row: GE Premier (Churchill Hospital) and GE Artist.

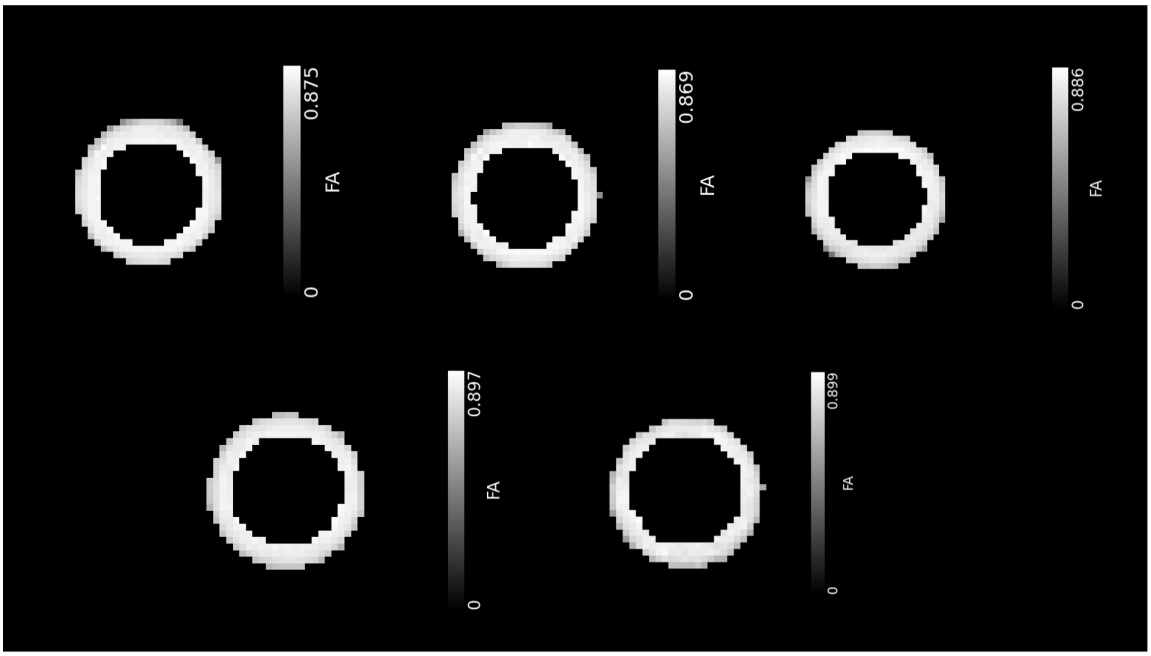

Figure 6.13: Fractional Anisotropy quantitive maps for the multi-shell acquisitions performed on, in order, first row: Siemens Prisma Monopolar and Bipolar, GE Premier (OCMR); second row: GE Premier (Churchill Hospital) and GE Artist.

levels. This occurs as additional pixels, associated with lower FA values, influence the final average FA value, thereby introducing inaccuracies and subsequently higher standard deviations in the results.

In Table 6.9 the results of the Bingham-NODDI metrics for the acquisitions performed

on the Siemens Prisma with a single-refocused applied gradient are shown. In Figure 6.14, all the quantitative maps given as output from the Bingham-NODDI fit are also displayed, showing a uniform distribution of the parameter of interest within the selected region, i.e. the fibre ring, except for the β-fraction. Within the spectrum of considered parameters, the characterization of the neurite orientation's dispersion or spread relative to the dominant neurite direction is encapsulated by the orientation dispersion index (ODI). High ODI values signify a complex and disorganized configuration of neurites within a voxel. Conversely, low ODI values indicate a more condensed and organized structure of neuronal fibers, reflecting a relatively uniform alignment of neurites. This alignment pattern aligns with the anticipated configuration outlined by the phantom manufacturing specifications. Intra-site results for the Siemens Prisma Monopolar acquisition show a CV of 0.13 %, indicating intra-site consistent repeatability of results over time.

The β-fraction parameter is linked with the concentration of neurites within a voxel. In particular, it measures the proportion of volume of a voxel that is occupied by neurites (i.e., axons and dendrites) in relation to the total volume. The higher the value, the higher the concentration of neurites within a voxel. When the β-fraction is close to 1, it suggests a significant presence of neurites within the voxel under consideration. Higher β-fraction values imply a greater concentration of neurite orientations around a dominant direction, indicating a more organized and coherent fiber structure. Lower β-fraction values suggest a more dispersed or isotropic arrangement of neurites, indicating a less organized structure. In the case of the Monopolar acquisitions performed on the Siemens Prisma, the β-fraction values indicate there's a greater concentration of neurites in voxels of the fibre ring region compared to the rest of the phantom, as also displayed by the β-fraction quantitative map in Figure 6.14(B). The CV of 4.06 % is still below the desired threshold of the 5%.

Other important parameters to discuss are the tissue volume fraction and the intra-cellular volume fraction. The tissue volume fraction measures the amount of brain tissue occupying the volume of a voxel, complementarily to the non-tissue volume fraction, measuring the portion of the voxel occupied by the Cerebral Spinal Fluid (CSF) or other non-tissue components. The values of tissue volume fraction are close to 1, as also shown in the quantitative map in Figure 6.14(C), as the fibre ring region should mimic the brain tissue hence excluding the CSF. The results obtained show a low CV equal to 0.02%, confirming intra-site consistency.

The intra-cellular volume fraction refers to the portion of the volume of a voxel that is occupied by neurites, specifically axons and dendrites. In the case of the Monopolar acquisitions performed on the Siemens Prisma, the intra-cellular volume fraction is consistent over time, with a CV equal to 0.11%, as also shown in Figure 6.14(D).

To evaluate the goodness of the fit, the Mean Square Error (MSE) and the R^2 coefficient are used. The Mean Square Error obtained values are low, indicating that the model fits properly the data. The MSE quantitative map is also shown in Figure 6.14(F). The R^2 coefficient, also known as the coefficient of determination, is a statistical measure of how well the observed values of a dependent variable (or response variable) are predicted by a model. It is a value between 0 and 1, where R^2 =0 indicates that the model does not explain any of the variability in the dependent variable. Viceversa, R^2 = 1 indicates that the model perfectly explains the variability in the dependent variable. R^2 is used to determine the goodness of the fit, where higher values indicate a better fit. In the case of the Monopolar acquisitions performed on the Siemens Prisma, the R^2 is very close to 1,

as also shown in Figure 6.14(E). The quite high CV for the MSE can be due to the very low values of the MSE itself, in some cases also equal to its standard deviation.

Table 6.9: Bingham-NODDI model metrics results for a set of two acquisitions of phantom data performed on the 3T Siemens Prisma with a single-refocused applied gradient (monopolar acquisition).

Bingham-NODDI model						
	ODI	**β-fraction**	**Tissue v.f.**	**Intra-neurite v.f.**	**R^2**	**MSE**
SCAN 1	0.0202 ± 0.0012	0.4096 ± 0.2562	0.969 ± 0.041	0.426 ± 0.069	0.988 ± 0.004	0.0009 ± 0.0003
SCAN 2	0.0201 ± 0.0007	0.3777 ± 0.2776	0.968 ± 0.042	0.427 ± 0.070	0.988 ± 0.003	0.0010 ± 0.0003
CV (%)	0.13%	4.06%	0.02%	0.11%	0.004%	0.52%

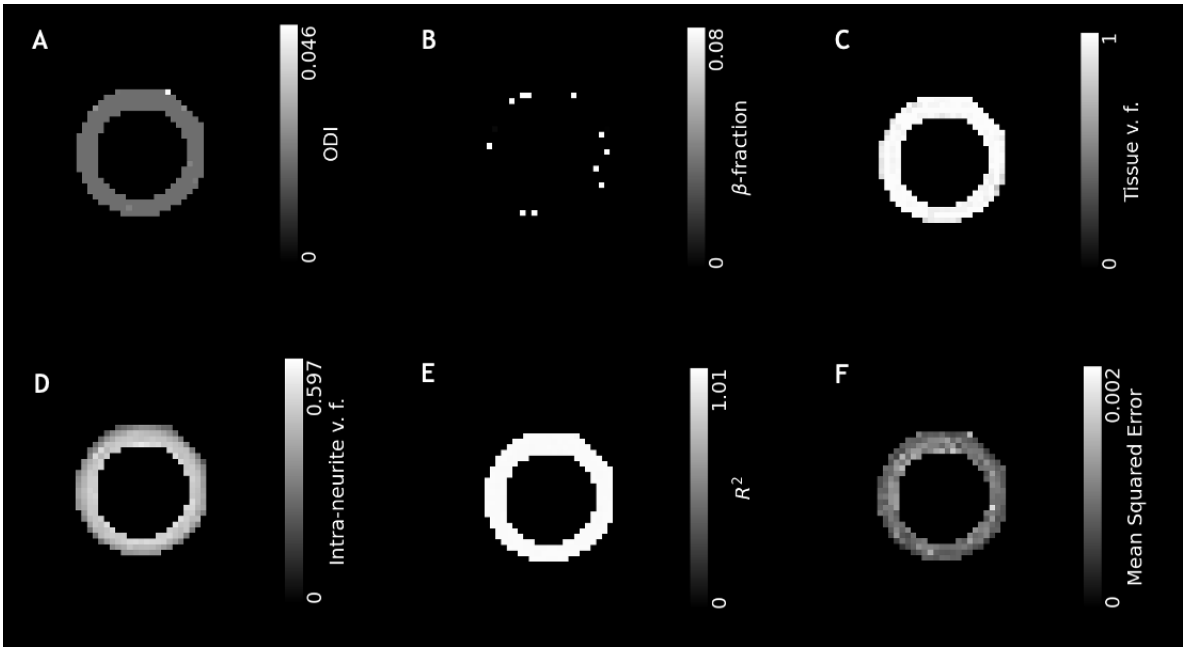

Figure 6.14: Quantitative maps of the parameters given as output by the Bingham-NODDI model fitted to the phantom data acquired on the Siemens Prisma with a single-refocused applied gradient (Monopolar). The images represent (A) the ODI, (B) the β-fraction, (C) the Tissue volume fraction, (D) the Intra-cellular volume fraction, (D) the R^2 coefficient, (E) the MSE coefficient.

Regarding phantom Bipolar acquisitions performed on the Siemens Prisma, the Bingham-NODDI fit metrics results are shown in Table 6.10. The quantitative maps for each Bingham-NODDI parameter are shown in Figure 6.15. The ODI values show consistency over time, with a CV equal to 1.2%. Similar considerations can be made for the intra-cellular and tissue volume fractions, as they show low values for the coefficient of variation. The β-fraction CV is equal to 5%, exactly equal to our desired threshold. This value could be due to the non-uniform distribution of the β-fraction values in the fibre ring, resulting in a higher standard deviation of the measurements. The R^2 coefficient values are close to 1 and the MSE low values suggest satisfactory goodness of fit.
Comparing the intra-site consistency of the acquisitions performed on the Siemens Prisma using a single-refocused and a twice-refocused applied gradient, it is possible to notice that the ODI values are consistent in both protocols' results however, the coefficient of variation (CV) for the Bipolar β-fraction is comparatively higher in the Monopolar acquisition.

This may reflect the impact of acquisition parameters in capturing the properties of distributions of neurite orientations.
Notably, both the tissue volume fraction and intra-cellular volume fraction demonstrate temporal repeatability in the outcomes for both protocols. Furthermore, the R^2 coefficient and Mean Squared Error (MSE) exhibit low CV values for both protocols, with the Monopolar acquisitions displaying a lower MSE compared to the Bipolar counterparts.

Table 6.10: Bingham-NODDI model metrics results for a set of two acquisitions of phantom data performed on the 3T Siemens Prisma with a twice-refocused applied gradient (bipolar acquisition).

Bingham-NODDI model						
	ODI	**β-fraction**	**Tissue v.f.**	**Intra-neurite v.f.**	**R^2**	**MSE**
SCAN 1	0.0206 ± 0.0085	0.4723 ± 0.2351	0.958 ± 0.052	0.410 ± 0.077	0.987 ± 0.004	0.0010 ± 0.0004
SCAN 2	0.0202 ± 0.0091	0.4274 ± 0.2269	0.959 ± 0.048	0.413 ± 0.073	0.988 ± 0.003	0.0010 ± 0.0003
CV (%)	1.2%	5%	0.05%	0.36%	0.02%	1.63%

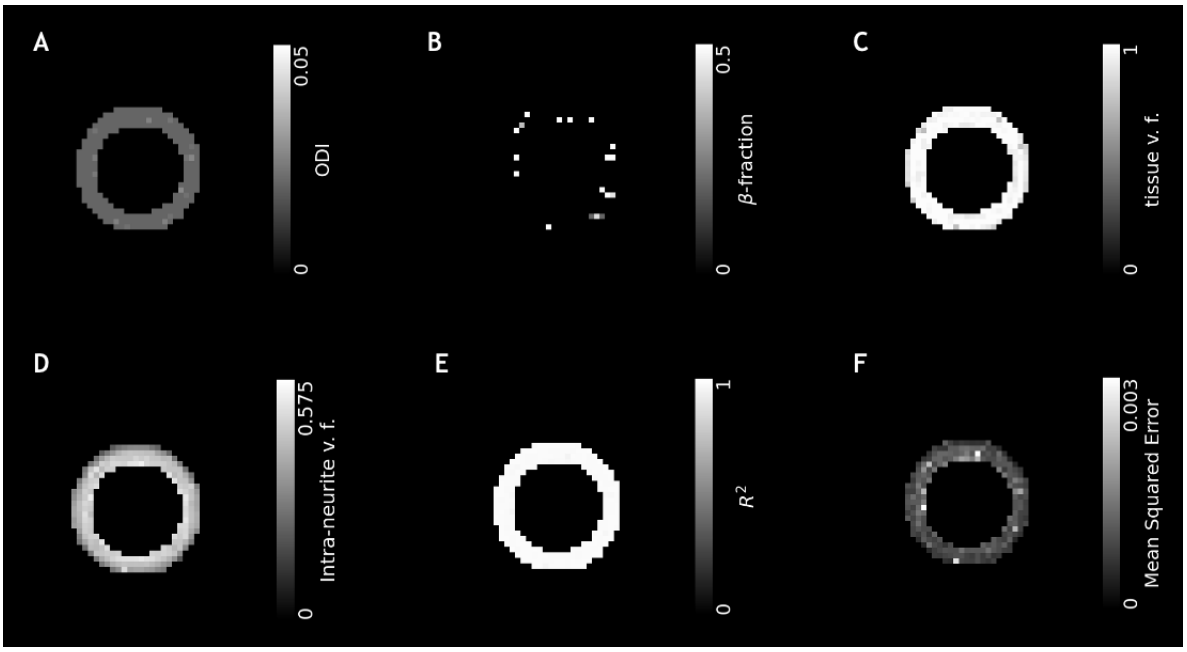

Figure 6.15: Quantitative maps of the parameters given as output by the Bingham-NODDI model fir on the phantom data acquired on the Siemens Prisma with a twice-refocused applied gradient (bipolar). The images represent (A) the ODI, (B) the β-fraction, (C) the Tissue volume fraction, (D) the Intra-cellular volume fraction, (D) the R^2 coefficient, (E) the MSE coefficient.

Regarding the other two 3T MRI scanners, i.e., the GE Premier located at the Oxford Centre for Magnetic Resonance Research (OCMR) and at the Churchill Hospital, results are shown below. In particular, the Bingham-NODDI metrics obtained fitting the phantom data acquired on the GE Premier located at the OCMR are shown in Table 6.11. The quantitative maps for the Bingham-NODDI parameters are shown in Figure 6.16. The ODI values show consistency over time, with a CV equal to 0.22%. Similar considerations can be made for the intra-cellular and tissue volume fractions, as they show low values for the coefficient of variation. The β-fraction CV is equal to 2.28%, below our desired

Table 6.11: Bingham-NODDI model metrics results for a set of two acquisitions of phantom data performed on the 3T GE Premier located at the OCMR.

Bingham-NODDI model						
	ODI	**β-fraction**	**Tissue v.f.**	**Intra-neurite v.f.**	R^2	**MSE**
SCAN 1	0.0203 ± 0.0015	0.327 ± 0.261	0.969 ± 0.045	0.431 ± 0.069	0.986 ± 0.005	0.0011 ± 0.0004
SCAN 2	0.0202 ± 0.0011	0.312 ± 0.255	0.974 ± 0.042	0.431 ± 0.069	0.987 ± 0.004	0.0010 ± 0.0003
CV (%)	0.22%	2.28%	0.24%	0.02%	0.05%	3.57%

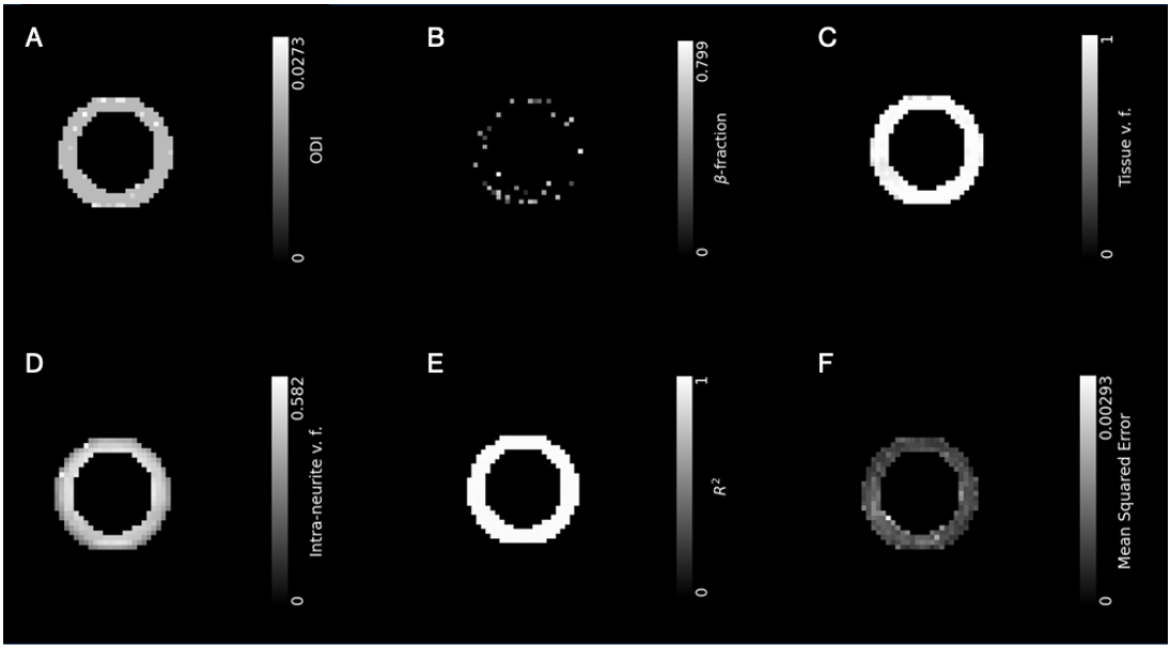

Figure 6.16: Quantitative maps of the parameters given as output by the Bingham-NODDI model fir on the phantom data acquired on the GE Premier located at the OCMR. The images represent (A) the ODI, (B) the β-fraction, (C) the Tissue volume fraction, (D) the Intra-cellular volume fraction, (D) the R^2 coefficient, (E) the MSE coefficient.

threshold. The R^2 coefficient values are close to 1 and the MSE low values suggest a satisfactory goodness of fit.

Results obtained by fitting phantom data acquired on the GE Premier located at the Churchill Hospital are shown in Table 6.12. Quantitative maps for the Bingham-NODDI model parameters are displayed in Figure 6.17. Outcomes highlight low ODI values, indicating that in the fibre ring region the orientation dispersion of neurites is low hence suggesting a fairly organized structure for neurites. This is consistent with the information supplied by the phantom's manufacturing specifications and in alignment with the inherent nature of the fiber ring region, which emulates brain tissue within a relatively compact structure. The CV value is equal to 0.99% suggesting intra-site stability of results. Similar considerations about the CV can be made for the other parameters. As in the case of the Bipolar acquisitions performed on the Siemens Prisma, the β-fraction value is above the desired 5% threshold and may be due to the non-uniform distribution of the β-fraction values in the fibre ring, resulting in a higher standard deviation of the measurements. The MSE CV is equal to 4.75% being higher compared to the other MRI scanners' Mean Squared Errors. This could be due to noisier acquisitions, as also seen in the lower SNR set to create the binary mask required to perform distortions corrections. Regarding the 1.5T GE Artist, the GE Premier located at Churchill Hospital, the results

Table 6.12: Bingham-NODDI model metrics results for a set of two acquisitions of phantom data performed on the 3T GE Premier located at the Churchill Hospital.

Bingham-NODDI model						
	ODI	**β-fraction**	**Tissue v.f.**	**Intra-neurite v.f.**	R^2	**MSE**
SCAN 1	0.0201 ± 0.0008	0.396± 0.253	0.957 ± 0.045	0.444 ± 0.789	0.985 ± 0.004	0.0012 ± 0.0004
SCAN 2	0.0202 ± 0.0007	0.473 ± 0.225	0.943 ± 0.078	0.452 ± 0.074	0.984 ± 0.006	0.0013 ± 0.0005
CV (%)	0.14 %	8.92%	0.76%	0.76%	0.076%	4.75%

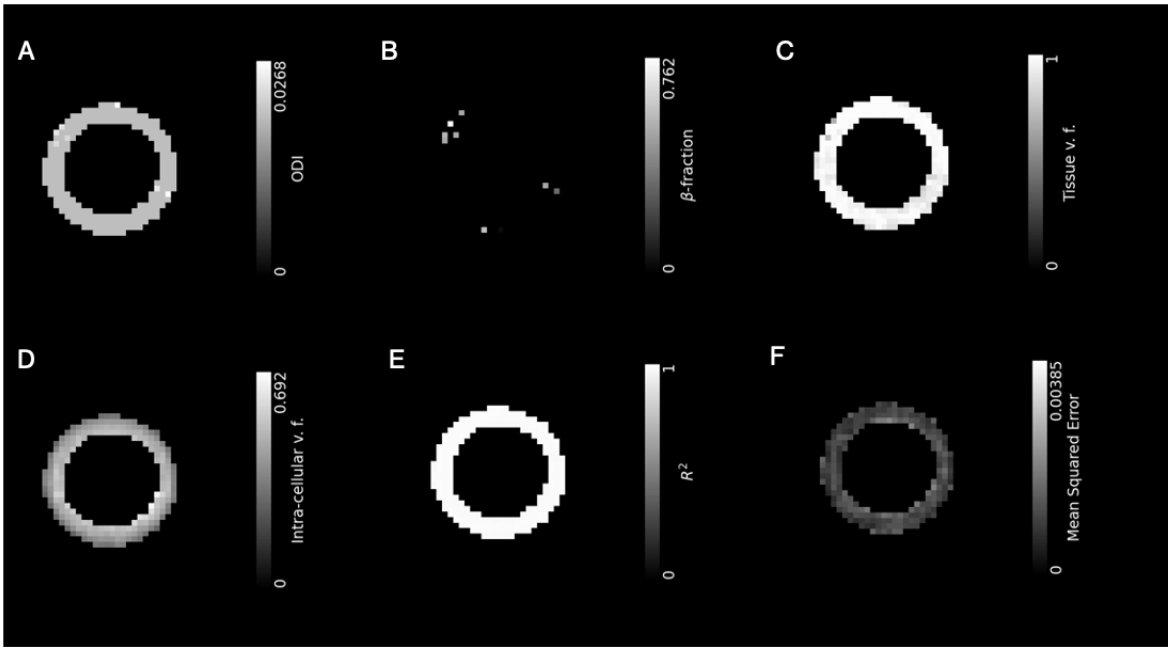

Figure 6.17: Quantitative maps of the parameters given as output by the Bingham-NODDI model fit on the phantom data acquired on the GE Premier located at the Churchill Hospital. The images represent (A) the ODI, (B) the β-fraction, (C) the Tissue volume fraction, (D) the Intra-cellular volume fraction, (D) the R^2 coefficient, (E) the MSE coefficient.

are shown below in Table 6.13. The quantitative maps for each Bignham-NODDI parameter are shown in Figure 6.18. The ODI values show consistency over time, with a CV equal to 0.99%. Similar considerations can be made for the intra-cellular and tissue volume fractions, as they show low values for the coefficient of variation. In particular, the tissue volume fraction values are close to 1, indicating the presence of neurites in the fibre ring region, as expected. The β-fraction CV is equal to 3.94%, below our desired threshold. The R^2 coefficient values are close to 1 and the low CV value suggests a satisfactory goodness of fit.

Table 6.13: Bingham-NODDI model metrics results for a set of two acquisitions of phantom data performed on the 1.5T GE Artist located at the Churchill Hospital.

Bingham-NODDI model						
	ODI	**β-fraction**	**Tissue v.f.**	**Intra-neurite v.f.**	**R^2**	**MSE**
SCAN 1	0.0212 ± 0.0049	0.446 ± 0.233	0.968 ± 0.049	0.525 ± 0.094	0.959 ± 0.011	0.0032 ± 0.0010
SCAN 2	0.0216 ± 0.0088	0.412 ± 0.239	0.967 ± 0.048	0.514 ± 0.091	0.963 ± 0.014	0.0030 ± 0.0012
CV (%)	0.99 %	3.94 %	0.1 %	1.03 %	0.15 %	4%

In order to compare the quantitative maps of the Bingham-NODDI model, the ODI, tis-

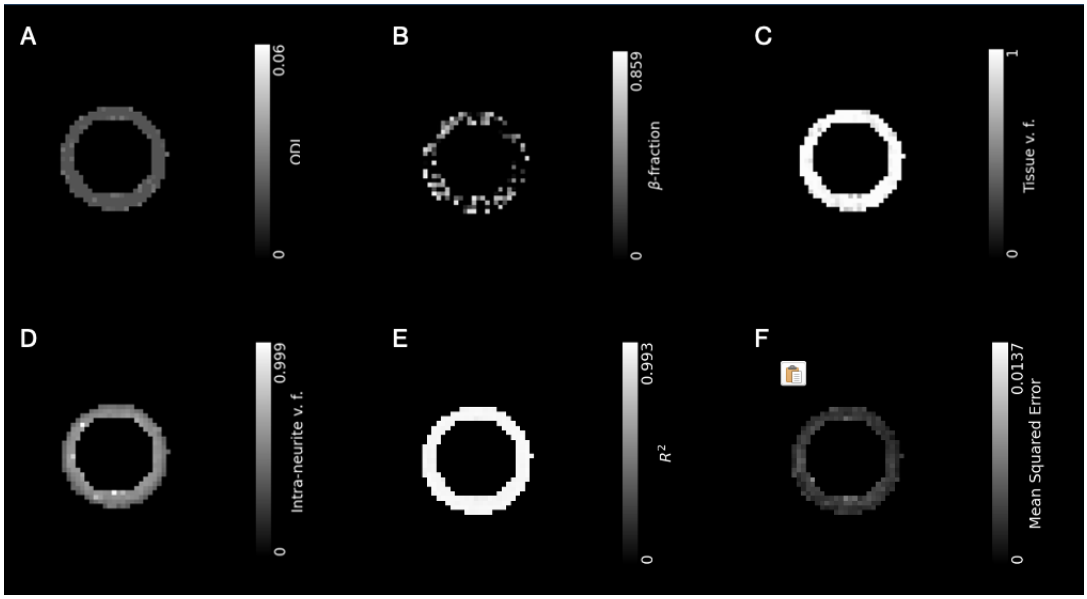

Figure 6.18: Quantitative maps of the parameters given as output by the Bingham-NODDI model fit on the phantom data acquired on the 1.5T GE Artist located at the Churchill Hospital. The images represent (A) the ODI, (B) the β-fraction, (C) the Tissue volume fraction, (D) the Intra-cellular volume fraction, (D) the R^2 coefficient, (E) the MSE coefficient.

sue and intra-cellular volume fractions, and the MSE quantitative maps of the first scan of each MRI scanner used in this multi-shell study are placed in Figure 6.19 and in Figure 6.20, to better visualize differences. After confirming intra-site repeatability, the initial scan from each distinct set of MRI scanner acquisitions was selected and displayed in Table 6.14. Notably, ODI values obtained on each scanner are congruent to each other within the margin of error, low values indicate all scanners are able to capture the low level of dispersion of neurites in the fibre ring region that simulates brain tissue. Similar considerations can be made regarding the intra-cellular volume fraction values, with values being all close to 1 and indicating a high proportion of brain tissue in the fibre ring region. The intra-cellular volume fraction is substantial across all acquisitions. The β-fraction varies, suggesting differences in the proportion of neurites with a Bingham distribution. MSE values are generally low, indicating low error in the model predictions, with the highest MSE observed in the GE Artist acquisition and R^2 values indicating a reliable goodness of fit for the model in all cases.

Overall, the Bingham-NODDI model demonstrates good consistency in capturing microstructural characteristics across different MRI scanners. The observed differences in β-fraction values highlight the importance of considering different protocols of acquisitions in microstructural modeling. Finally, the high R^2 values and low MSE indicate a robust fit of the model to the acquired data, supporting the reliability of results.
So, despite the tensor model highlighting some differences between the 3T MRI scanners and the GE Artist, specifically regarding the lower Mean Diffusivity values, the Bingham-NODDI model parameters are similar within the margin of errors, showing inter-site consistency and repeatability and assessing the reliability of the Bingham-NODDI model across all scanners.

The acquired diffusion data was also fitted to the linear formulation of the NODDI model,

Table 6.14: Bingham-NODDI metrics results for the first scan of the set of acquisitions on each MRI scanner system.

Bingham-NODDI model						
	ODI	**β-fraction**	**Tissue v.f.**	**Intra-neurite v.f.**	R^2	**MSE**
Siemens Prisma MONOPOLAR	0.0202 ± 0.0012	0.410 ± 0.256	0.969 ± 0.041	0.426 ± 0.069	0.988 ± 0.004	0.0009 ± 0.0003
Siemens Prisma BIPOLAR	0.0206 ± 0.0085	0.472 ± 0.236	0.958 ± 0.052	0.410 ± 0.077	0.987 ± 0.004	0.0010 ± 0.0004
GE Premier (OCMR)	0.0203 ± 0.0015	0.327 ± 0.261	0.969 ± 0.045	0.431 ± 0.069	0.986 ± 0.005	0.0011 ± 0.0004
GE Premier (Churchill H.)	0.0201 ± 0.0008	0.396± 0.253	0.957 ± 0.045	0.444 ± 0.789	0.985 ± 0.004	0.0012 ± 0.0004
GE Artist	0.0212 ± 0.0049	0.446 ± 0.233	0.968 ± 0.049	0.525 ± 0.094	0.959 ± 0.011	0.0032 ± 0.0010

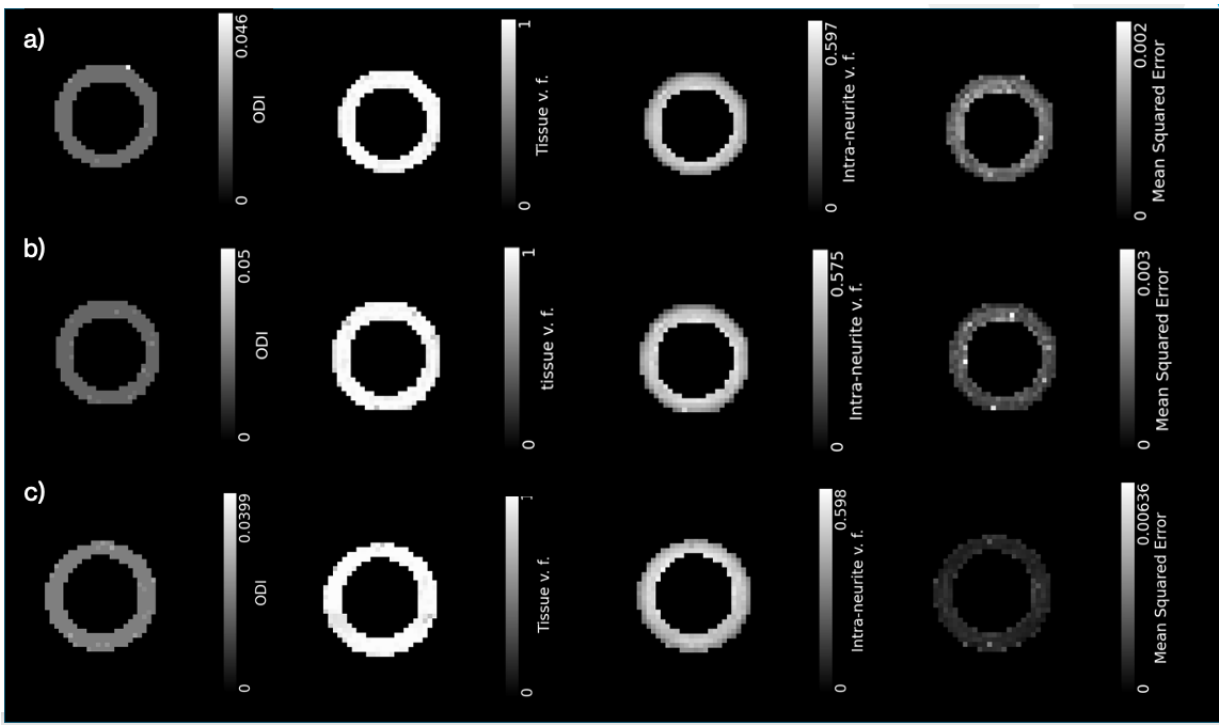

Figure 6.19: Quantitative maps of the parameters given as output by the Bingham-NODDI model fit on the phantom data acquired on the first row: Siemens Prisma Monopolar; second row: Siemens Prisma Bipolar; third row: GE Premier (OCMR). The images represent (A) the ODI, the Tissue volume fraction, the Intra-cellular volume fraction, and the MSE coefficient.

the AMICO-NODDI model, as described in Section 2.2. The implementation of the AMICO-NODDI model is described in Section 4.3. The obtained metrics results for phantom data acquired on each MRI scanner are shown in Table 6.15. For each set of acquisitions, the AMICO-NODDI model was fitted in order to obtain outcomes for the orientation dispersion index (ODI), the intra-cellular volume fraction (ICVF), which corresponds to the Intra-neurite volume fraction metric of the Bingham-NODDI model fit, and the isotropic volume fraction (ISOVF), describing the extra-cellular compartment, i.e. CSF. The quantitative maps for each parameter are displayed in Figure 6.21, Figure 6.22, and in Figure 6.23.

The ODI index values are constant across the different scanners, showing intra-site consistency with low coefficient of variation (CV) values. In particular, the acquisitions

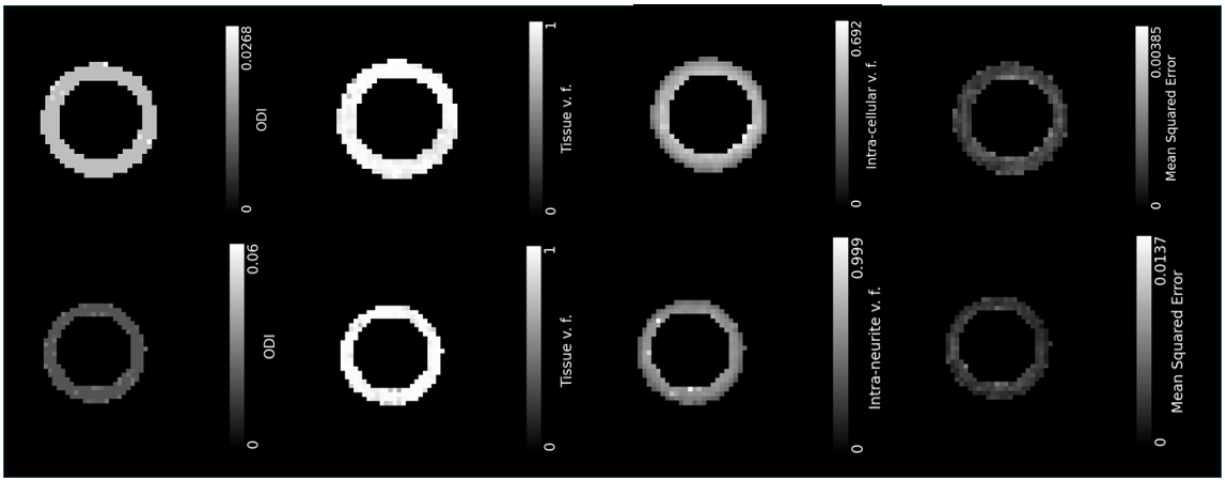

Figure 6.20: Quantitative maps of the parameters given as output by the Bingham-NODDI model fit on the phantom data acquired on the first row: GE Premier (Churchill Hospital); second row: GE Artist. The images represent (A) the ODI, the Tissue volume fraction, the Intra-cellular volume fraction, and the MSE coefficient.

performed on the GE Premier located at the OCMR have the lowest CV value. However, all ODI outcomes are slightly higher compared to those obtained by fitting the Bingham-NODDI model (Table 6.14). This may be due to the AMICO-NODDI mathematical formulation exploiting the Watson distribution rather than the Bingham distribution to model the neurite orientation distribution, possibly overestimating the ODI values due to its incapability to capture complex neurite configurations.

The ISOVF, shown in Figure 6.23, has low values, emphasizing how the ring region is mainly composed by a material mimicking neurite fibers in the human brain hence not CSF. This may also explain the higher standard deviation values, almost as high as the value itself thus affecting the CV, which has high values for all MRI scanners, except for the Siemens Prisma Bipolar acquisitions, having good repeatability while the GE Premier (Churchill) has the highest CV, suggesting greater variability.

The ICVF values, shown in Figure 6.22, are stable between scans for acquisitions performed on the Siemens Prisma (Monopolar and Bipolar) and on the GE Premier located at the OCMR while the acquisitions performed at the GE Premier located at the Churchill Hospital exhibits moderate variability between scans. The highest CV value is shown by data acquired on the GE Artist, still below the desired threshold of 5%. Overall, Siemens Prisma (Monopolar and Bipolar) and GE Premier (OCMR) show high repeatability for both ODI and volume fractions, with low CV values. Data acquired on the GE Artist also show good repeatability, particularly for ODI and ISOVF, with the exception of the ICVF, congruently with what expected by this study.

Notably, data acquired on the Siemens Prisma (Bipolar) demonstrates low variability across all metrics, however, this may be due to the fibre ring region being fitted by the model in a reduced dimension compared to the other ring regions hence having less voxels to compute the AMICO-NODDI model metrics on (Figure 6.21(B)). Furthermore, the consistency of results is evident, with minimal differences between scans for most metrics.

Table 6.15: AMICO-NODDI model metrics results obtained fitting to the phantom data acquired on: Siemens Prisma Monopolar and Bipolar, GE Premier (OCMR), GE Premier (Churchill Hospital) and GE Artist.

AMICO-NODDI model						
		Siemens Prisma MONOPOLAR	**Siemens Prisma BIPOLAR**	**GE Premier (OCMR)**	**GE Premier (Churchill H.)**	**GE Artist**
ODI	Scan 1	0.0301 ± 0.0010	0.0300 ± 0.0001	0.03000 ± 0.00006	0.03 ± 4e-06	0.0301 ± 0.0006
	Scan 2	0.0300 ± 0.0004	0.0300 ± 0.0004	0.03000 ± 0.00006	0.0301 ± 0.0014	0.0301 ± 0.0006
	CV (%)	0.09 %	0.02%	0.003%	0.16 %	0.001%
ISOVF	Scan 1	0.048 ± 0.040	0.05 ± 0.04	0.042 ± 0.036	0.053 ± 0.039	0.046 ± 0.037
	Scan 2	0.050 ± 0.043	0.05 ± 0.04	0.037 ± 0.033	0.074 ± 0.073	0.054 ± 0.044
	CV (%)	2.53 %	0.1%	5.6%	16.6 %	8.4%
ICVF	Scan 1	0.430 ± 0.082	0.412 ± 0.086	0.443 ± 0.069	0.453 ± 0.080	0.519 ± 0.083
	Scan 2	0.435 ± 0.073	0.417 ± 0.075	0.442 ± 0.066	0.462 ± 0.072	0.506 ± 0.082
	CV (%)	0.53 %	0.66%	0.12%	1.0 %	1.2%

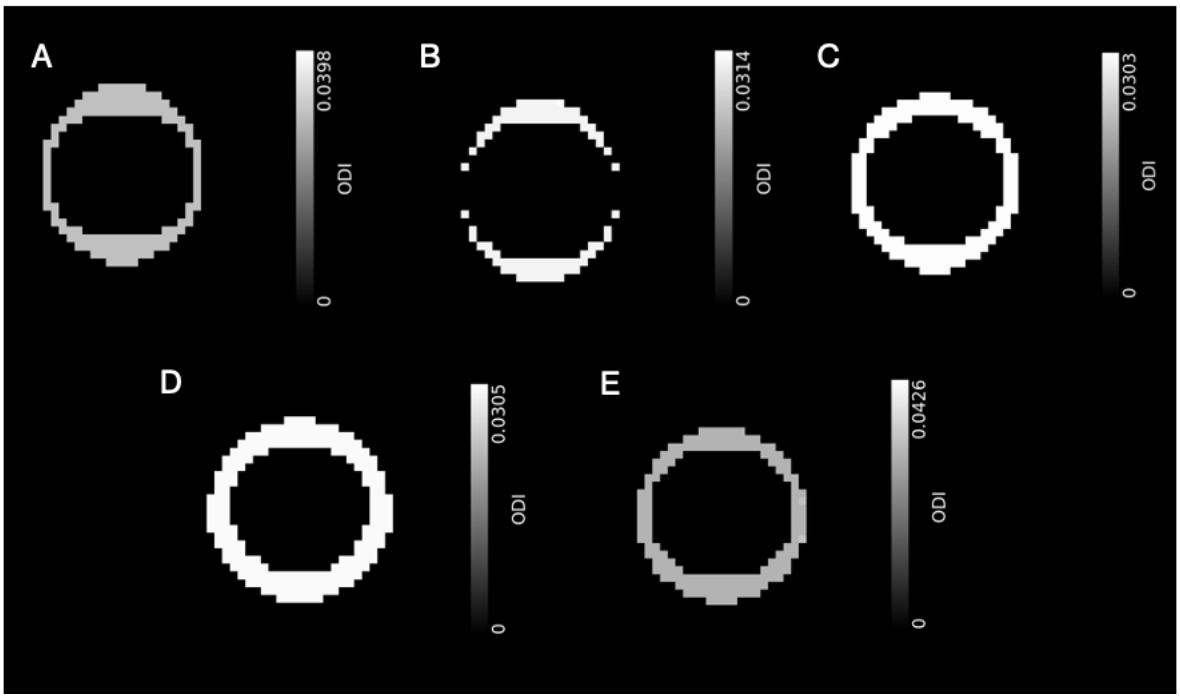

Figure 6.21: Quantitative maps of the ODI parameter given as output by the AMICO-NODDI model fit on the phantom data acquired on first row: Siemens Prisma Monopolar, Siemens Prisma Bipolar and GE Premier (OCMR): second row: GE Premier (Churchill Hospital) and GE Artist.

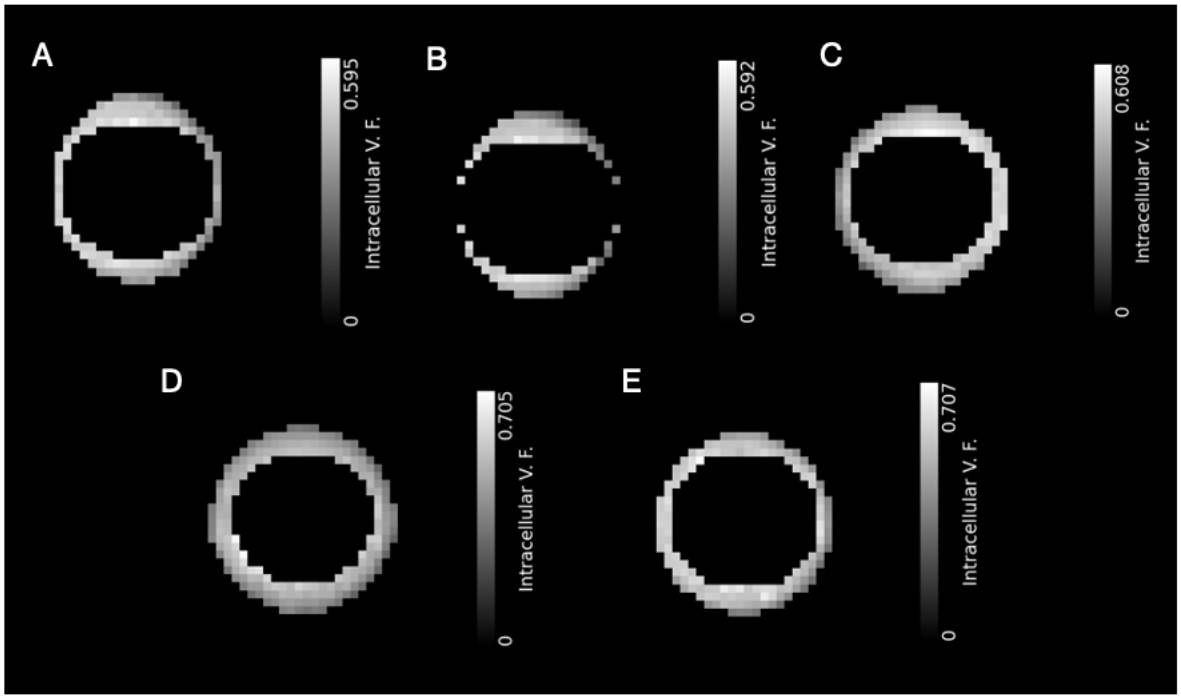

Figure 6.22: Quantitative maps of the Intra-cellular volume fraction parameter given as output by the AMICO-NODDI model fit on the phantom data acquired on first row: Siemens Prisma Monopolar, Siemens Prisma Bipolar and GE Premier (OCMR): second row: GE Premier (Churchill Hospital) and GE Artist.

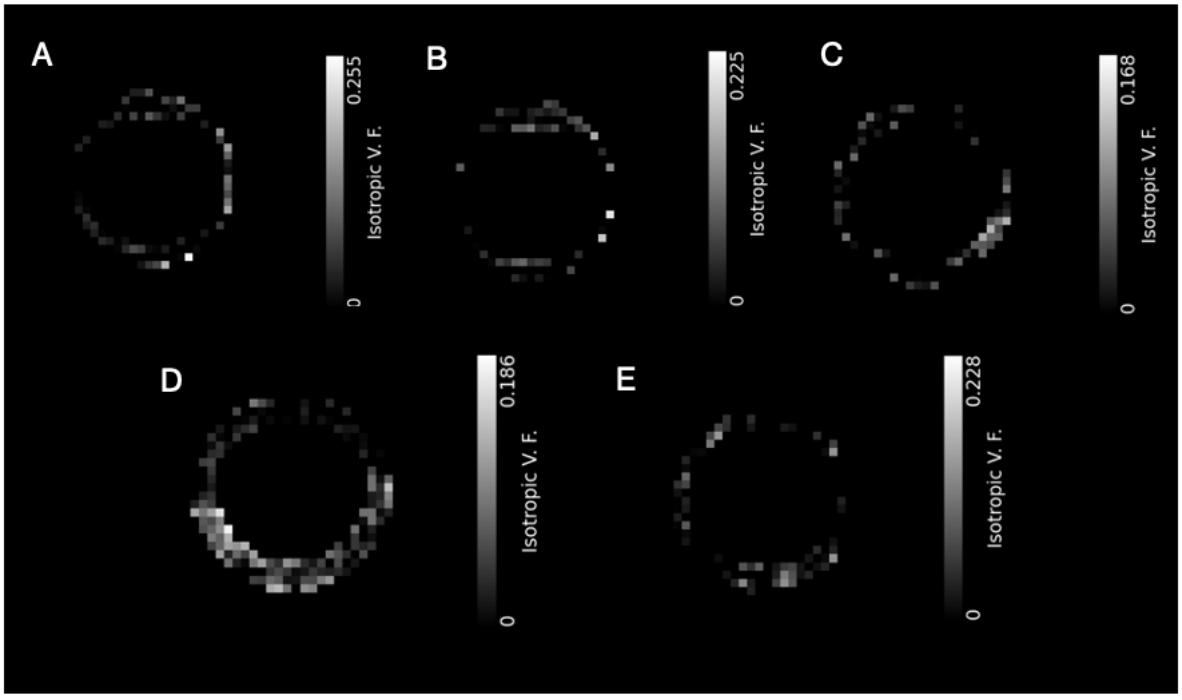

Figure 6.23: Quantitative maps of the Isotropic volume fraction parameters given as output by the AMICO-NODDI model fit on the phantom data acquired on first row: Siemens Prisma Monopolar, Siemens Prisma Bipolar and GE Premier (OCMR): second row: GE Premier (Churchill Hospital) and GE Artist.

Chapter 7

MULTIPLE TE and b-VALUES PHANTOM STUDY

In this chapter, we investigate the relationship between echo time and b-values with the tensor model metrics, i.e. Fractional Anisotropy (FA) and Mean Diffusivity (MD). Results in the previous chapter have shown how mean diffusivity values decrease when increasing the echo time (TE).

In particular, this has been highlighted when analyzing the phantom data acquired on the 1.5T GE Artist as due to the lower magnetic field, the minimum echo time allowed and set for the acquisition TE = 105 ms resulted in being higher compared to the echo times set for the phantom acquisitions on the 3T MRI scanners used for this study. Having dismissed the hypothesis attributing the observed results to the manual generation of the 3D binary ring mask utilized for extracting data from the fiber ring region—crafted meticulously for each distinct acquisition through the functionalities of FSLeyes applied to the eddy-corrected image—we have chosen to extend our examination into the relationship between echo time and the metrics derived from the tensor model. To do so, the DTI basic phantom was first scanned multiple times on the GE Premier located at the OCMR with different echo times with a single-shell and a multi-shell protocol. Then, the phantom was scanned with a single-shell and a multi-shell protocol using nine different b-values.

7.1 Multiple TE acquisitions

The DTI basic phantom was scanned with a single-shell protocol with different echo times consecutively, spanning the time interval of 10 ms, with a first echo time point TE = 56.3 ms up to TE = 126 ms. The single-shell protocol involved the acquisitions of 32 volumes with a b-value equal to 1000 and non-weighted volume. In the context of each acquisition, the phantom data underwent tensor model fitting to derive fractional anisotropy (FA) and mean diffusivity (MD) outcomes specifically from the fiber ring region. This extraction process was facilitated by employing a consistent 3D binary ring mask. The stability of the phantom, devoid of motion artifacts, ensured the precise placement of the identical ring on different images. Results of the tensor model metrics are shown in Table 7.1. As it is possible to notice, the results of the MD values decrease with increasing echo times. It is also possible to notice how, on the contrary, the FA values with the increase of echo times to the acceptable result of 0.78 ± 0.02 given by the manufacturer [46]. This suggests that a single-shell protocol may be enough to capture properly anisotropic diffusion information when the acquisitions are performed with a longer echo time. However,

this evidence should be further investigated on multiple scanners to infer information and compare results.

Regarding the MD decreasing values, a first hypothesis considered the decrease in mean diffusivity values to be linked with diffusion along the preferential direction. Increasing the echo time facilitates a greater diffusion of water molecules along the principal direction, where diffusion along orthogonal directions occurs at a substantially slower rate in comparison. Consequently, considering that the diffusion magnitude in the Diffusion Tensor Imaging (DTI) model, elucidated in Section 1.1, is delineated by the eigenvalues λ_1, λ_2, and λ_3, our hypothesis posits that the diffusion magnitude along the principal direction, denoted as μ_1 and governed by λ_1, should be greater than that along the other two directions (λ_2 and λ_3), exhibiting an increasing trend with increasing echo times if our conjecture holds true.

Table 7.1: Basic Phantom single-shell acquisitions with multiple TE values from TE = 56.3 ms to TE = 126 ms. For each acquisition, the Tensor model metrics results for FA and MD, and the mean values of the eigenvalues λ_1, λ_2 and λ_3 of the Diffusion Tensor Matrix are shown.

Tensor Model					
TE (ms)	FA	MD ($\cdot 10^{-3} mm^2$/s)	λ_1 (mm^2/s)	λ_2 (mm^2/s)	λ_3 (mm^2/s)
56.3	0.710 ± 0.083	0.930 ± 0.097	0.00186 ± 9.3e-05	0.00051 ± 0.00013	0.00042 ± 0.00013
66	0.739 ± 0.081	0.896 ± 0.093	0.00186 ± 7.6e-05	0.00046 ± 0.00013	0.00038 ± 0.00012
76	0.756 ± 0.082	0.873 ± 0.094	0.00184 ± 8.3e-05	0.00043 ± 0.00013	0.00035 ± 0.00012
86	0.766 ± 0.083	0.856 ± 0.089	0.00182 ± 8.7e-05	0.00042 ± 0.00013	0.00032 ± 0.00012
96	0.777 ± 0.086	0.841 ± 0.094	0.00181 ± 9.1e-05	0.00039 ± 0.00013	0.00031 ± 0.00013
106	0.784 ± 0.088	0.828 ± 0.099	0.00180 ± 0.00010	0.00038 ± 0.00014	0.00030 ± 0.00013
116	0.789 ± 0.085	0.823 ± 0.092	0.00180 ± 0.00011	0.00038 ± 0.00013	0.00029 ± 0.00012
126	0.796 ± 0.088	0.811 ± 0.100	0.00179 ± 0.00012	0.00037 ± 0.00013	0.00027 ± 0.00013

To analyze the eigenvalues results, the mean of each eigenvalue has been computed on the `dtifit` eigenvalues maps extracting the outcomes from the fibre ring region exploiting fslmaths. Results in Table 7.1 show that λ_1 is almost four times greater than λ_2 and λ_3, as expected given that it represents the magnitude of diffusion along the preferential direction. Notably, λ_2 and λ_3 decrease with increasing echo times. Furthermore, considering that the mean diffusivity is by definition (see Eq. (1.11)) the average of the eigenvalues, the decrease of λ_2 and λ_3 imply a decrease in MD. However, the changes appear to be almost minimal.

Similar considerations may be done with the acquisitions performed with a multi-shell protocol using three different b-values (b=0, 1000, 2600 s/mm^2). Results show the fractional anisotropy assumes acceptable values, showing that a multi-shell protocol is reliable for capturing diffusion properties through the tensor model metrics independently from the echo time. However, it is noticeable that FA values show an increasing trend with increasing echo time. Even in this case, the mean diffusivity values drop considerably with increasing echo times. Furthermore, the eigenvalues λ_2 and λ_3 values decrease but similarly to the single-shell acquisitions not drastically.

The diffusion data acquired with the multi-shell protocol were then fitted to the Bingham-NODDI model as it is crucial to assess the model's metrics results do not depend on the echo time to capture microstructural properties of the organization of neurites in the brain. The results are shown in Table 7.3. Results show consistency of the results hence proving the robustness of the model. In particular, the ODI values show perfect repeata-

bility whilst the Tissue and the Intra-neurite Volume Fraction show similar values within the margin of errors. These results confirm the independency of the Bingham-NODDI model from the echo time, as desired, hence proving the model's reliability once more.

Table 7.2: Basic Phantom multi-shell acquisitions with multiple TE values from TE = 70 ms to TE = 120 ms. For each acquisition, the Tensor model metrics results FA and MD, and the mean values of the eigenvalues λ_1, λ_2 and λ_3 of the Diffusion Tensor Matrix are shown.

Tensor Model					
TE (ms)	FA	MD ($\cdot 10^{-3} mm^2/s$)	λ_1 (mm^2/s)	λ_2 (mm^2/s)	λ_3 (mm^2/s)
70	0.793 ± 0.058	0.819 ± 0.063	0.00180 ± 8.4e-05	0.00036 ± 8.6e-05	0.00029 ± 7.9e-05
80	0.804 ± 0.060	0.802 ± 0.065	0.00179 ± 8.2e-05	0.00034 ± 8.7e-05	0.00028 ± 8.3e-05
100	0.816 ± 0.063	0.775 ± 0.064	0.00176 ± 9e-05	0.00031 ± 8.7e-05	0.00025 ± 8.3e-05
120	0.824 ± 0.068	0.745 ± 0.063	0.0017 ± 0.0001	0.00029 ± 9e-05	0.00023 ± 8.3e-05

Table 7.3: Bingham-NODDI model metrics results for each echo time used for this phantom study.

Bingham-NODDI model						
TE (ms)	**ODI**	**beta**	**Tissue v. f.**	**Intra-neruite v. f.**	**R^2**	**MSE**
70	0.020 ± 0.001	0.367 ± 0.251	0.96 ± 0.04	0.44 ± 0.07	0.983 ± 0.007	0.0014 ± 0.0006
80	0.020 ± 0.001	0.378 ± 0.252	0.97 ± 0.04	0.45 ± 0.08	0.984 ± 0.007	0.0013 ± 0.0005
100	0.020 ± 0.001	0.350 ± 0.244	0.97 ± 0.04	0.48 ± 0.09	0.982 ± 0.008	0.0015 ± 0.0007
120	0.020 ± 0.001	0.357 ± 0.261	0.96 ± 0.04	0.51 ± 0.10	0.978 ± 0.011	0.0018 ± 0.0009

7.2 Multiple b-values acquisitions

Up to now, the single-shell and multi-shell acquisitions provided phantom data with: SS = 32 diffusion-weighted volumes with b = 1000 s/mm^2 and one non-weighted b = 0 s/mm^2 image and MS = 90 diffusion-weighted volumes with b = 1000, 2600 s/mm^2 and one non-weighted b = 0 s/mm^2 image. To investigate the correlation between the decrease of the mean diffusivity and echo time we decided to perform phantom acquisition with a multi-shell protocol involving nine different b-values and the same single-shell protocol used in the previous acquisitions, to make comparisons.

The hypothesis posits that by incorporating more b-values in the relaxation curve fitting process, a more accurate fit is achieved. This is crucial because, with only two b-values, the fit essentially represents a straight curve, making it challenging for the tensor model to discern between the T_2 decay and diffusion-induced decay, see Figure 7.1.
It is noteworthy that the Bingham-NODDI model remains unaffected by the choice of b-values. Therefore, the acquisition protocol employed in the preceding chapter yields dependable results regardless of the specific b-values chosen.

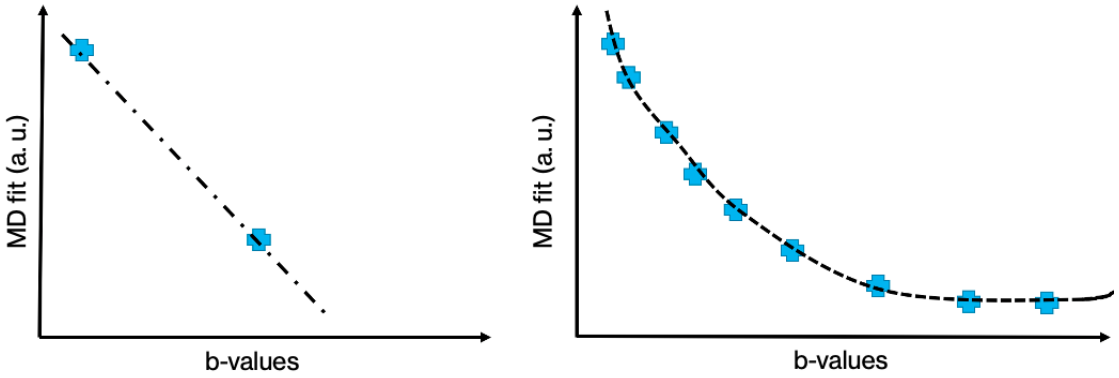

Figure 7.1: Schematic representation of the MD fit sampling b-values points.

Table 7.4: Tensor model metrics results obtained fitting to phantom data acquired with a multi-shell acquisition protocol with multiple b-values. The table shows mean and standard deviation values for FA and MD and the eigenvalues λ_1, λ_2 and λ_3 of the Diffusion Tensor Matrix obtained with the DTI fit.

TENSOR model - Multi Shell					
TE (ms)	**FA**	**MD** ($\cdot 10^{-3} mm^2$/s)	λ_1 (mm^2/s)	λ_2 (mm^2/s)	λ_3 (mm^2/s)
70	0.768 ± 0.056	0.806 ± 0.052	0.001724 ± 9.5e-05	0.00038 ± 7.6e-05	0.00031 ± 7e-05
110	0.805 ± 0.076	0.767 ± 0.080	0.001718 ± 0.000166	0.00033 ± 9.4e-05	0.00026 ± 8.9e-05

Results in Table 7.4 and in Table 7.5 show the MD values decreasing with increasing echo time despite the multiple b-values used for the fit. In particular, the same procedure regarding the computation of the eigenvalues applied in Section 7.1 was used to process this data. The obtained eigenvalues show a visible decrease with increasing echo time. However, computing the ratio of the variability of the eigenvalues outcomes in both the single-shell and multi-shell acquisitions, it results not uniform as λ_1 has a lower ratio. In particular, for the single-shell acquisitions, the ratios are $\lambda_{1,ratio} = 1.00$, $\lambda_{2,ratio} = 1.15$ and $\lambda_{3,ratio} = 1.19$. For the multi-shell acquisitions the ratios are $\lambda_{1,ratio} = 1.01$, $\lambda_{2,ratio}$

Table 7.5: Tensor model metrics results obtained fitting to phantom data acquired with a single-shell acquisition protocol. The table show mean and standard deviations values for FA and MD and the eigenvalues λ_1, λ_2 and λ_3 of the Diffusion Tensor Matrix obtained with the DTI fit.

TENSOR model - Single Shell					
TE (ms)	**FA**	**MD** ($\cdot 10^{-3} mm^2/s$)	λ_1 (mm^2/s)	λ_2 (mm^2/s)	λ_3 (mm^2/s)
70	0.741 ± 0.078	0.903 ± 0.097	0.00187 ± 8.1e-05	0.00046 ± 0.000126	0.00038 ± 0.00013
110	0.788 ± 0.081	0.840 ± 0.090	0.00184 ± 8.6e-05	0.00038 ± 0.00013	0.00030 ± 0.00012

= 1.21 and $\lambda_{3,ratio} = 1.27$.
Furthermore, the questions posed by the decrease in the MD values needs future further investigation.

Chapter 8

IN-VIVO BRAIN STUDY

In this chapter, the results of the analysis performed on the healthy volunteers is presented. *In-vivo* diffusion brain data were fitted to the tensor model and the NODDI models to obtain the metrics described in the previous chapter for the phantom data acquisitions hence describing the diffusion properties in the brain.

The diffusion brain data was acquired using two 3T MRI scanners: the Siemens Prisma with a single-refocused applied gradient (Monopolar acquisition protocol) and the GE Premier, located at the Oxford centre for Magnetic Resonance. The aim of this *in-vivo* study is to assess the intra-site stability and the inter-site repeatability of the results of the main diffusion models across different MRI scanners. Intra-site consistency is assessed by analyzing two sets of scans acquired on both 3T MRI scanners on one healthy volunteer. After that, inter-site comparisons to assess the repeatability of the diffusion models were made by analyzing two sets of scans acquired on two healthy volunteers.

Lastly, the last part of the chapter displays the comparisons of the *in-vivo* brain diffusion data fitted to the AMICO-NODDI model with the Bingham-NODDI model, as previously done with the phantom acquisitions.

8.1 GE PREMIER

To assess the intra-site consistency of the diffusion metrics over time, two healthy volunteers were scanned with the 3T Siemens Prisma using a monopolar acquisition protocol and a 21 channels head coil, available at the OCMR - University of Oxford. The acquisition protocol is described in Section 3.3.

In Figure 8.1, the original diffusion-weighted brain image acquired is shown. As it is possible to notice, the brain is warped, especially in the higher region. The figure also displays the binary brain mask, required to perform EDDY correction. The corrected image is finally shown, hence showing the brain image corrected of the distortions. In particular, the corrections are visible in the higher region of the brain. In Figure 8.2, the t1-weighted brain image used in the alignment to the MNI152 standard space is shown.
The acquired data was fitted to the tensor model in order to obtain the Fractional Anisotropy (FA) and Mean Diffusivity (MD) mean and standard deviations values. This is done using the `dtifit` function, implemented in fslpy.

The obtained quantitative maps are then aligned to the standard space MNI152 in order to extract results exploiting the same ROIs, displayed in Figure 5.5. In particular, the FA and MD maps were extracted from the Thalamus to infer information about the Gray

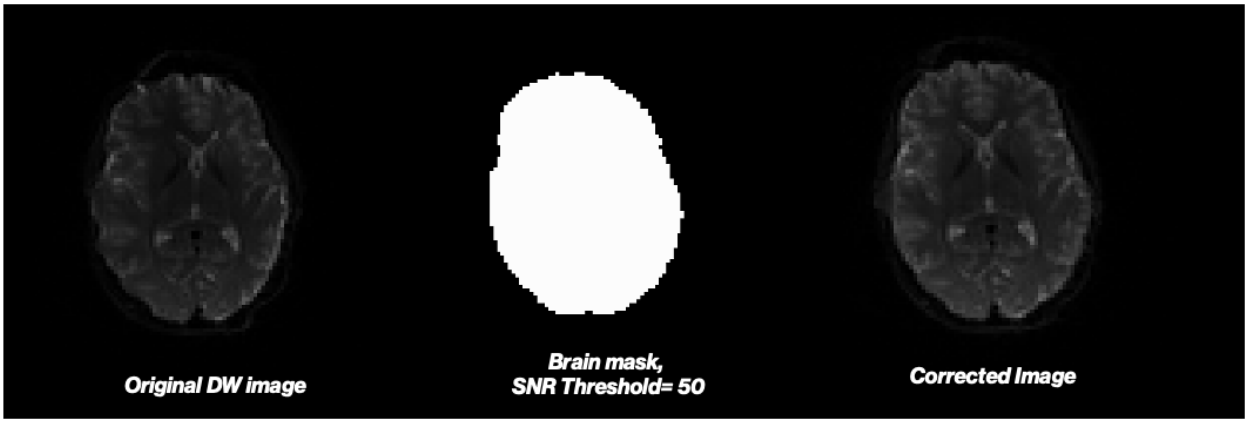

Figure 8.1: *In-vivo* brain diffusion data acquired on the GE Premier located at the OCMR

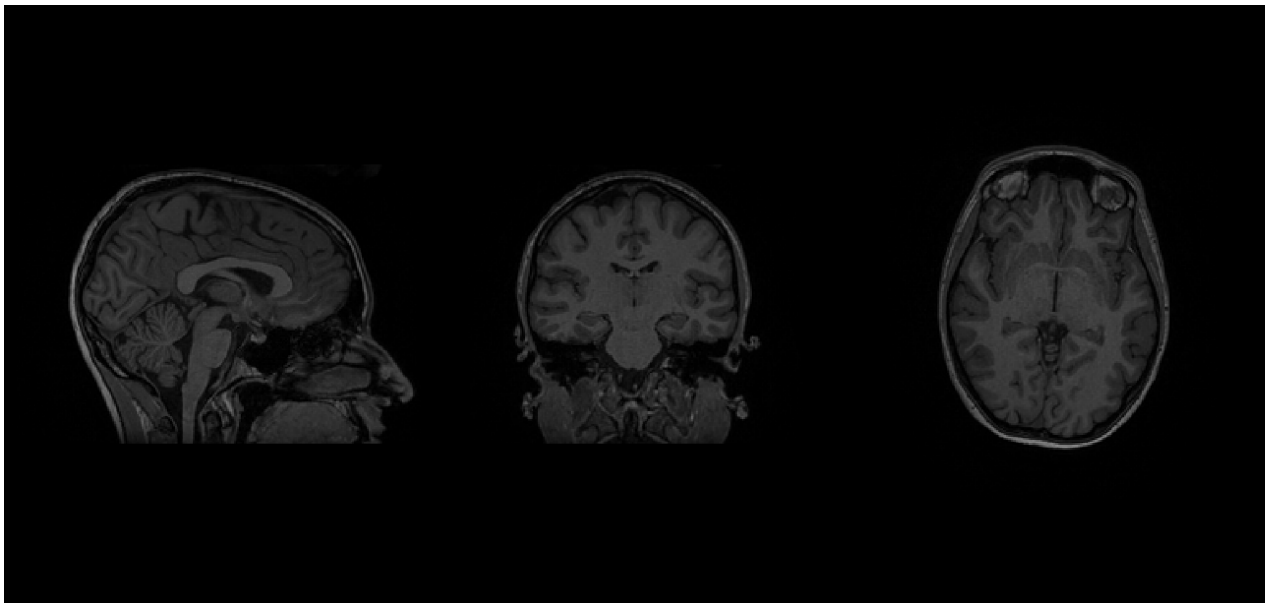

Figure 8.2: T1-weighted image of the brain acquired on the GE Premier, located at the OCMR.

Matter, from the Corpus Callosum to infer results about the White Matter, and from the Ventricles to infer results on the CSF.

The tensor model metrics results are shown in Table 8.1.

The quantitative maps of FA and MD are shown in Figure 8.3 and in Figure 8.4. In particular, the images show the fractional anisotropy and mean diffusivity values for the whole brain and for each selected ROI used to extract results, as aforementioned.

As it can be seen in Table 8.1, the FA values for corpus callosum are higher compared to those of obtained for the Thalamus and the Ventricles, highlighting the intricately organized nature of White Matter as opposed to the lower values of FA in the Ventricles, hence reflecting the isotropic diffusion of CSF, as expected in this region of the brain.

Regarding consistency of results, for both Scan 1 and Scan 2, FA and MD values are consistent, with slight variations. This is also confirmed by a low Coefficient of Variation (CV) at 0.08%, indicating a high level of repeatability. FA and MD values for the Thalamus show minor variability between the two scans, also confirmed by a relatively low level

Table 8.1: Tensor model metrics results for the *in-vivo* brain data acquired on the GE Premier located at the OCMR.

TENSOR model

		FA	**MD** ($\cdot 10^{-3} mm^2/s$)
Corpus Callosum	SCAN 1	0.577 ± 0.196	0.661 ± 0.145
	SCAN 2	0.578 ± 0.190	0.647 ± 0.127
	CV	0.08%	1.07%
Thalamus	SCAN 1	0.307 ± 0.078	0.724 ± 0.177
	SCAN 2	0.300 ± 0.070	0.686 ± 0.139
	CV	1.1%	2.69%
Ventricles	SCAN 1	0.346 ± 0.186	1.522 ± 0.370
	SCAN 2	0.325 ± 0.166	1.501 ± 0.310
	CV	3.1%	0.69%

of variation between scans. Finally, FA and MD values for the Ventricles demonstrate some variability between Scan 1 and Scan 2 but remain within a reasonable range. This is also confirmed by a slightly higher CV though still below our desired threshold of 5%.

Overall, the tensor model applied to *in-vivo* brain data on the GE Premier at the OCMR produces consistent results for all ROIs. The observed FA and MD values are generally small, indicating the robustness and reliability of the Tensor model.

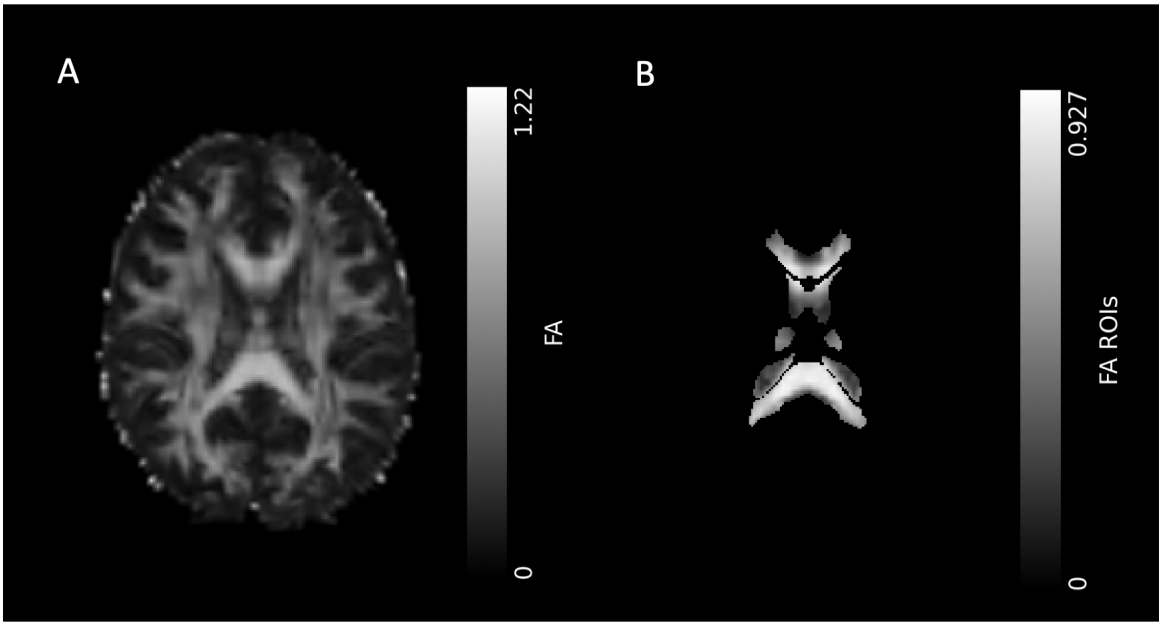

Figure 8.3: (A) Quantitative map of the FA of the whole brain aligned to MNI152 standard space, (B) quantitative map of FA for each selected ROI, i.e. Corpus Callosum, Thalamus and Ventricles.

The results obtained fitting the diffusion brain data acquired on the GE Premier of a healthy volunteer are shown in Table 8.2. The quantitative maps for each Bingham-

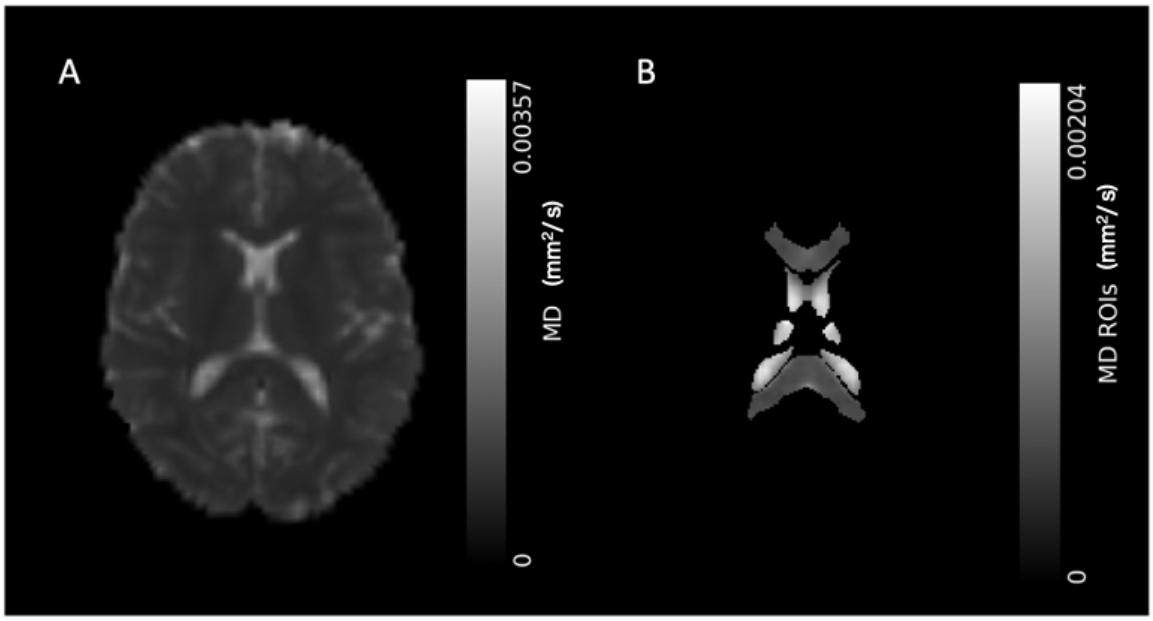

Figure 8.4: (A) Quantitative map of the MD of the whole brain aligned to MNI152 standard space, (B) quantitative map of MD for each selected ROI, i.e. Corpus Callosum, Thalamus and Ventricles.

NODDI model parameter for the whole brain are shown in Figure 8.5. These are the results of the parameters of the Bingham-NODDI model fit not aligned to the MNI152 standard space. The quantitative maps obtained by the fit for each parameter were then aligned to the MNI152 standard space, to better compare results based on a reference system. Furthermore, the quantitative maps for each selected ROI are displayed in Figure 8.6, Figure 8.7, Figure 8.8, Figure 8.9, Figure 8.10, Figure 8.11, and in Figure 8.12.

Regarding the obtained results for Genu of Corpus Callosum, the ODI values for scan 1 and scan 2 are similar, with low variability (CV= 0.48 %). This suggests good repeatability in measuring the orientation dispersion in the Genu. The β-fraction, Tissue volume fraction and Intra-neurite Volume Fraction show similar metrics results, exhibiting low variability, as also confirmed by the CV values of each of these parameters hence suggesting consistent results between the two scans. The high R^2 values for both scans (0.980 and 0.967) indicate a strong fit of the Bingham-NODDI model to the data while the low MSE values (0.0013 and 0.0022) further support the model's goodness of fit. Similar considerations can be made for the Splenium of CC and the Anterior and Posterior limbs of Internal Capsule, showing low variability through scans. Thalamus, Caudate, and Putamen regions also exhibit low variability in the measured metrics, indicating the intra-site consistency of the Bingham-NODDI model fitted to *in-vivo* acquisitions.

The quantitative maps in Figure 8.6 show a great contrast between gray and white matter arising from the difference in the ODI index values between the two tissue types. White matter has lower ODI values, indicating a more structured neurite arrangement, with little dispersion about the dominant orientation of fiber tracts. Viceversa, grey matter is characterized by higher ODI values hence suggesting that gray matter does not exhibit organized fibre tracts like white matter. Notably, the ODI values in the Ventricles region are very close to zero, as Ventricles are mainly composed of Cerebral Spinal Fluid hence marking the absence of cells.

Table 8.2: Bingham-NODDI metrics results of a set of two *in-vivo* acquisitions on the GE Premier of a healthy volunteer to assess intra-site repeatability.

Bingham-NODDI model							
		ODI	**β-fraction**	**Tissue v. f.**	**Intra-neurite v. f.**	**R^2**	**MSE**
Genu CC	SCAN 1	0.103 ± 0.089	0.582 ± 0.202	0.82 ± 0.17	0.56 ± 0.11	0.980 ± 0.008	0.0013 ± 0.0006
	SCAN 2	0.102 ± 0.088	0.603 ± 0.211	0.83 ± 0.15	0.56 ± 0.11	0.967 ± 0.013	0.0022 ± 0.0009
	CV	0.48%	1.78%	0.49%	0.27%	0.67%	24.4%
Splenium CC	SCAN 1	0.079 ± 0.077	0.583 ± 0.200	0.86 ± 0.10	0.64 ± 0.11	0.979 ± 0.006	0.0014 ± 0.0005
	SCAN 2	0.075 ± 0.075	0.597 ± 0.196	0.85 ± 0.11	0.64 ± 0.11	0.972 ± 0.008	0.0019 ± 0.0006
	CV	2.79%	1/16%	0.79%	0.61%	0.38%	15.2%
Anterior limb IC	SCAN 1	0.193 ± 0.099	0.491 ± 0.183	0.939 ± 0.051	0.549 ± 0.073	0.976 ± 0.008	0.0014 ± 0.0005
	SCAN 2	0.190 ± 0.091	0.487 ± 0.177	0.938 ± 0.049	0.549 ± 0.072	0.971 ± 0.010	0.0015 ± 0.0006
	CV	0.67%	0.45%	0.01%	0.04%	0.27%	10.3%
Posterior limb IC	SCAN 1	0.119 ± 0.041	0.521 ± 0.233	0.881 ± 0.041	0.65 ± 0.06	0.977 ± 0.008	0.0013 ± 0.0005
	SCAN 2	0.116 ± 0.049	0.516 ± 0.250	0.887 ± 0.042	0.66 ± 0.06	0.973 ± 0.009	0.0016 ± 0.0006
	CV	1.71%	0.51%	0.34%	0.10%	0.22%	9.42%
Thalamus	SCAN 1	0.181 ± 0.073	0.622 ± 0.206	0.921 ± 0.131	0.424 ± 0.061	0.981 ± 0.005	0.0011 ± 0.0003
	SCAN 2	0.186 ± 0.070	0.649 ± 0.191	0.946 ± 0.097	0.434 ± 0.061	0.973 ± 0.009	0.0016 ± 0.0006
	CV	1.34%	2.07%	1.30%	1.12%	0.40%	17.6%
Caudate	SCAN 1	0.423 ± 0.147	0.524 ± 0.173	0.834 ± 0.201	0.446 ± 0.076	0.981 ± 0.012	0.0012 ± 0.0007
	SCAN 2	0.405 ± 0.131	0.562 ± 0.170	0.850 ± 0.179	0.441 ± 0.068	0.97 ± 0.01	0.0019 ± 0.0010
	CV	2.28%	3.52%	0.98%	0.63%	0.58%	23.37%
Putamen	SCAN 1	0.417 ± 0.136	0.542 ± 0.178	0.986 ± 0.010	0.460 ± 0.031	0.979 ± 0.003	0.0012 ± 0.0002
	SCAN 2	0.439 ± 0.138	0.542 ± 0.174	0.987 ± 0.010	0.468 ± 0.025	0.976 ± 0.006	0.0014 ± 0.0004
	CV	2.6%	0.04%	0.02%	0.83%	0.18%	8.02%

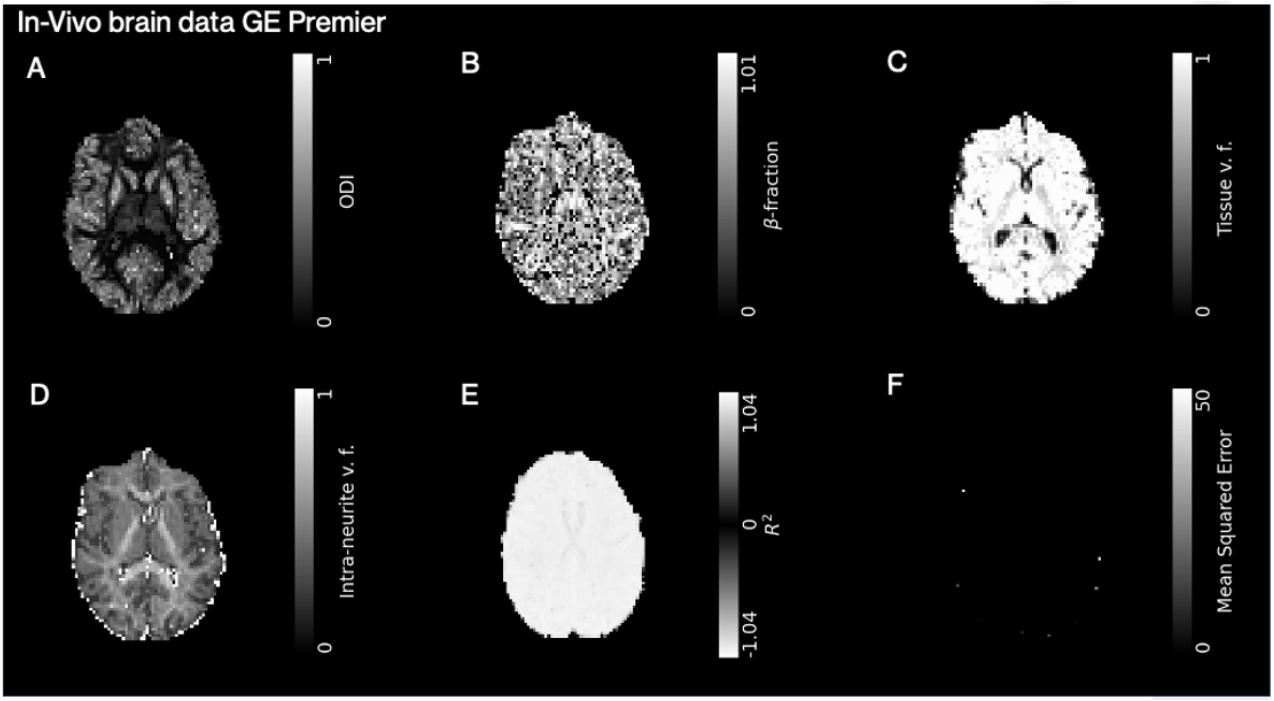

Figure 8.5: Quantitative maps of the metrics obtained fitting the diffusion brain data acquired on the GE Premier located at the OCMR to the Bingham-NODDI model: (A) The ODI index, (B) The β-fraction, (C) The tissue volume fraction, (D) The intra-neurite volume fraction, (E) The R^2 coefficient, (F) The Mean Squared Error (MSE) coefficient.

On the other hand, in Figure 8.8, it is possible to notice how the tissue volume fraction is close to one in regions characterised by the presence of gray and white matter, highlighting the very low presence of inter-cellular water filling the spaces between adjacent cells in a tissue. Furthermore, the tissue volume fraction index shows values close to zero in the Ventricles, as we don't expect to have brain tissues located in this region.

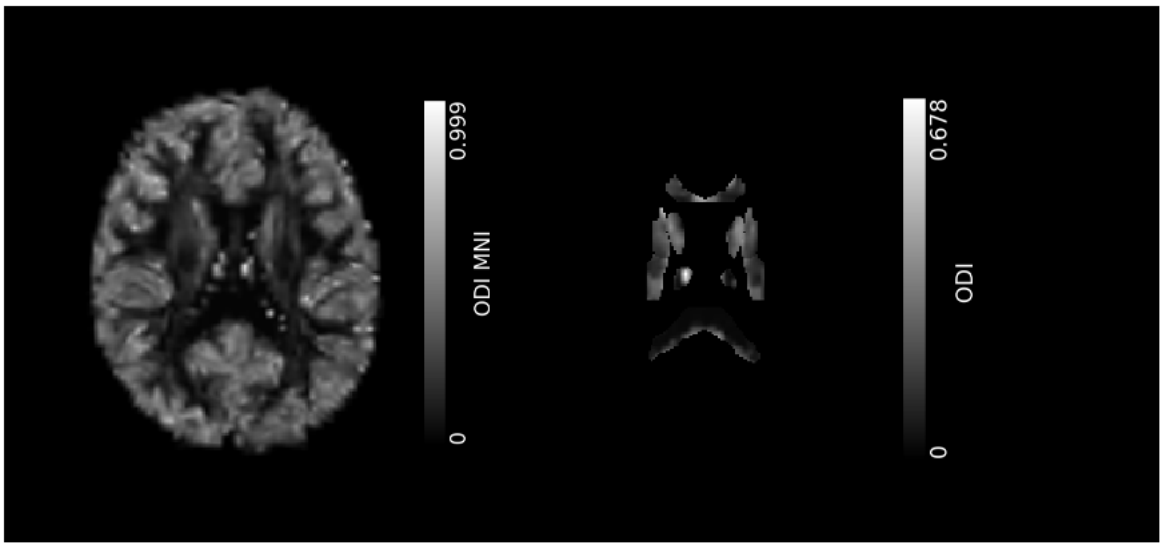

Figure 8.6: Quantitative maps of the ODI index obtained fitting the diffusion brain data acquired on the GE Premier located at the OCMR to the Bingham-NODDI model: on the left, the ODI map fitted to the MNI152 space: on the right the ODI index for each selected ROI, i.e. Genu and Splenium of Corpus Callosum, Anterior and Posterior Limbs of Internal Capsule, Thalamus, Putamen, and Caudate.

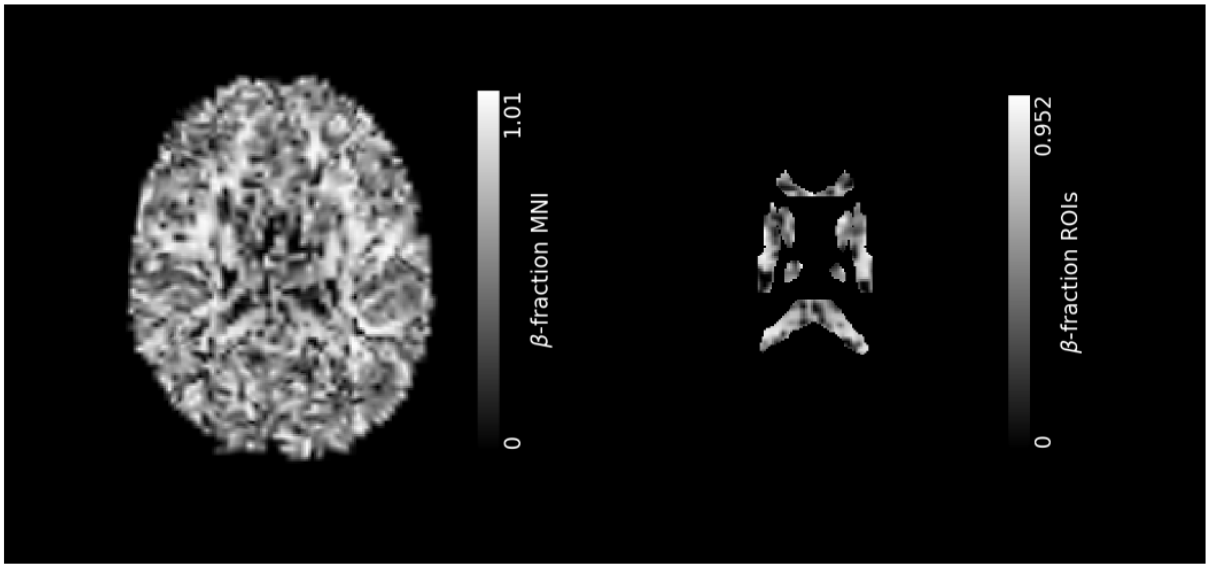

Figure 8.7: Quantitative maps of the β-fraction index obtained fitting the diffusion brain data acquired on the GE Premier located at the OCMR to the Bingham-NODDI model: on the left, the β-fraction map fitted to the MNI152 space: on the right the β-fraction index for each selected ROI, i.e. Genu and Splenium of Corpus Callosum, Anterior and Posterior Limbs of Internal Capsule, Thalamus, Putamen and Caudate.

In Figure 8.5, the quantitative maps show the fraction of axons and dendrites in the brain. It is evident that values are higher in the Genu and Splenium of the Corpus Callosum as well as in the Anterior and Posterior Limbs of the Internal Capsule compared to the regions of the Thalamus, Caudate, and putamen, as these regions are predominantly characterized by the presence of white matter. This indicated that white matter has a

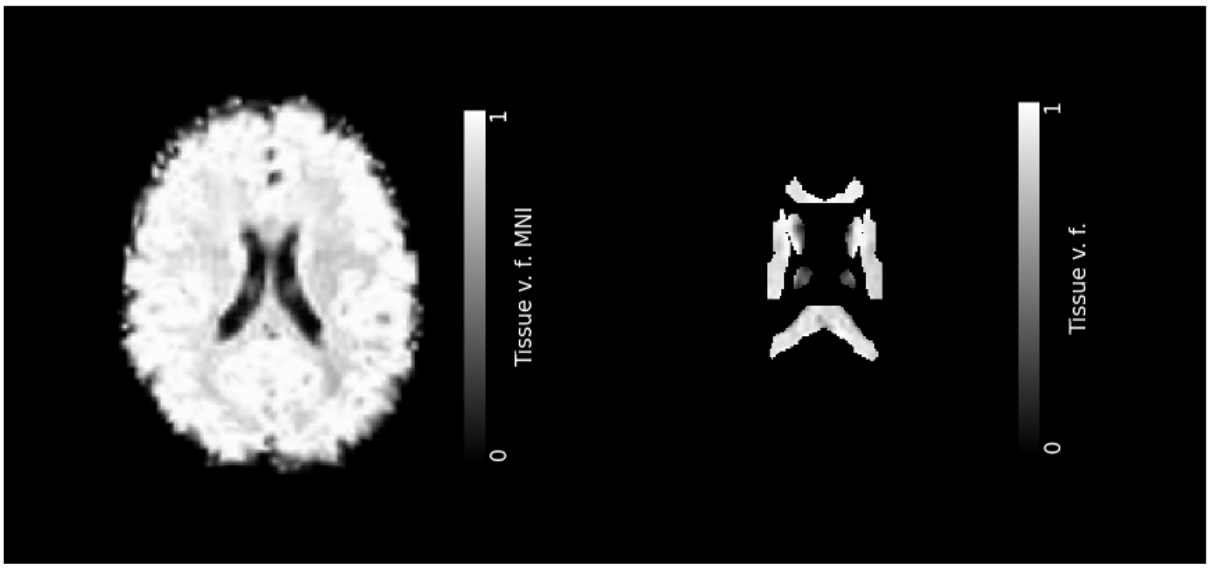

Figure 8.8: Quantitative maps of the Tissue Volume Fraction index obtained fitting the diffusion brain data acquired on the GE Premier located at the OCMR to the Bingham-NODDI model: on the left, the Tissue Volume Fraction map fitted to the MNI152 space: on the right the Tissue Volume Fraction index for each selected ROI, i.e. Genu and Splenium of Corpus Callosum, Anterior and Posterior Limbs of Internal Capsule, Thalamus, Putamen and Caudate.

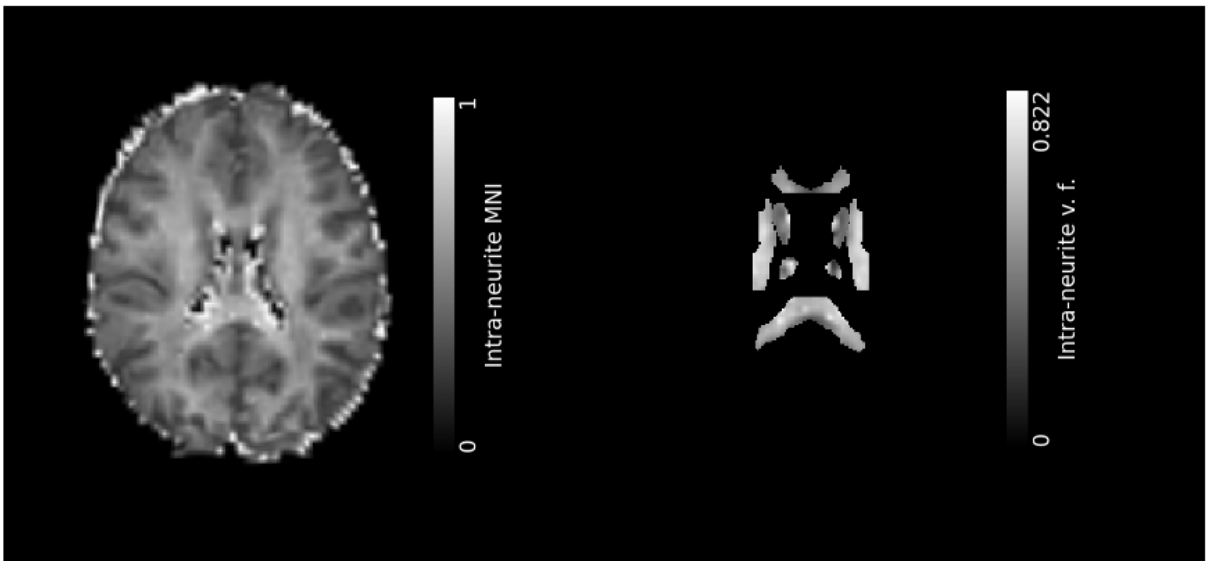

Figure 8.9: Quantitative maps of the Intra-neurite Volume Fraction index obtained fitting the diffusion brain data acquired on the GE Premier located at the OCMR to the Bingham-NODDI model: on the left, the Intra-neurite Volume Fraction map fitted to the MNI152 space: on the right the Intra-neurite Volume Fraction index for each selected ROI, i.e. Genu and Splenium of Corpus Callosum, Anterior and Posterior Limbs of Internal Capsule, Thalamus, Putamen and Caudate.

higher density of neurites when compared to gray matter.

Figure 8.10 shows the extra-cellular component obtained by fitting the Bingham-model to *in-vivo* results. Notably, the extra-cellular component's values are higher in the region

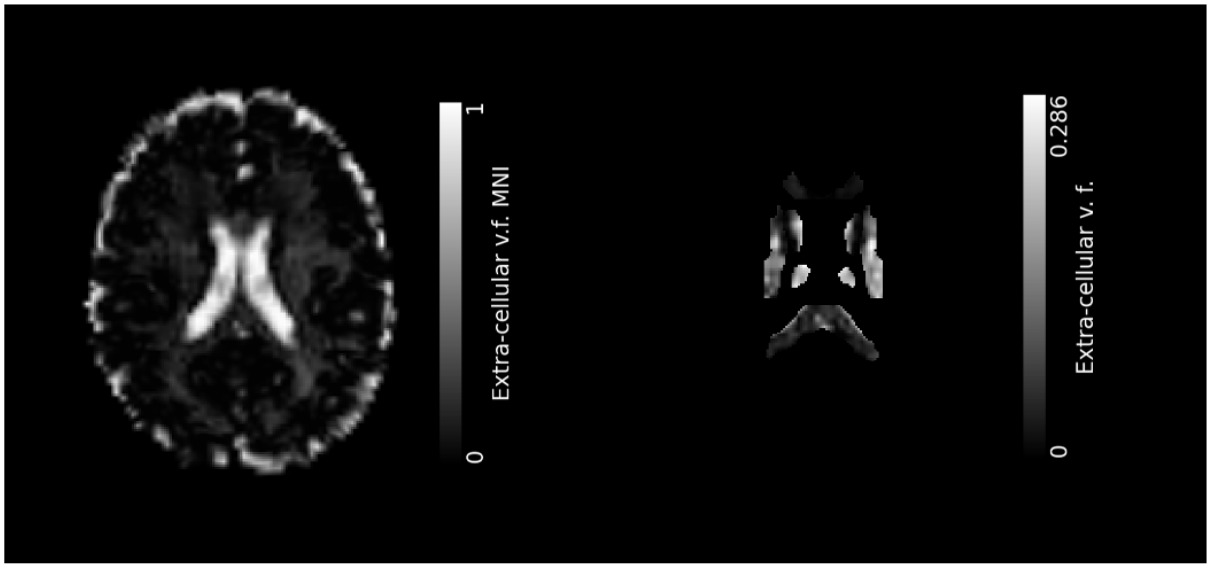

Figure 8.10: Quantitative maps of the Extra-cellular Volume Fraction index obtained fitting the diffusion brain data acquired on the GE Premier located at the OCMR to the Bingham-NODDI model: on the left, the Extra-cellular Volume Fraction map fitted to the MNI152 space: on the right the Extra-cellular Volume Fraction index for each selected ROI, i.e. Genu and Splenium of Corpus Callosum, Anterior and Posterior Limbs of Internal Capsule, Thalamus, Putamen and Caudate.

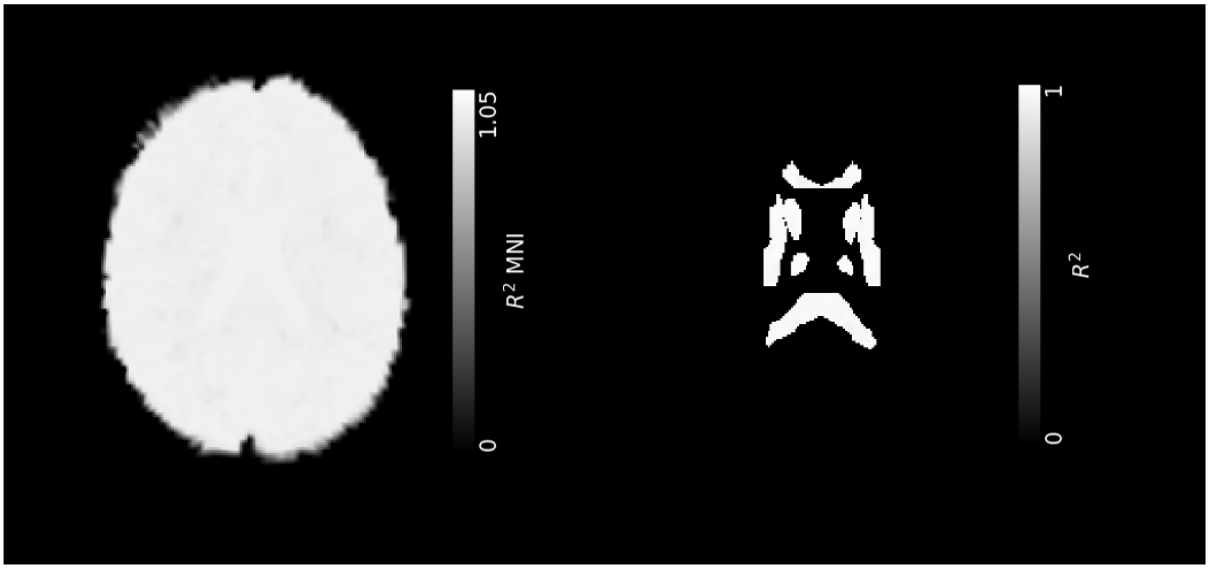

Figure 8.11: Quantitative maps of the R^2 index obtained fitting the diffusion brain data acquired on the GE Premier located at the OCMR to the Bingham-NODDI model: on the left, the R^2 map fitted to the MNI152 space: on the right the R^2 index for each selected ROI, i.e. Genu and Splenium of Corpus Callosum, Anterior and Posterior Limbs of Internal Capsule, Thalamus, Putamen and Caudate.

corresponding to the Ventricles, as expected, as it depicts the main presence of CSF inside this brain region whilst showing lower values in the rest of the brain.

Figure 8.11 and Figure 8.12 show the statistical coefficient indicating the goodness of fit in the case of the *in-vivo* acquisitions. The coefficients shoul not display the brain structure

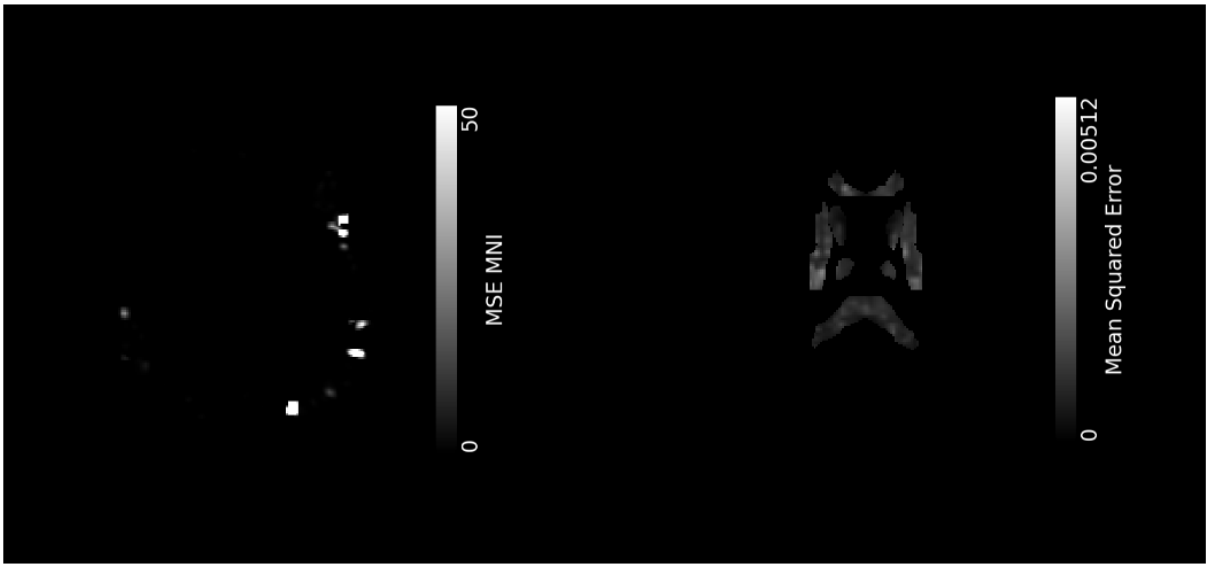

Figure 8.12: Quantitative maps of the Mean Squared Error index obtained fitting the diffusion brain data acquired on the GE Premier located at the OCMR to the Bingham-NODDI model: on the left, the Mean Squared Error map fitted to the MNI152 space: on the right the Mean Squared Error index for each selected ROI, i.e. Genu and Splenium of Corpus Callosum, Anterior and Posterior Limbs of Internal Capsule, Thalamus, Putamen and Caudate.

of the fitted data, as it indicates that the model is able to fit the acquired data equally well everywhere. Figure 8.12 shows white voxels indicating higher values of the MSE that do not produce a precise structure. Furthermore, the values of the MSE were thresholded to better visualize the coefficient properties as the original visualization could not be clear otherwise. Figure 8.11 shows the high values obtained for the R^2 coefficient, indicating the robustness of the fit as the values extracted from the white matter ROIs and those obtained from the gray matter ROIs are similar within the margin of errors.

8.2 SIEMENS PRISMA

Following the initial scanning of the healthy volunteer on the GE Premier system, subsequent analysis involved two additional acquisitions of the same individual on the Siemens Prisma, employing a monopolar acquisition protocol. The analysis protocol mirrored that applied to the GE Premier images, encompassing the fitting of the tensor model to the diffusion brain data, followed by fitting to the NODDI models. Relevant parameters were then extracted from region-of-interests (ROIs) tailored to yield results from both gray and white matter.

Notably, the Siemens Prisma acquisitions employed a phase encoding gradient oriented from left to right, differing from the GE Premier acquisition. To facilitate accurate data fitting, a new file incorporating acquisition parameter information was generated to rectify distortions affecting the Siemens Prisma images. Subsequently, the images were aligned with the MNI152 standard space, ensuring a consistent reference system for reliable extraction of results and facilitating meaningful inter-site comparisons.

The original diffusion brain images are shown in Figure 8.13, together with the binary brain mask required to perform distortions corrections and the final corrected image. The original diffusion brain image is warped on both sides of the brain, indicating it has been affected by distortions, then corrected in the final image used to be fitted. Figure 8.14 shows the T1-weighted image of the brain acquired on the Siemens Prisma.

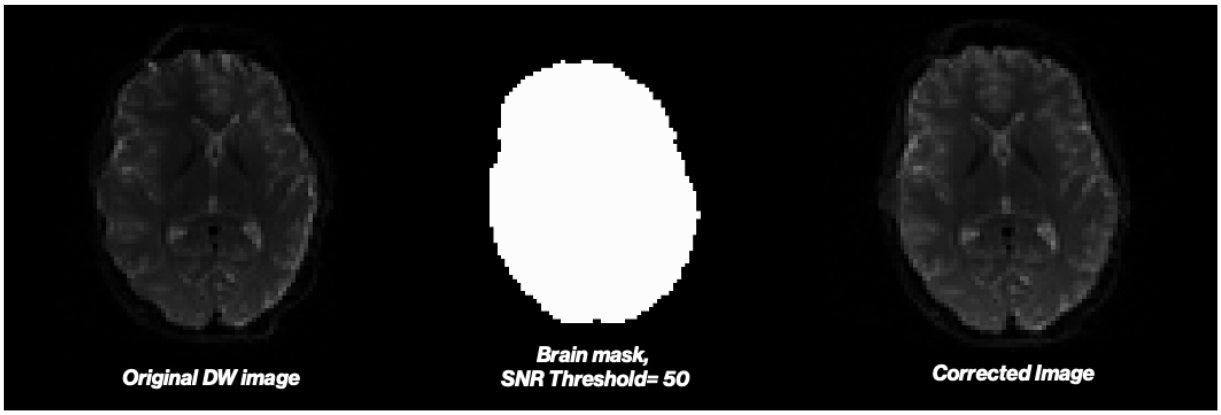

Figure 8.13: *In-vivo* brain diffusion data acquired on the Siemens Prisma with a monopolar acquisition protocol.

The tensor model metrics results are shown in Figure 8.3. The quantitative maps of FA and MD are shown in Figure 8.15 and in Figure 8.16. In particular, the images show the fractional anisotropy and mean diffusivity values for the whole brain and for each selected ROI used to extract results, i.e. Ventricles for the CSF analysis, Thalamus for the Gray Matter analysis, and the Corpus Callosum for the White Matter analysis.
Corpus Callosum fractional anisotropy and mean diffusivity results are similar suggesting consistency between scans, also confirmed by the low coefficient of variation values, indicating good repeatability. FA values are lower compared to the Corpus Callosum, indicating a lower level of anisotropy in this brain region compared to those in the Corpus Callosum, characterized by the presence of white matter tracts through which water diffuses preferentially. Low CV suggests little variability. The FA values extracted from the Ventricles' region are lower, indicating lower anisotropy, as expected due to the free movement of water in this brain region. Values are consistent between scans and low CV

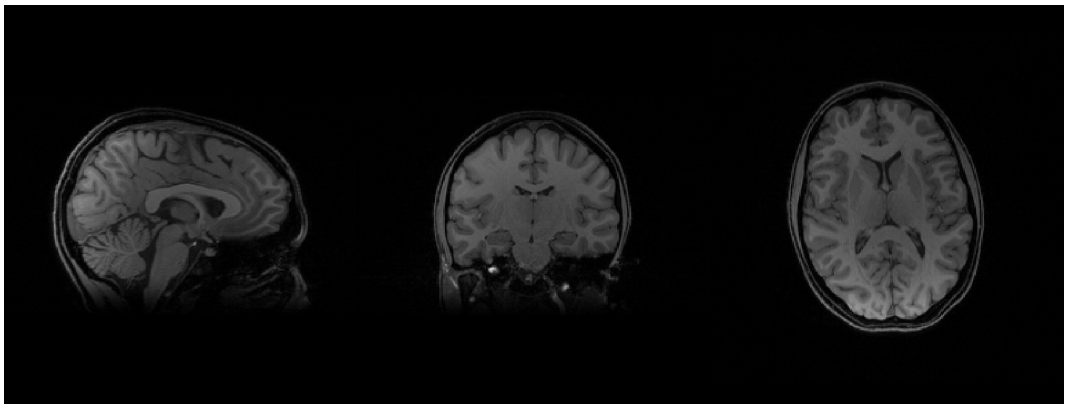

Figure 8.14: T1-weighted image of the brain acquired on the Siemens Prisma with a Monopolar acquisition protocol.

Table 8.3: Tensor model metrics results for diffusion brain data acquired on the Siemens Prisma with a Monopolar acquisition protocol.

TENSOR model			
		FA	**MD** ($\cdot 10^{-3} mm^2/s$)
Corpus Callosum	SCAN 1	0.6564 ± 0.1700	0.650 ± 0.146
	SCAN 2	0.6563 ± 0.1677	0.646±0.141
	CV	0.009%	0.31%
Thalamus	SCAN 1	0.331 ± 0.078	0.657 ± 0.117
	SCAN 2	0.335 ± 0.077	0.665 ± 0.133
	CV	0.62%	0.61%
Ventricles	SCAN 1	0.274 ± 0.126	1.741 ± 0.290
	SCAN 2	0.284 ± 0.134	1.740 ± 0.308
	CV	1.71%	0.02%

values suggest high reproducibility of the obtained results.

The quantitative maps show uniform distribution of FA and MD values, the discussed consideration about diffusion properties are also evidently displayed in the selected ROIs. The results obtained for the Genu of the CC show similar values for the ODI index, β-fraction, Tissue volume fraction, and Intra-neurite volume fraction. The CV values are all low, indicating low variability. Similar to the Genu of the CC, scan 1 and scan 2 results of the Splenium of the CC are consistent, indicating good repeatability. The Anterior Limb of IC shows consistent results between scans, while the intra-neurite volume fraction and MSE have a slightly higher CV. The Thalamus results show one of the highest CV values for the tissue volume fraction, suggesting a relatively higher variability in this metric whilst the Caudate results have a generally low CV, except for MSE, which has a higher CV. Finally, the Putamen results demonstrate very low CV values, indicating high repeatability and low variability in the measured metrics. Overall, the Bingham-NODDI model results suggest intra-site repeatability for the assessed brain regions, with low coefficients of variation in most metrics. Notably, the Mean Squared Error's coefficients of variation of the GE Premier have higher variability between scans compared to the

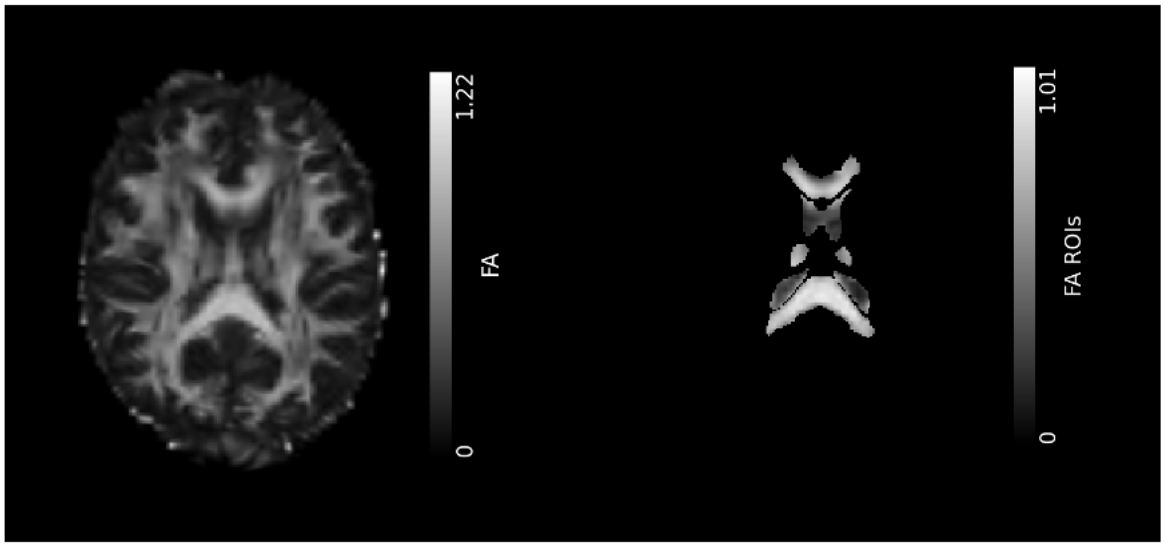

Figure 8.15: (A) Quantitative map of the FA of the whole brain aligned to MNI152 standard space, (B) quantitative map of FA for each selected ROI, i.e. Corpus Callosum, Thalamus and Ventricles.

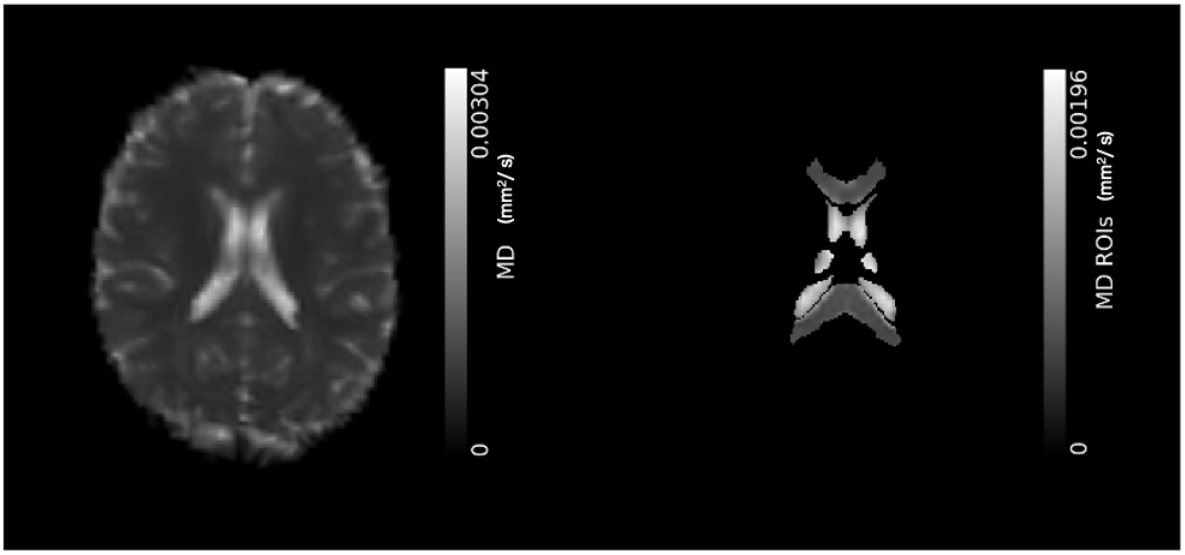

Figure 8.16: (A) Quantitative map of the MD of the whole brain aligned to MNI152 standard space, (B) quantitative map of MD for each selected ROI, i.e. Corpus Callosum, Thalamus and Ventricles.

scans acquired on the Siemens Prisma. However, the values obtained are similar between the two scanners hence suggesting a robust fit for the Bingham-NODDI model across scanners.

The considerations applied to the quantitative maps derived from the diffusion brain data collected on the GE Premier remain applicable to those generated from the Siemens Prisma. Particularly noteworthy is the observation of elevated ODI index values within regions of the Corpus Callosum and areas corresponding to the anticipated histological presence of white matter, shown in Figure 8.18. The β-fraction values in Figure 8.19 exhibit notable variability across various Regions of Interest (ROIs), primarily attributed to the intricate and diverse nature of neurite structures within the brain. This diversity

Table 8.4: Bingham-NODDI metrics results of a set of two *in-vivo* acquisitions on the Siemens Prisma of a healthy volunteer to assess intra-site repeatability.

Bingham-NODDI model							
		ODI	**β-fraction**	**Tissue v. f.**	**Intra-neurite v. f.**	**R^2**	**MSE**
Genu CC	SCAN 1	0.080 ± 0.069	0.586 ± 0.219	0.85 ± 0.14	0.61 ± 0.11	0.981 ± 0.009	0.0013 ± 0.0007
	SCAN 2	0.078 ± 0.065	0.592 ± 0.202	0.86 ± 0.13	0.61 ± 0.11	0.982 ± 0.009	0.0012 ± 0.0007
	CV	1.44 %	0.54%	0.53%	0.30%	0.02%	1.1%
Splenium CC	SCAN 1	0.061 ± 0.062	0.595 ± 0.194	0.85 ± 0.12	0.69 ± 0.11	0.980 ± 0.011	0.0016 ± 0.0013
	SCAN 2	0.060 ± 0.059	0.607 ± 0.202	0.85 ± 0.13	0.69 ± 0.12	0.981 ± 0.010	0.0014 ± 0.0010
	CV	1.53%	1.00%	0.48%	0.21%	0.07%	4.7%
Anterior limb IC	SCAN 1	0.174 ± 0.095	0.551 ± 0.184	0.94 ± 0.05	0.59 ± 0.09	0.974 ± 0.013	0.0015 ± 0.0007
	SCAN 2	0.177 ± 0.091	0.532 ± 0.182	0.95 ± 0.06	0.59 ± 0.09	0.973 ± 0.020	0.0016 ± 0.0016
	CV	0.87%	1.72%	0.3%	0.46%	0.04%	2.6%
Posterior limb IC	SCAN 1	0.100 ± 0.044	0.541 ± 0.235	0.91 ± 0.03	0.69 ± 0.06	0.977 ± 0.011	0.0014 ± 0.0007
	SCAN 2	0.099 ± 0.050	0.558 ± 0.213	0.91 ± 0.04	0.68 ± 0.06	0.976 ± 0.013	0.0015 ± 0.0008
	CV	0.46%	1.56%	0.27%	0.47%	0.04%	2.1%
Thalamus	SCAN 1	0.185 ± 0.076	0.627 ± 0.203	0.95 ± 0.08	0.46 ± 0.06	0.976 ± 0.008	0.0010 ± 0.0006
	SCAN 2	0.179 ± 0.074	0.641 ± 0.194	0.94 ± 0.10	0.47 ± 0.06	0.984 ± 0.007	0.0010 ± 0.0004
	CV	1.70%	1.12%	0.33%	0.09%	0.06%	3.83%
Caudate	SCAN 1	0.420 ± 0.127	0.581 ± 0.187	0.88 ± 0.15	0.47 ± 0.07	0.976 ± 0.016	0.0016 ± 0.0011
	SCAN 2	0.418 ± 0.120	0.581 ± 0.191	0.90 ± 0.14	0.47 ± 0.07	0.972 ± 0.020	0.0018 ± 0.0014
	CV	0.22%	0.01%	0.75%	0.39%	0.16%	6.76%
Putamen	SCAN 1	0.444 ± 0.137	0.540 ± 0.170	0.989 ± 0.003	0.49 ± 0.02	0.980 ± 0.004	0.0011 ± 0.0002
	SCAN 2	0.451 ± 0.136	0.536 ± 0.166	0.989 ± 0.004	0.49 ± 0.02	0.980 ± 0.004	0.0011 ± 0.0002
	CV	0.77%	0.31%	0.002%	0.02%	0.002%	0.13%

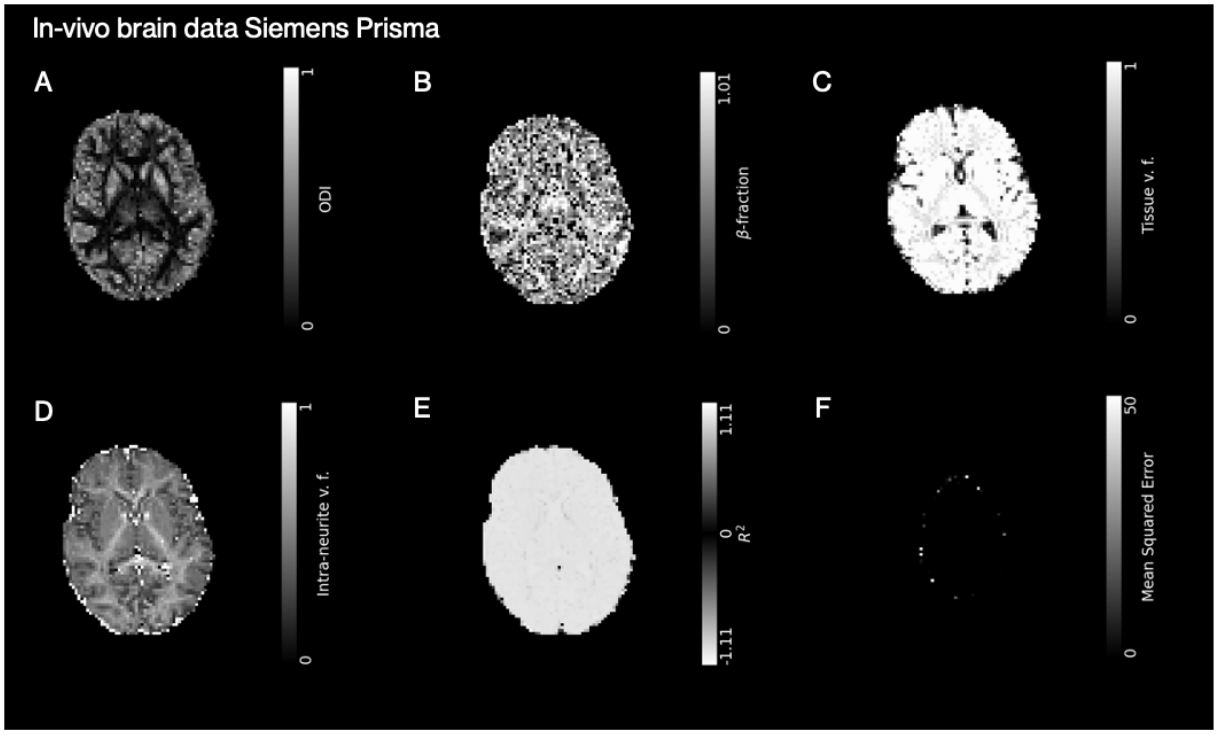

Figure 8.17: Quantitative maps of the metrics obtained fitting the diffusion brain data acquired on the Siemens Prisma to the Bingham-NODDI model: (A) The ODI index, (B) The β-fraction, (C) The tissue volume fraction, (D) The intra-neurite volume fraction, (E) The R^2 coefficient, (F) The Mean Squared Error (MSE) coefficient.

poses challenges in accurately determining a precise value representing the proportion of volume occupied by neurites relative to the total voxel volume. The Tissue volume fraction index in Figure 8.20 has values that are close to 1 in the brain regions characterized by the presence of brain tissue whilst it is close to zero in the ventricles region, mainly composed by the CSF. Similar consideration can be done for the intra-neurite volume fraction,

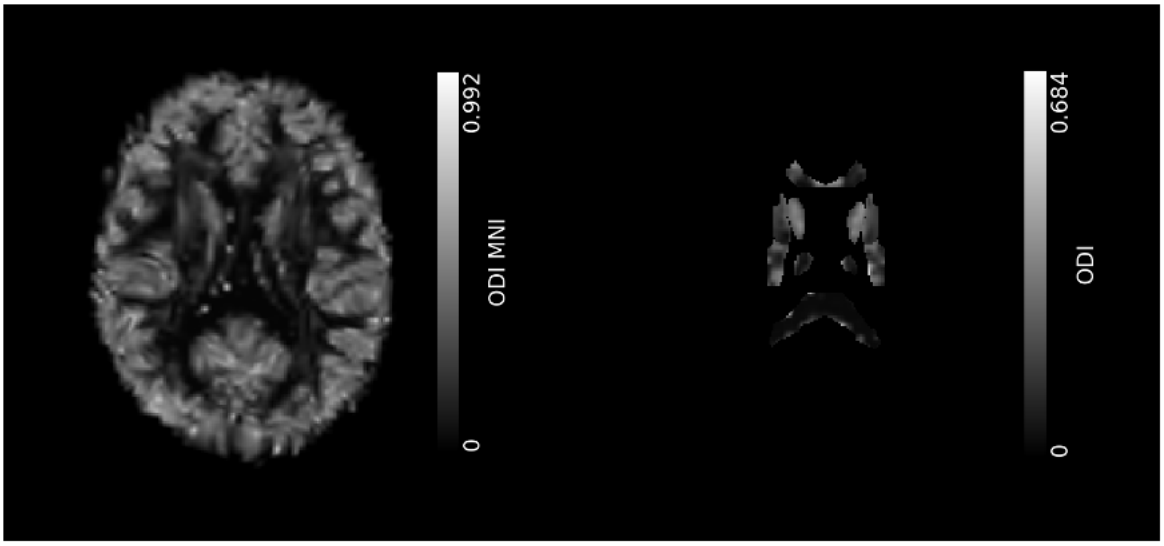

Figure 8.18: Quantitative maps of the ODI index obtained fitting the diffusion brain data acquired on the Siemens Prisma to the Bingham-NODDI model: on the left, the ODI map fitted to the MNI152 space: on the right the ODI index for each selected ROI, i.e. Genu and Splenium of Corpus Callosum, Anterior and Posterior Limbs of Internal Capsule, Thalamus, Putamen and Caudate.

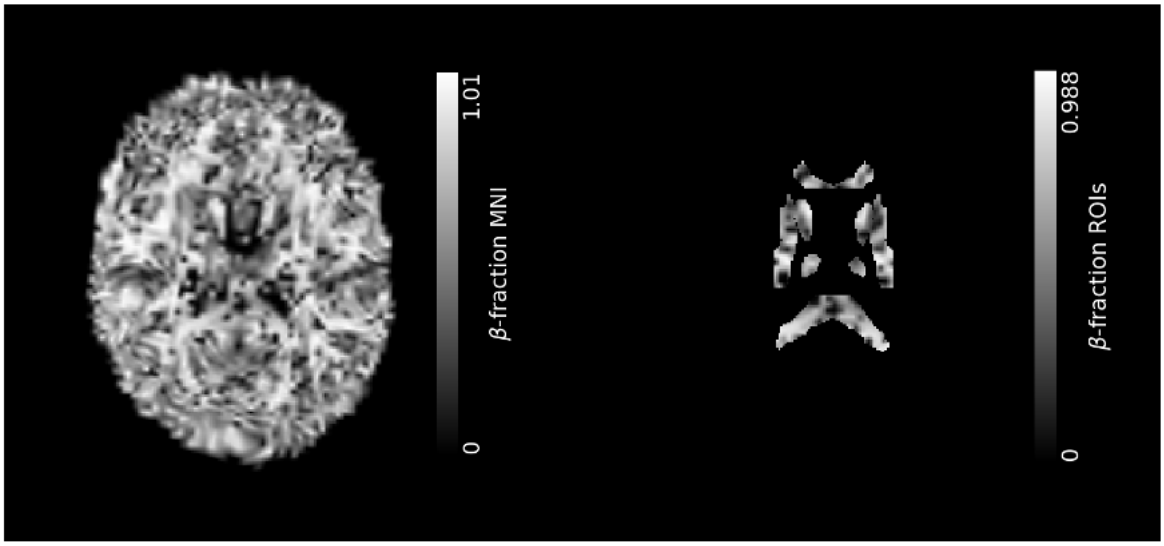

Figure 8.19: Quantitative maps of the β-fraction index obtained fitting the diffusion brain data acquired on the Siemens Prisma to the Bingham-NODDI model: on the left, the β-fraction map fitted to the MNI152 space: on the right the β-fraction index for each selected ROI, i.e. Genu and Splenium of Corpus Callosum, Anterior and Posterior Limbs of Internal Capsule, Thalamus, Putamen and Caudate.

showing lower values in the Thalamus, Caudate and Putamen regions hence suggesting a lower density of axons and dendrites. Finally, the Extra-cellular volume fraction has values close to one in the Ventricles region, thus marking the dominant presence of non-tissue in this region of the brain.
The Mean Squared Error assumes low values. Furthermore, voxels with higher values are randomly located in the map not showing any particular brain structure hence showing

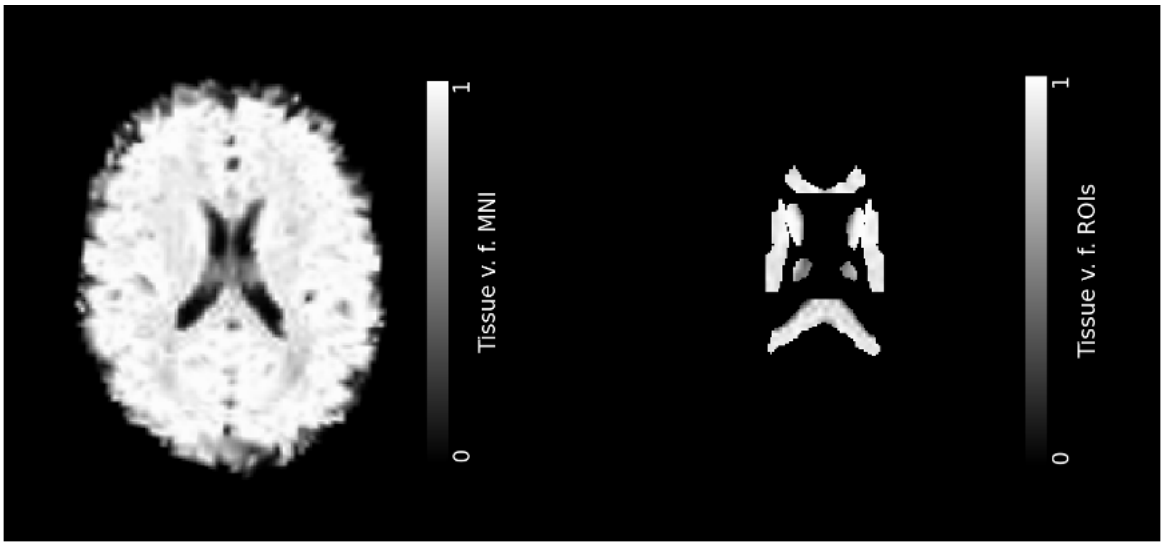

Figure 8.20: Quantitative maps of the Tissue Volume Fraction index obtained fitting the diffusion brain data acquired on the Siemens Prisma to the Bingham-NODDI model: on the left, the Tissue Volume Fraction map fitted to the MNI152 space: on the right the Tissue Volume Fraction index for each selected ROI, i.e. Genu and Splenium of Corpus Callosum, Anterior and Posterior Limbs of Internal Capsule, Thalamus, Putamen and Caudate.

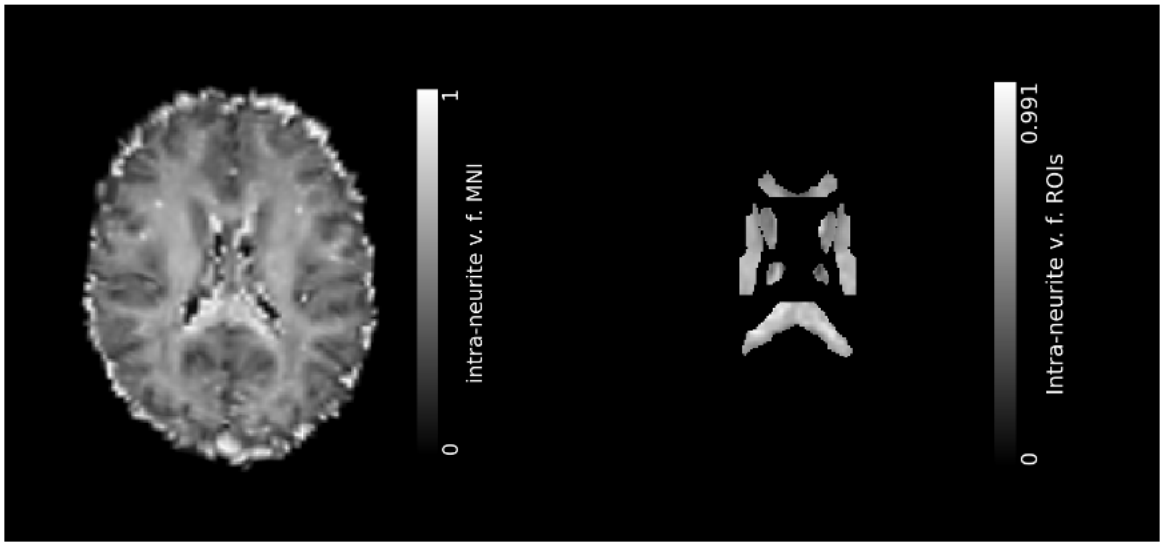

Figure 8.21: Quantitative maps of the Intra-neurite Volume Fraction index obtained fitting the diffusion brain data acquired on the Siemens Prisma to the Bingham-NODDI model: on the left, the Intra-neurite Volume Fraction map fitted to the MNI152 space: on the right the Intra-neurite Volume Fraction index for each selected ROI, i.e. Genu and Splenium of Corpus Callosum, Anterior and Posterior Limbs of Internal Capsule, Thalamus, Putamen and Caudate.

the goodness of fit.

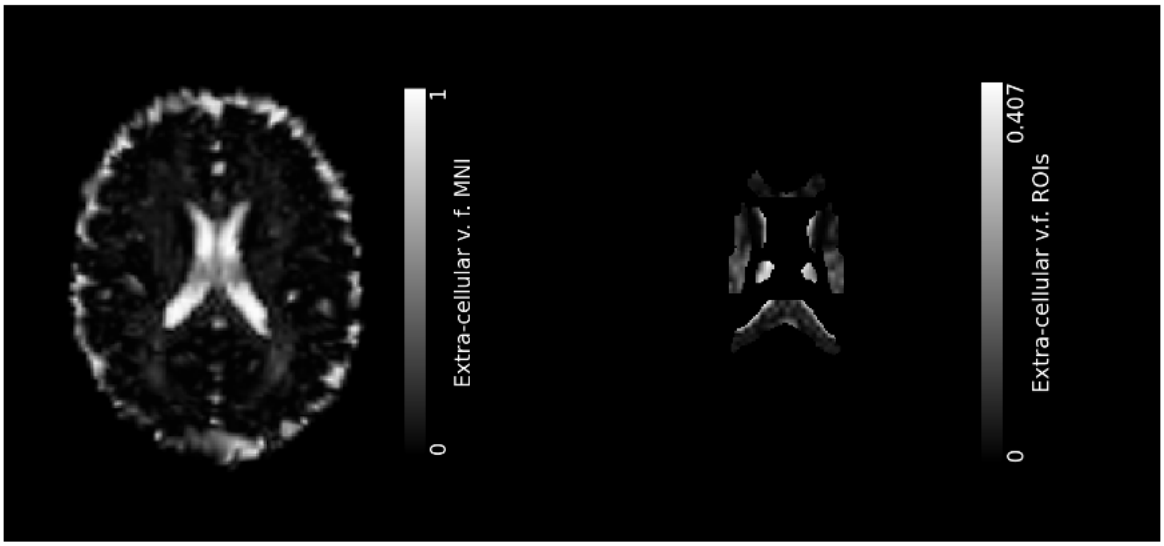

Figure 8.22: Quantitative maps of the Extra-cellular Volume Fraction index obtained fitting the diffusion brain data acquired on the Siemens Prisma to the Bingham-NODDI model: on the left, the Extra-cellular Volume Fraction map fitted to the MNI152 space: on the right the Extra-cellular Volume Fraction index for each selected ROI, i.e. Genu and Splenium of Corpus Callosum, Anterior and Posterior Limbs of Internal Capsule, Thalamus, Putamen and Caudate.

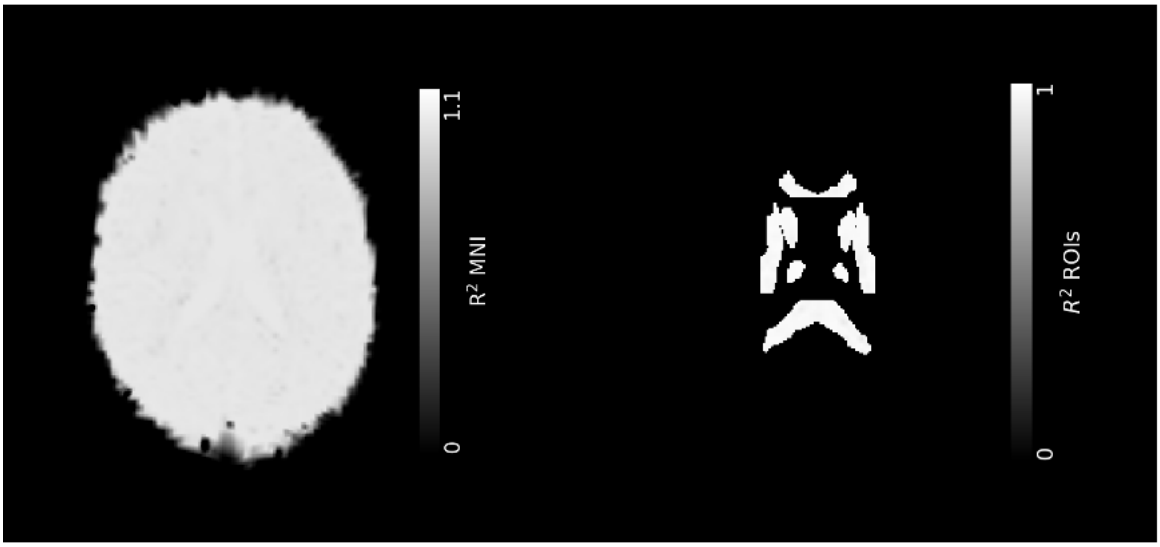

Figure 8.23: Quantitative maps of the R^2 index obtained fitting the diffusion brain data acquired on the Siemens Prisma to the Bingham-NODDI model: on the left, the R^2 map fitted to the MNI152 space: on the right the R^2 index for each selected ROI, i.e. Genu and Splenium of Corpus Callosum, Anterior and Posterior Limbs of Internal Capsule, Thalamus, Putamen and Caudate.

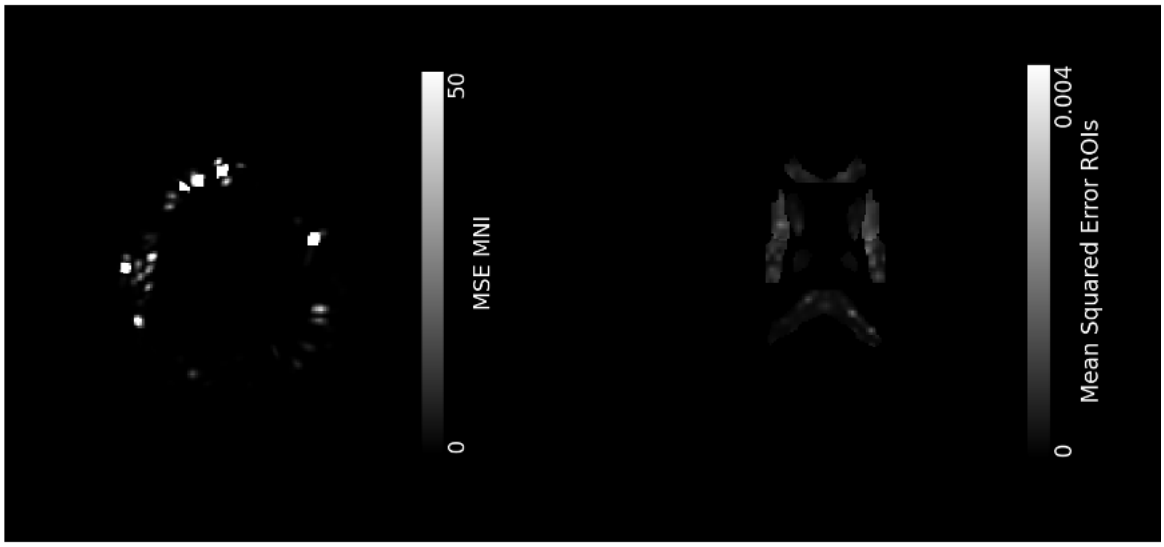

Figure 8.24: Quantitative maps of the Mean Squared Error index obtained fitting the diffusion brain data acquired on the Siemens Prisma to the Bingham-NODDI model: on the left, the Mean Squared Error map fitted to the MNI152 space: on the right the Mean Squared Error index for each selected ROI, i.e. Genu and Splenium of Corpus Callosum, Anterior and Posterior Limbs of Internal Capsule, Thalamus, Putamen and Caudate.

8.3 Comparisons

The *in-vivo* data investigation proceeded with the acquisition of diffusion brain data of a second healthy volunteer. First, the volunteer was scanned on the GE Premier located at the OCMR, then on the Siemens Prisma with a monopolar acquisition protocol. On each scanner, one scan was performed, in order to visualize comparisons with the scans acquired on the first healthy volunteer and to assess the inter-site repeatability of results of the tensor model of the Bingham-NODDI model. Having assessed intra-site consistency of results, for each set of acquisitions performed on the first healthy volunteer, the first scan was chosen to show results.
It is necessary to highlight that the processing of the diffusion brain images of the second healthy volunteer acquired on the Siemens Prisma showed distortions that the FSL EDDY tool was not able to properly correct hence creating inaccurate alignments of the quantitative map of the fit with the MNI152 standard space. For this reason, images were corrected by exploiting distortion correction without reverse phase-encoding scans or field maps, as explained in the paper [56].

This tool aims to enable susceptibility distortion correction with historical and/or limited datasets using an "undistorted" b = 0 image that matches the geometry of structural T1-weighted images and also matches the contrast from the diffusion images. This "undistorted" image is used in the standard work pipeline and tells the algorithm that this synthetic image has infinite bandwidth. The resulting topup outputs were then used to perform eddy correction and to fit the data to the tensor and NODDI models.

Comparisons of the metrics results obtained fitting the tensor model to each healthy volunteer diffusion brain data are shown in Table 8.5.

Table 8.5: Tensor model metrics results for the *in-vivo* diffusion brain data acquisitions performed on the GE Premier located and on the Siemens Prisma. Results are extracted from three region of interests: Corpus Callosum for WM, Thalamus for GM and Ventricles for CSF.

TENSOR model				
			FA	**MD** ($\cdot 10^{-3} mm^2/s$)
GE PREMIER	*Corpus Callosum*	Healthy Volunteer 1	0.577 ± 0.196	0.661 ± 0.145
		Healthy Volunteer 2	0.615 ± 0.180	0.636 ± 0.133
	Thalamus	Healthy Volunteer 1	0.307 ± 0.078	0.724 ± 0.177
		Healthy Volunteer 2	0.316 ± 0.067	0.629 ± 0.122
	Ventricles	Healthy Volunteer 1	0.346 ± 0.186	1.522 ± 0.370
		Healthy Volunteer 2	0.234 ± 0.108	1.812 ± 0.285
SIEMENS PRISMA	*Corpus Callosum*	Healthy Volunteer 1	0.656 ± 0.170	0.650 ± 0.146
		Healthy Volunteer 2	0.495 ± 0.297	0.515 ± 0.260
	Thalamus	Healthy Volunteer 1	0.331 ± 0.078	0.657 ± 0.117
		Healthy Volunteer 2	0.272 ± 0.135	0.543 ± 0.254
	Ventricles	Healthy Volunteer 1	0.274 ± 0.126	1.741 ± 0.290
		Healthy Volunteer 2	0.140 ± 0.128	1.455 ± 1.0

The FA and MD outcomes, derived from the analysis of *in-vivo* brain data presented in Table 8.5, juxtapose the results of the initial scans obtained from both the GE Premier and Siemens Prisma scanners of the first healthy volunteer with those acquired from both MRI scanners in the case of the second healthy volunteer.
Results obtained on the Siemens Prisma tend to show higher FA values in the Corpus Callosum region compared to those obtained on the GE Premier. Both scanners exhibit

relatively similar FA and MD values for the Thalamus in both healthy volunteers whilst FA values are generally lower in Siemens Prisma. Results obtained across scanners for each single volunteer are similar within the margin of errors. However, MD results extracted from the ROIs designed on the ventricles region show variability. This may be due to the different alignment processing performed on the second volunteer Siemens diffusion data, as it has been corrected from distortions differently hence showing slight differences.

Figure 8.25 displays the quantitative maps of FA obtained fitting the diffusion brain data acquired on the two 3T scanners to the tensor model. The quantitative maps were aligned to the MNI152 standard space to better visualize differences.

In addition to the structural distinctions among the brains, the FA maps exhibit comparable characteristics, as FA tends to attain higher values in white matter regions. This is indicative of the preferential diffusion direction of water molecules along axons. Figure 8.26 shows MD quantitative maps. Notably, mean diffusivity assumes higher values in the ventricles, consistent with the unrestricted diffusion properties of CSF located in this brain region.

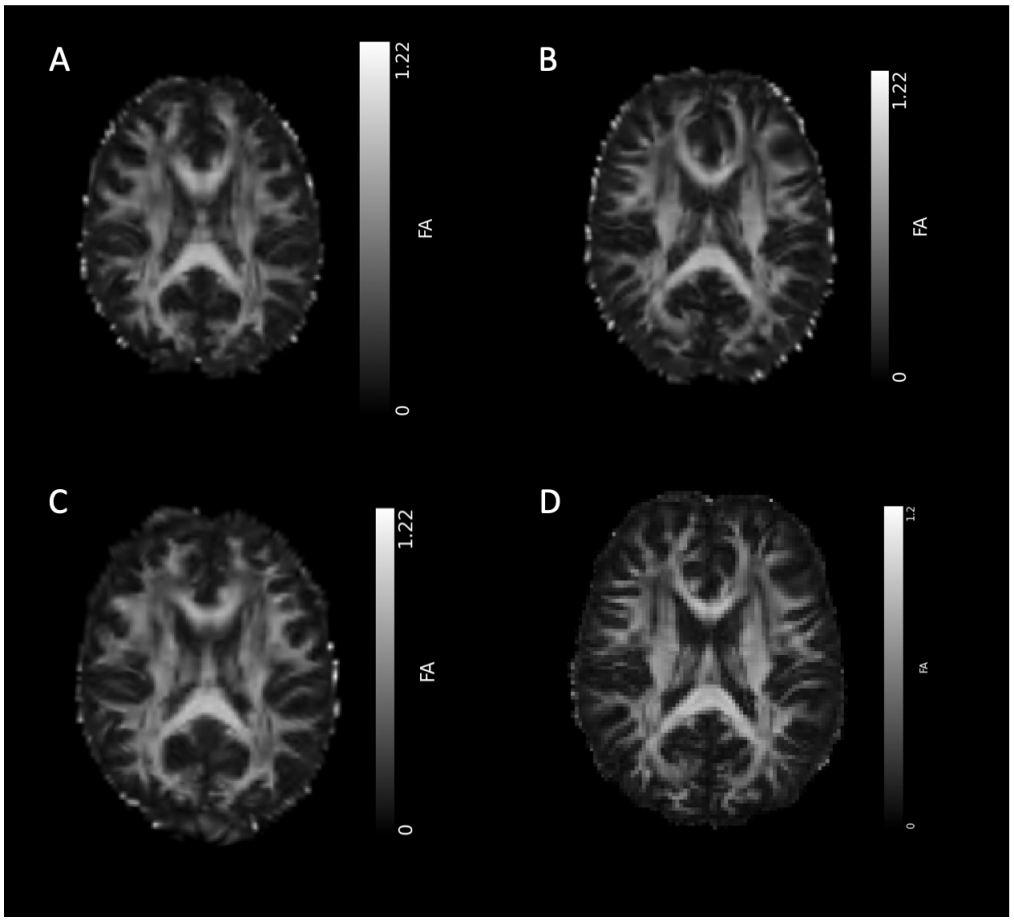

Figure 8.25: FA quantitative maps obtained fitting the diffusion brain data to the tensor model. First row shows GE Premier acquisitions: (A) FA map of the first scan of Healthy Volunteer 1, (B) FA map of Healthy Volunteer 2; second row shows Siemens Prisma Monopolar acquisitions: (C) FA map of the first scan of Healthy Volunteer 1, (D) FA map of Healthy Volunteer 2.

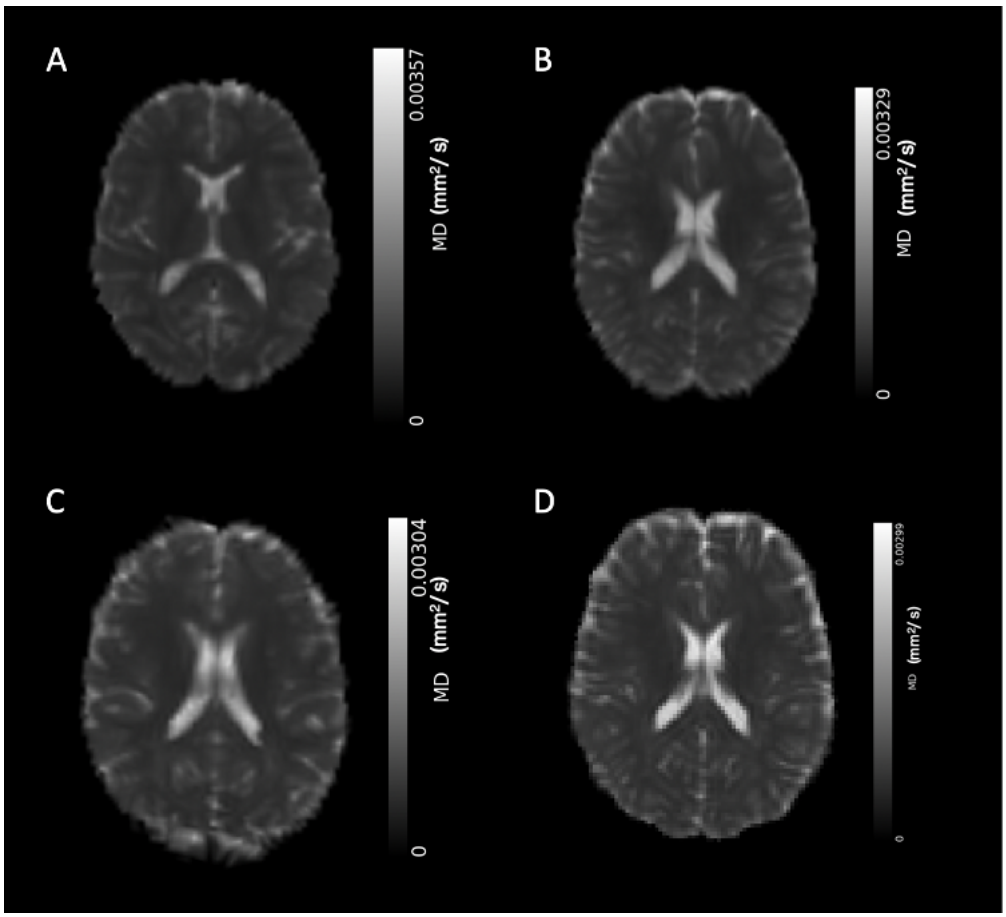

Figure 8.26: MD quantitative maps obtained fitting the diffusion brain data to the tensor model. First row shows GE Premier acquisitions: (A) MD map of the first scan of Healthy Volunteer 1, (B) MD map of Healthy Volunteer 2; second row shows Siemens Prisma Monopolar acquisitions: (C) MD map of the first scan of Healthy Volunteer 1, (D) MD map of Healthy Volunteer 2.

Table 8.6: Bingham-NODDI model metrics results of the two healthy volunteers for each selected region of interest (ROI) on the 3T GE Premier and Siemens Prisma.

BINGHAM-NODDI model								
			ODI	**beta**	**Tissue v. f.**	**Intra-neruite v. f.**	**R^2**	**MSE**
GE PREMIER	*Genu CC*	Healthy Volunteer 1	0.103 ± 0.089	0.582 ± 0.202	0.82 ± 0.17	0.56 ± 0.11	0.980 ± 0.008	0.0013 ± 0.0006
		Healthy Volunteer 2	0.088 ± 0.076	0.499 ± 0.232	0.89 ± 0.12	0.56 ± 0.09	0.971 ± 0.009	0.0020 ± 0.0007
	Splenium CC	Healthy Volunteer 1	0.079 ± 0.077	0.583 ± 0.200	0.86 ± 0.10	0.64 ± 0.11	0.979 ± 0.006	0.0014 ± 0.0005
		Healthy Volunteer 2	0.069 ± 0.075	0.614 ± 0.195	0.86 ± 0.13	0.63 ± 0.11	0.963 ± 0.013	0.0027 ± 0.0014
	Anterior limb IC	Healthy Volunteer 1	0.193 ± 0.099	0.491 ± 0.183	0.939 ± 0.051	0.549 ± 0.073	0.976 ± 0.008	0.0014 ± 0.0005
		Healthy Volunteer 2	0.150 ± 0.082	0.530 ± 0.212	0.964 ± 0.028	0.577 ± 0.070	0.959 ± 0.017	0.0025 ± 0.0012
	Posterior limb IC	Healthy Volunteer 1	0.119 ± 0.041	0.521 ± 0.233	0.881 ± 0.041	0.65 ± 0.06	0.977 ± 0.008	0.0013 ± 0.005
		Healthy Volunteer 2	0.115 ± 0.051	0.458 ± 0.232	0.937 ± 0.041	0.66 ± 0.07	0.956 ± 0.012	0.0027 ± 0.0008
	Thalamus	Healthy Volunteer 1	0.181 ± 0.073	0.622 ± 0.206	0.921 ± 0.131	0.424 ± 0.061	0.981 ± 0.005	0.0011 ± 0.0003
		Healthy Volunteer 2	0.189 ± 0.058	0.611 ± 0.202	0.950 ± 0.096	0.485 ± 0.058	0.958 ± 0.011	0.0025 ± 0.0007
	Caudate	Healthy Volunteer 1	0.423 ± 0.147	0.524 ± 0.173	0.834 ± 0.201	0.446 ± 0.076	0.981 ± 0.012	0.0012 ± 0.0007
		Healthy Volunteer 2	0.332 ± 0.108	0.565 ± 0.170	0.872 ± 0.186	0.445 ± 0.080	0.973 ± 0.012	0.0016 ± 0.0007
	Putamen	Healthy Volunteer 1	0.417 ± 0.136	0.542 ± 0.178	0.986 ± 0.010	0.460 ± 0.031	0.979 ± 0.003	0.0012 ± 0.0002
		Healthy Volunteer 2	0.374 ± 0.133	0.558 ± 0.176	0.987 ± 0.009	0.522 ± 0.041	0.958 ± 0.0170	0.0025 ± 0.0010
SIEMENS PRISMA	*Genu CC*	Healthy Volunteer 1	0.080 ± 0.069	0.586 ± 0.219	0.85 ± 0.14	0.61 ± 0.11	0.981 ± 0.009	0.0013 ± 0.0007
		Healthy Volunteer 2	0.076 ± 0.074	0.507 ±0.264	0.87 ± 0.16	0.55 ± 0.12	0.956 ± 0.123	0.0014 ± 0.0011
	Splenium CC	Healthy Volunteer 1	0.061 ± 0.062	0.595 ± 0.194	0.85 ± 0.12	0.69 ± 0.11	0.980 ± 0.011	0.0016 ± 0.0013
		Healthy Volunteer 2	0.076 ± 0.09	0.620 ± 0.217	0.90 ± 0.09	0.62 ± 0.13	0.974 ± 0.021	0.0023 ± 0.0020
	Anterior limb IC	Healthy Volunteer 1	0.174 ± 0.095	0.551 ± 0.184	0.94 ± 0.05	0.59 ± 0.09	0.974 ± 0.013	0.0015 ± 0.0007
		Healthy Volunteer 2	0.116 ± 0.075	0.577 ± 0.231	0.95 ± 0.06	0.57 ± 0.09	0.971 ± 0.047	0.0015 ± 0.0007
	Posterior limb IC	Healthy Volunteer 1	0.100 ± 0.044	0.541 ± 0.235	0.91 ± 0.03	0.69 ± 0.06	0.977 ± 0.011	0.0014 ± 0.0007
		Healthy Volunteer 2	0.089± 0.052	0.556 ± 0.251	0.92 ± 0.04	0.65 ± 0.07	0.976 ± 0.012	0.0015 ± 0.0008
	Thalamus	Healthy Volunteer 1	0.185 ± 0.076	0.627 ± 0.203	0.95 ± 0.08	0.46 ± 0.06	0.976 ± 0.008	0.0010 ± 0.0006
		Healthy Volunteer 2	0.189 ± 0.066	0.616 ± 0.223	0.96 ± 0.09	0.47 ± 0.07	0.973 ± 0.013	0.0016 ± 0.0009
	Caudate	Healthy Volunteer 1	0.420 ± 0.127	0.581 ± 0.187	0.88 ± 0.15	0.47 ± 0.07	0.976 ± 0.016	0.0016 ± 0.0011
		Healthy Volunteer 2	0.356 ± 0.115	0.571 ± 0.204	0.93 ± 0.14	0.45 ± 0.10	0.956 ± 0.094	0.0018 ± 0.0015
	Putamen	Healthy Volunteer 1	0.444 ± 0.137	0.540 ± 0.170	0.989 ± 0.003	0.49 ± 0.02	0.980 ± 0.004	0.0011 ± 0.0002
		Healthy Volunteer 2	0.372 ± 0.159	0.514 ± 0.206	0.94 ± 0.17	0.46 ± 0.09	0.930 ± 0.168	0.0014 ± 0.0004

Comparisons of results obtained for Healthy Volunteer 1 on paired scanners show similarity hence suggesting the model's consistency. In particular, the ODI values obtained on the Siemens Prisma for Genu CC are slightly lower compared to the GE premier but acceptable within the margin of errors. Tissue and Intra-neurite volume fraction results are consistent across MRI scanners. The ODI values obtained by extracting from the Splenium region are affected by noise on both scanners.
The volume fraction within neurites shows elevated values in the Genu and Splenium regions of the Corpus Callosum, as well as in the Anterior and Posterior limbs of the Internal Capsules, in contrast to the results derived from the Putamen, Caudate, and Thalamus. This indicates a greater concentration of axons and dendrites in these former regions, aligning with histological expectations, given that the latter regions are primarily distinguished by the prevalence of gray matter. Also, results extracted from Genu, Splenium and Anterior limb of IC show slightly higher values on the Siemens Prisma compared to those obtained on the GE premier although consistent within the margin of errors whilst results from the Posterior limb of the IC are comparable between scanners.

Overall, despite being different scanners, there is consistency in the estimated metrics for intra-neurite volume fraction across most brain regions and for both healthy volunteers. There is some variability between healthy volunteers, with different individuals showing slightly different intra-neurite volume fraction values. This is expected due to natural anatomical variations among individuals.

The Bingham-NODDI model appears to provide robust and consistent estimations of the metrics across different brain regions and volunteers on both scanners.

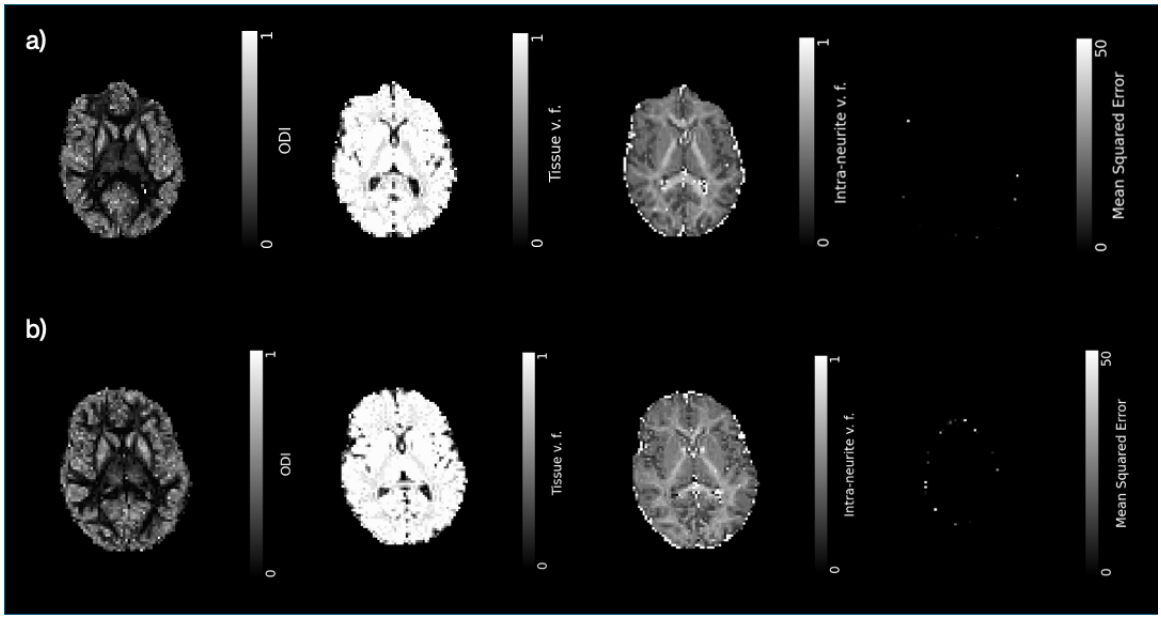

Figure 8.27: Bingham-NODDI quantitative maps obtained fitting *in-vivo* brain data acquired on a) GE Premier, b) Siemens Prisma with a monopolar acquisition protocol. Images show the ODI index, the Tissue Volume Fraction index, the Intra-neurite Volume Fraction and the Mean Squared Error.

Table 8.7: AMICO-NODDI model results fitting the diffusion brain data acquired on the GE Premier and on the Siemens Prisma for both healthy volunteers.

AMICO-NODDI model										
			ODI	**ISOVF**	**ICVF**				**ODI**	**ISOVF**	**ICVF**
GE PREMIER	*Genu CC*	Healthy Volunteer 1	0.170 ± 0.14	0.18 ± 0.18	0.54 ± 0.12						
		Healthy Volunteer 2	0.130 ± 0.10	0.11 ± 0.12	0.55 ± 0.10						
	Splenium CC	Healthy Volunteer 1	0.123 ± 0.098	0.14 ± 0.10	0.64 ± 0.11		*Thalamus*	Healthy Volunteer 1	0.306 ± 0.099	0.110 ± 0.160	0.40 ± 0.08
		Healthy Volunteer 2	0.118 ± 0.106	0.139 ± 0.141	0.62 ± 0.11			Healthy Volunteer 2	0.298 ± 0.063	0.093 ± 0.133	0.45 ± 0.07
	Anterior limb IC	Healthy Volunteer 1	0.236 ± 0.120	0.059 ± 0.050	0.54 ± 0.09		*Caudate*	Healthy Volunteer 1	0.553 ± 0.144	0.225 ± 0.222	0.341 ± 0.067
		Healthy Volunteer 2	0.187 ± 0.107	0.056 ± 0.04	0.57 ± 0.08			Healthy Volunteer 2	0.459 ± 0.104	0.196 ± 0.217	0.34 ± 0.07
	Posterior limb IC	Healthy Volunteer 1	0.189 ± 0.071	0.121 ± 0.040	0.67 ± 0.07		*Putamen*	Healthy Volunteer 1	0.506 ± 0.143	0.012 ± 0.016	0.42 ± 0.06
		Healthy Volunteer 2	0.149 ± 0.067	0.056 ± 0.043	0.67 ± 0.07			Healthy Volunteer 2	0.455 ± 0.147	0.012 ± 0.018	0.46 ± 0.06
SIEMENS PRISMA	*Genu CC*	Healthy Volunteer 1	0.208 ± 0.128	0.143 ± 0.139	0.63 ± 0.17						
		Healthy Volunteer 2	0.113 ± 0.099	0.109 ± 0.115	0.55 ± 0.13						
	Splenium CC	Healthy Volunteer 1	0.158 ± 0.112	0.109 ± 0.124	0.55 ± 0.20		*Thalamus*	Healthy Volunteer 1	0.285 ± 0.105	0.072 ± 0.096	0.48 ± 0.18
		Healthy Volunteer 2	0.118 ± 0.111	0.099 ± 0.092	0.61 ± 0.12			Healthy Volunteer 2	0.297 ± 0.070	0.084 ± 0.133	0.43 ± 0.07
	Anterior limb IC	Healthy Volunteer 1	0.373 ± 0.144	0.010 ± 0.019	0.52 ± 0.10		*Caudate*	Healthy Volunteer 1	0.406 ± 0.126	0.113 ± 0.135	0.47 ± 0.14
		Healthy Volunteer 2	0.146 ± 0.097	0.054 ± 0.05	0.57 ± 0.10			Healthy Volunteer 2	0.436 ± 0.112	0.112 ± 0.157	0.341 ± 0.071
	Posterior limb IC	Healthy Volunteer 1	0.246 ± 0.109	0.053 ± 0.063	0.58 ± 0.15		*Putamen*	Healthy volunteer 1	0.370 ± 0.137	0.033 ± 0.051	0.41 ± 0.06
		Healthy Volunteer 2	0.127 ± 0.061	0.067 ± 0.039	0.65 ± 0.07			Healthy Volunteer 2	0.447 ± 0.170	0.001 ± 0.015	0.41 ± 0.09

The same diffusion-weighted MRI data was also fitted to the linear formulation of the NODDI model which used the Watson distribution to model the neurite dispersion, instead of the Bingham distribution. The data processing pipeline is the same as for fitting the Bingham-NODDI model and it was repeated for each scan separately, results are shown in Table 8.7.

Regarding results obtained on both Healthy Volunteers, values are slightly different between scanners but consistent within the margin of errors, with ODI and ICVF values being slightly higher for Siemens Prisma. The ISOVF values are less consistent but indicate potential variations in isotropic diffusion characteristics. Healthy Volunteer 1 generally exhibits more noticeable differences between scanners compared to Healthy Volunteer 2.

The quantitative maps obtained from the AMICO-NODDI fit are shown in Figure 8.28, Figure 8.29, and in Figure 8.30.

The ODI map, shown in Figure 8.28, represents the orientation dispersion index obtained on (A) the GE Premier and (B) Siemens Prisma. In particular, the regions where CSF is located are characterized by higher values, indicating the absence of coherent neurite structure for CSf.
The ICVF maps, in Figure 8.30, show the volume fraction occupied by neurites in each voxel and looks similar to the intra-neurite volume fractions maps in Figure 8.27. In this map, however, the ventricles have values close to zero, showing the absence of cells in this region, due to the CSF signal not being suppressed in the AMICO-NODDI mathematical formulation.
The ISOVF maps, in Figure 8.29, define the fraction of voxels occupied by non-tissue in the brain, clearly showing higher values in the region where CSF is located, mainly the ventricles, the surface of the brain and down the subarachnoid space.

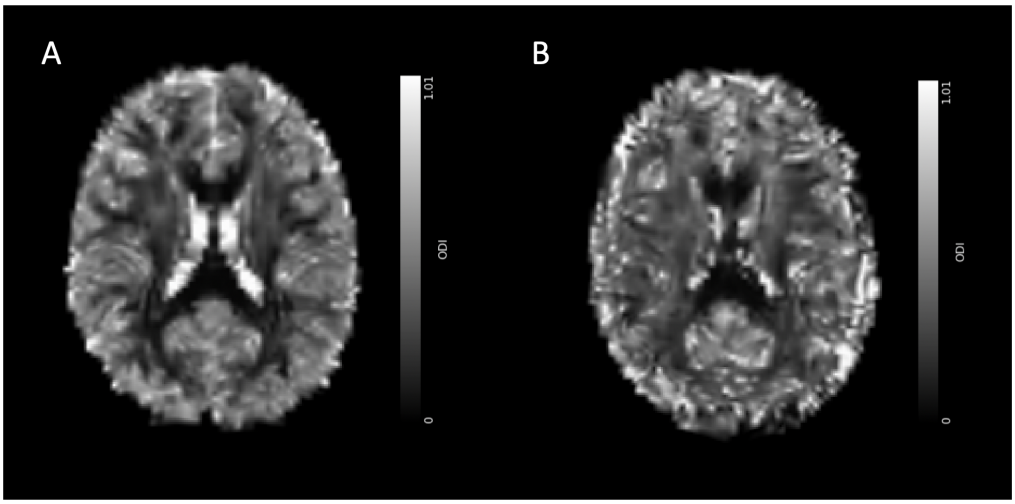

Figure 8.28: Amico-NODDI model quantitative maps of the results fitting *in-vivo* data. (A) The ODI index map obtained fitting diffusion brain data of the first scan of Healthy Volunteer 1 on the GE Premier; (B) The ODI index map obtained fitting diffusion brain data of the first scan of Healthy Volunteer 1 on the Siemens Prisma with a monopolar acquisition protocol.

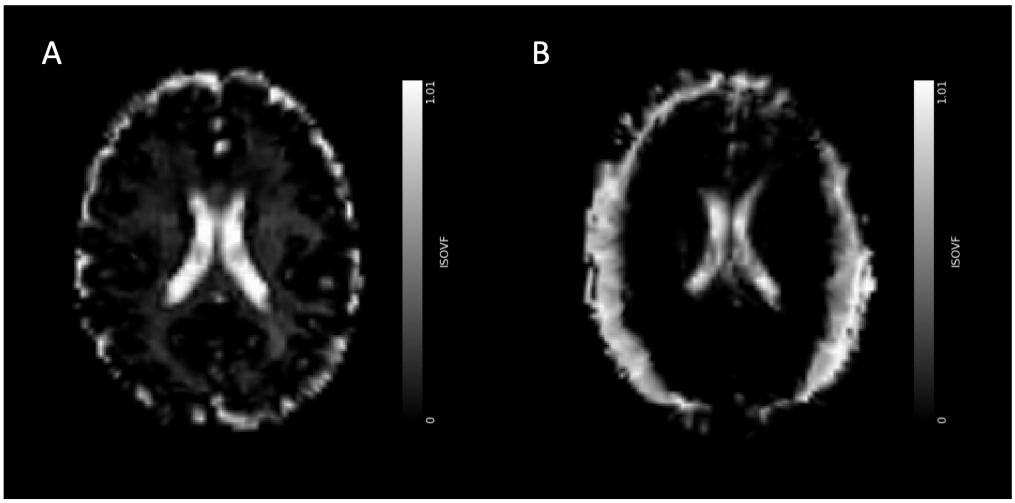

Figure 8.29: Amico-NODDI model quantitative maps of the results fitting *in-vivo* data. (A) The Isotropic Volume Fraction (ISOVF) index map obtained fitting diffusion brain data of the first scan of Healthy Volunteer 1 on the GE Premier; (B) The ISOVF index map obtained fitting diffusion brain data of the first scan of Healthy Volunteer 1 on the Siemens Prisma with a monopolar acquisition protocol.

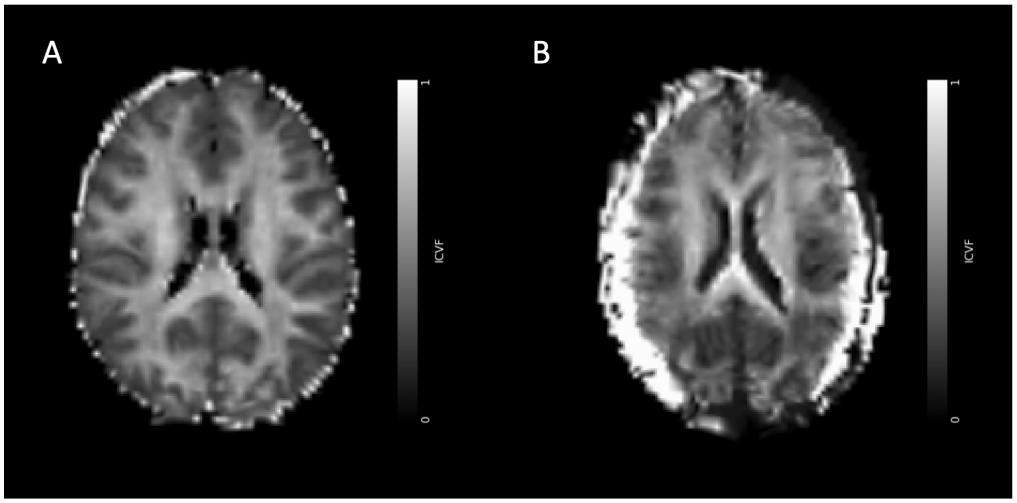

Figure 8.30: Amico-NODDI model quantitative maps of the results fitting *in-vivo* data. (A) The Intra-cellular Volume Fraction (ICVF) index map obtained fitting diffusion brain data of the first scan of Healthy Volunteer 1 on the GE Premier; (B) The ICVF index map obtained fitting diffusion brain data of the first scan of Healthy Volunteer 1 on the Siemens Prisma with a monopolar acquisition protocol.

Conclusions

This thesis is the result of my research study carried out at the Oxford Centre for Clinical Magnetic Resonance (OCMR) - University of Oxford. The main objective of this study was to assess the consistency and repeatability of the Bingham-NODDI model results across different MRI scanner systems, a model used to detect microstructural changes in the brain by estimating the orientation distribution function of neurites in the brain. In particular, this model employs the Bingham distribution to model the neurite dispersion about a dominant orientation, improving the original formulation of the NODDI model, only able to capture the isotropic dispersion of neurites. In this way, the Bingham-NODDI model offers a unique perspective on microstructural changes in the brain by being able to properly capture more complex configurations of neurites in the brain, such as bending or fanning fibers of white matte. The tensor model and the AMICO-NODDI model were also used as the first is able to provide insights into the diffusion properties of the brain, and the latter is a linear formulation of the NODDI model which requires less time to fit the diffusion data compared to its original formulation.

To assess the repeatability of the results across different MRI scanners, the study employed a DTI basic phantom that mimics restricted anisotropic diffusion in the brain, in particular in white matter. The phantom, described in Chapter 3 was scanned with the acquisition protocol described in Section 3.3 on four different scanners, three 3T MRI scanners (GE Premier located at the OCMR, GE Premier located at the Churchill Hospital in Oxford, and Siemens Prisma) and one 1.5T scanner located at the Churchill Hospital in Oxford, the GE Artist, described in Chapter 3. The acquired diffusion data were then fitted with the tensor, Bingham-NODDI and AMICO-NODDI models, and the final results were extracted from ROIs contoured onto the quantitative maps. To assess the consistency of results across different MRI scanners, first intra-site stability was assessed on each scanner computing the coefficient of variation (CV) considering the mean and the standard deviation of each model's metric on each scanner's set of acquisitions. The final results of the inter-site phantom study are shown in Chapter 6. The consistency of results are shown by low CV values for each scanner. Comparisons of results obtained on each model for each scanner show similar results within the margin of error with slight differences. In particular, the analysis performed on the single-shell acquisitions shows that the Fractional Anisotropy values are not consistent with the expected value given by the manufacturer of the phantom whilst results obtained fitting the multi-shell data show acceptable Fractional Anisotropy values and consistency of results across different MRI scanners for the tensor model. Furthermore, the analysis has also shown that the Mean Diffusivity obtained values decrease with increasing echo times, as highlighted by results obtained fitting data acquired on the GE Artist. This is further investigated Chapter 7. The basic phantom was scanned multiple times with different echo times, spanning from an echo time of 56.3 ms to 126 ms. Results show that the Mean Diffusivity values decrease with increasing echo time whilst the Fractional Anisotropy values are still acceptable. To further investigate what might be the cause of this decrease, acquisitions with multiple diffusion weighting b-values was performed, in order to obtain a better fit for the MD values, hopefully stable increasing echo time. However, the results show that despite increasing the number of points (b-values) on which the MD values are being sampled, the results of mean diffusivity are still decreasing. This implies that this study needs further investigation.

Regarding the Bingham-NODDI model, results show consistency within the margin of errors across different MRI scanners, indicating there is no significant variation in the analyzed metrics hence suggesting the reliability of the model.

In addition to the phantom study, two healthy volunteers were scanned on the GE Premier and on the Siemens Prisma. The first volunteer was scanned twice on each scan, to assess intra-site repeatability of results and compare it between the two scanners. The second volunteer was scanned once on each scanner. The consistency of the measures contributes to the evidence of stability of the Bingham-NODDI model, given that slight variations on the values results are still within the margin of error for the main metrics of interest, such as the Orientation Dispersion Index (ODI), the Tissue Volume Fraction and Intra-neurite Volume Fraction. Further investigation analyzing diffusion brain data acquired on both 3T scanners of more healthy volunteers may increase the evidence of the model's applicability in different research and clinical applications thus providing a more robust statistical investigation. The model's reliability serves as a solid foundation for detecting minor changes in the brain microstructure over time, representing an additional tool for clinicians thus representing a powerful tool in both neuroscience and the clinical fields. This study also poses a step forward for multi-center studies as it contributes to transcending the boundaries of individual equipment thus establishing solid ground for collaborative research and clinical applications.

Bibliography

[1] W. D. Foltz and D. A. Jaffray. "Principles of Magnetic Resonance Imaging". In: *Radiation Research* 177.4 (2012), pp. 331–348. DOI: 10.1667/RR2620.1. URL: https://doi.org/10.1667/RR2620.1.

[2] E.M. Haacke et al. *Magnetic Resonance Imaging: Physical Principles and Sequence Design*. Wiley, 1999. ISBN: 9780471351283. URL: https://books.google.it/books?id=BnOvQgAACAAJ.

[3] Andrew L Alexander et al. "Diffusion tensor imaging of the brain". In: *Neurotherapeutics* 4.3 (2007), pp. 316–329.

[4] P.J. Basser, J. Mattiello, and D. Lebihan. "Estimation of the Effective Self-Diffusion Tensor from the NMR Spin Echo". In: *Journal of Magnetic Resonance, Series B* 103.3 (1994), pp. 247–254. ISSN: 1064-1866. DOI: https://doi.org/10.1006/jmrb.1994.1037. URL: https://www.sciencedirect.com/science/article/pii/S1064186684710375.

[5] Xiuwei Fu et al. "Microstructural white matter alterations in mild cognitive impairment and Alzheimer's disease: study based on neurite orientation dispersion and density imaging (NODDI)". In: *Clinical Neuroradiology* 30 (2020), pp. 569–579.

[6] Inge Timmers et al. "Assessing microstructural substrates of white matter abnormalities: a comparative study using DTI and NODDI". In: *PloS one* 11.12 (2016), e0167884.

[7] Chase R Figley et al. "Potential pitfalls of using fractional anisotropy, axial diffusivity, and radial diffusivity as biomarkers of cerebral white matter microstructure". In: *Frontiers in Neuroscience* 15 (2022), p. 799576.

[8] Hui Zhang et al. "NODDI: practical in vivo neurite orientation dispersion and density imaging of the human brain". In: *Neuroimage* 61.4 (2012), pp. 1000–1016.

[9] Zach Eaton-Rosen et al. "Longitudinal measurement of the developing grey matter in preterm subjects using multi-modal MRI". In: *NeuroImage* 111 (2015), pp. 580–589.

[10] Aga Z Burzynska et al. "Age-related differences in white matter microstructure: region-specific patterns of diffusivity". In: *Neuroimage* 49.3 (2010), pp. 2104–2112.

[11] Maira Tariq et al. "Bingham–NODDI: Mapping anisotropic orientation dispersion of neurites using diffusion MRI". In: *Neuroimage* 133 (2016), pp. 207–223.

[12] MA Islam. "Einstein–Smoluchowski diffusion equation: a discussion". In: *Physica Scripta* 70.2-3 (2004), p. 120.

[13] Philippe Douek et al. "MR color mapping of myelin fiber orientation". In: *J Comput Assist Tomogr* 15.6 (1991), pp. 923–929.

[14] Denis Le Bihan and Eric Breton. "Imagerie de diffusion in vivo par résonance magnétique nucléaire". In: *Comptes rendus de l'Académie des sciences. Série 2, Mécanique, Physique, Chimie, Sciences de l'univers, Sciences de la Terre* 301.15 (1985), pp. 1109–1112.

[15] Andrew L Alexander et al. "Diffusion tensor imaging of the brain". In: *Neurotherapeutics* 4.3 (2007), pp. 316–329.

[16] Pp Ni et al. "Technical advancements and protocol optimization of diffusion-weighted imaging (DWI) in liver". In: *Abdominal Radiology* 41 (Jan. 2016). DOI: 10.1007/s00261-015-0602-x.

[17] Chandana Lall et al. "Diffusion-weighted imaging in hemorrhagic abdominal and pelvic lesions: restricted diffusion can mimic malignancy". In: *Abdominal Radiology* 43 (July 2018), pp. 1–13. DOI: 10.1007/s00261-017-1366-2.

[18] E. O. Stejskal and J. E. Tanner. "Spin Diffusion Measurements: Spin Echoes in the Presence of a Time-Dependent Field Gradient". In: *The Journal of Chemical Physics* 42.1 (July 2004), pp. 288–292. ISSN: 0021-9606. DOI: 10.1063/1.1695690. eprint: https://pubs.aip.org/aip/jcp/article-pdf/42/1/288/11154285/288_1_online.pdf. URL: https://doi.org/10.1063/1.1695690.

[19] Peter J Basser, James Mattiello, and Denis LeBihan. "Estimation of the effective self-diffusion tensor from the NMR spin echo". In: *Journal of Magnetic Resonance, Series B* 103.3 (1994), pp. 247–254.

[20] Khader M Hasan, Dennis L Parker, and Andrew L Alexander. "Comparison of gradient encoding schemes for diffusion-tensor MRI". In: *Journal of Magnetic Resonance Imaging: An Official Journal of the International Society for Magnetic Resonance in Medicine* 13.5 (2001), pp. 769–780.

[21] Cheng Guan Koay et al. "A unifying theoretical and algorithmic framework for least squares methods of estimation in diffusion tensor imaging". In: *Journal of magnetic resonance* 182.1 (2006), pp. 115–125.

[22] Derek K Jones, Mark A Horsfield, and Andrew Simmons. "Optimal strategies for measuring diffusion in anisotropic systems by magnetic resonance imaging". In: *Magnetic Resonance in Medicine: An Official Journal of the International Society for Magnetic Resonance in Medicine* 42.3 (1999), pp. 515–525.

[23] John A Nelder. "Downhill simplex method". In: *Computer journal* 7 (1965), pp. 308–313.

[24] Carlo Pierpaoli and Peter J Basser. "Toward a quantitative assessment of diffusion anisotropy". In: *Magnetic resonance in Medicine* 36.6 (1996), pp. 893–906.

[25] Carlo Pierpaoli and Peter J Basser. "Toward a quantitative assessment of diffusion anisotropy". In: *Magnetic resonance in Medicine* 36.6 (1996), pp. 893–906.

[26] Peter J Basser and Sinisa Pajevic. "Statistical artifacts in diffusion tensor MRI (DT-MRI) caused by background noise". In: *Magnetic Resonance in Medicine: An Official Journal of the International Society for Magnetic Resonance in Medicine* 44.1 (2000), pp. 41–50.

[27] Andrew L Alexander et al. "Analysis of partial volume effects in diffusion-tensor MRI". In: *Magnetic Resonance in Medicine: An Official Journal of the International Society for Magnetic Resonance in Medicine* 45.5 (2001), pp. 770–780.

[28] Andrew L Alexander et al. “A geometric analysis of diffusion tensor measurements of the human brain”. In: *Magnetic Resonance in Medicine: An Official Journal of the International Society for Magnetic Resonance in Medicine* 44.2 (2000), pp. 283–291.

[29] C-F Westin et al. “Processing and visualization for diffusion tensor MRI”. In: *Medical image analysis* 6.2 (2002), pp. 93–108.

[30] P Mansfield. “Real-time echo-planar imaging by NMR”. In: *British medical bulletin* 40.2 (1984), pp. 187–190.

[31] Robert Turner et al. “Echo-planar imaging of intravoxel incoherent motion.” In: *Radiology* 177.2 (1990), pp. 407–414.

[32] José M Soares et al. “A hitchhiker’s guide to diffusion tensor imaging”. In: *Frontiers in neuroscience* 7 (2013), p. 31.

[33] Jesper LR Andersson and Stefan Skare. “A model-based method for retrospective correction of geometric distortions in diffusion-weighted EPI”. In: *Neuroimage* 16.1 (2002), pp. 177–199.

[34] Gustavo Kunde Rohde et al. “Comprehensive approach for correction of motion and distortion in diffusion-weighted MRI”. In: *Magnetic Resonance in Medicine: An Official Journal of the International Society for Magnetic Resonance in Medicine* 51.1 (2004), pp. 103–114.

[35] Partha Mukherjee et al. “Diffusion tensor MR imaging and fiber tractography: technical considerations”. In: *American Journal of Neuroradiology* 29.5 (2008), pp. 843–852.

[36] Derek Kenton Jones et al. “Isotropic resolution diffusion tensor imaging with whole brain acquisition in a clinically acceptable time”. In: *Human brain mapping* 15.4 (2002), pp. 216–230.

[37] Andrew L Alexander et al. “Comparison of diffusion tensor imaging measurements at 3.0 T versus 1.5 T with and without parallel imaging”. In: *Neuroimaging Clinics* 16.2 (2006), pp. 299–309.

[38] J Le R Conel. “The postnatal development of the human cerebral cortex. Vol. 1. The cortex of the newborn.” In: (1939).

[39] Bob Jacobs, Lori Driscoll, and Matthew Schall. “Life-span dendritic and spine changes in areas 10 and 18 of human cortex: a quantitative Golgi study”. In: *Journal of comparative neurology* 386.4 (1997), pp. 661–680.

[40] Suma Jacob et al. “Sustained human chemosignal unconsciously alters brain function”. In: *Neuroreport* 12.11 (2001), pp. 2391–2394.

[41] John C Fiala, Josef Spacek, and Kristen M Harris. “Dendritic spine pathology: cause or consequence of neurological disorders?” In: *Brain research reviews* 39.1 (2002), pp. 29–54.

[42] Denis Le Bihan et al. “Diffusion tensor imaging: concepts and applications”. In: *Journal of Magnetic Resonance Imaging: An Official Journal of the International Society for Magnetic Resonance in Medicine* 13.4 (2001), pp. 534–546.

[43] Aaron Szafer, Jianhui Zhong, and John C Gore. “Theoretical model for water diffusion in tissues”. In: *Magnetic resonance in medicine* 33.5 (1995), pp. 697–712.

[44] Kanti V. Mardia and Peter E. Jupp. *Directional Statistics*. Wiley series in probability and statistics., 1999. DOI: 10.1002/9780470316979.

[45] Alessandro Daducci et al. "Accelerated microstructure imaging via convex optimization (AMICO) from diffusion MRI data". In: *Neuroimage* 105 (2015), pp. 32–44.

[46] Frederik Bernd Laun, Sandra Huff, and Bram Stieltjes. "On the effects of dephasing due to local gradients in diffusion tensor imaging experiments: relevance for diffusion tensor imaging fiber phantoms". In: *Magnetic resonance imaging* 27.4 (2009), pp. 541–548.

[47] Stavroula Kyriazi et al. "Optimising diffusion-weighted imaging in the abdomen and pelvis: comparison of image quality between monopolar and bipolar single-shot spin-echo echo-planar sequences". In: *European radiology* 20 (2010), pp. 2422–2431.

[48] Mark W Woolrich et al. "Bayesian analysis of neuroimaging data in FSL". In: *Neuroimage* 45.1 (2009), S173–S186.

[49] Jesper LR Andersson, Stefan Skare, and John Ashburner. "How to correct susceptibility distortions in spin-echo echo-planar images: application to diffusion tensor imaging". In: *Neuroimage* 20.2 (2003), pp. 870–888.

[50] Jesper LR Andersson and Stamatios N Sotiropoulos. "An integrated approach to correction for off-resonance effects and subject movement in diffusion MR imaging". In: *Neuroimage* 125 (2016), pp. 1063–1078.

[51] Matteo Bastiani et al. "Automated quality control for within and between studies diffusion MRI data using a non-parametric framework for movement and distortion correction". In: *Neuroimage* 184 (2019), pp. 801–812.

[52] Mark Jenkinson et al. "FSL". In: *NeuroImage* 62.2 (2012). 20 YEARS OF fMRI, pp. 782–790. ISSN: 1053-8119. DOI: https://doi.org/10.1016/j.neuroimage.2011.09.015. URL: https://www.sciencedirect.com/science/article/pii/S1053811911010603.

[53] Stephen M. Smith et al. "Advances in functional and structural MR image analysis and implementation as FSL". In: *NeuroImage* 23 (2004). Mathematics in Brain Imaging, S208–S219. ISSN: 1053-8119. DOI: https://doi.org/10.1016/j.neuroimage.2004.07.051. URL: https://www.sciencedirect.com/science/article/pii/S1053811904003933.

[54] Rutger HJ Fick, Demian Wassermann, and Rachid Deriche. "The dmipy toolbox: Diffusion mri multi-compartment modeling and microstructure recovery made easy". In: *Frontiers in neuroinformatics* 13 (2019), p. 64.

[55] Mark Jenkinson et al. "Improved optimization for the robust and accurate linear registration and motion correction of brain images". In: *Neuroimage* 17.2 (2002), pp. 825–841.

[56] Kurt G Schilling et al. "Distortion correction of diffusion weighted MRI without reverse phase-encoding scans or field-maps". In: *PLoS One* 15.7 (2020), e0236418.

Acknowledgements

I would like to thank with all my heart Professor Claudia Testa for giving me this amazing opportunity at Oxford. Professor Testa has shown constant support and has always believed in me, proving to be extremely helpful, a safe haven for a student at the mercy of the uncertainties that research and academic life can sometimes represent. Her mentor figure as a scientist has been and will always remain a source of great inspiration for me and I will not be able to express in the right words how grateful I am for her availability, kindness and professionalism and for this huge opportunity.

I would like to express my heartfelt gratitude to Doctor James Grist, my mentor and supervisor at OCMR, University of Oxford. James, your valuable advices and constant faith in me as well as your constant presence and encouragement to constantly improve have had a significant impact on my professional growth. Your support during my time at Oxford was crucial to regaining my confidence in my future as a scientist. Your passion and joy manifested in your work were a source of inspiration and admiration. Working with you and your team has left an indelible mark on my academic journey. It was an honor to be able to observe you at work and be considered an integral part of your team. Even just through observing you all working, I have learned significantly. I look forward to future collaborations and am grateful to have had the opportunity to work with such an exceptional person like you.

I would also like to express my sincere gratitude to my colleagues at OCMR. Aaron, Jordan, Kylie, Damian, Sarah, Dan, Ayaka, Ferenc, Laci, Thierry working and learning alongside such a talented and diverse group has been an incredible privilege. It was extremely instructive to be part of such a stimulating collaborative environment, always ready to engage in interesting discussions and help each other, demonstrating to me that the strength and beauty of academic research lie in being a team-player whose ultimate aim is to work towards a common goal by supporting the successes of others besides your own, because, after all, the one who really has to win is always science. The friendships I have formed within this vibrant academic community have made my time in Oxford extremely fulfilling and unforgettable, making me feel at home even when my home was thousands of miles away. Sharing papers, cakes, smiles, coffee and multicultural facts has been a pleasure, thank you all.

I am beyond grateful to my parents for their unwavering support, my accomplishments were non-existent if it was not for you. Thanks to my sister, who held me while I was crying stressed out and scared infinite times and thanks to my brother who has made me laugh and kept me sane in a wiser way than I could ever imagine he would be able to to do for his young age.
Ottavio, you know I am here writing a thesis mainly because of you. You saw the good in me, you stood by me faithfully in scary times, comforted me and remembered to me how capable I was when I could only think to give up, you have been my constant, my

shelter, the basecamp to help me restore in dark periods of my life, I love you dearly.
Thanks to my friends, Giulia, Alessia, Marta, Leda for being with me all the time, you have been the foundation of my success, wheter it was offering emotional assistance, memes or hugs. I am grateful for each one of you to be part of my life, you are all wonderful and I cannot imagine a future without you in it.

Thanks to Mattia for always being there for me when I needed help, you've been an amazing friend and colleague.

This thesis wouldn't have been possible without the collective support, guidance, love and encouragement of all these individuals.

Thank you all for being a vital part of my journey.